Doctoral theses at NTNU, 2024:301

Farid Aligolzadeh

Studies of Turbulence in a von Kármán Swirling Flow

Doctoral thesis

NTNU
Norwegian University of Science and Technology
Thesis for the Degree of
Philosophiae Doctor
Faculty of Engineering
Department of Energy and Process Engineering

NTNU
Norwegian University of
Science and Technology

Farid Aligolzadeh

Studies of Turbulence in a von Kármán Swirling Flow

Thesis for the Degree of Philosophiae Doctor

Trondheim, August 2024

Norwegian University of Science and Technology
Faculty of Engineering
Department of Energy and Process Engineering

NTNU
Norwegian University of
Science and Technology

NTNU
Norwegian University of Science and Technology

Thesis for the Degree of Philosophiae Doctor

Faculty of Engineering
Department of Energy and Process Engineering

ISBN 978-82-326-8194-5 (printed ver.)
ISBN 978-82-326-8193-8 (electronic ver.)
ISSN 1503-8181 (printed ver.)
ISSN 2703-8084 (online ver.)

Doctoral theses at NTNU, 2024:301

Printed by NTNU Grafisk senter

Abstract

The aim of the present thesis was to improve our fundamental understanding of the dynamics of turbulence at the small and large-scales produced in a von Kármán swirling flow. The body of the work was based on the particle image velocimetry (PIV) measurements performed within a large-size facility which enabled large Reynolds numbers but with large length-scales accessible to PIV. This thesis has focused primarily on three topics that are connected to each other through a well-known concept in turbulence theory, the energy cascade. The first study investigated the small-scale dynamics and kinematics of turbulence. The second study investigated the free decay of turbulence, a phenomenon that facilitates evaluating the large-scales to the small-scales energy transfer through the cascade process. Finally, the third study investigated the large-scale, energetic harmonic motions in the flow with and without modulations in the turbulent forcing.

In the small-scale study, the interactions between the vortices at the dissipation scale with the surrounding fluid were investigated. An experimental data set of homogenous turbulence from scanning PIV [Lawson and Dawson, 2014, 2015] at the center of the von Kármán swirling flow along with a direct numerical simulation (DNS) data set of homogeneous isotropic turbulence were studied. A recent definition of objective vortex structure [Haller et al., 2016] was implemented for the first time on a fully resolved 3D experimental dataset of small-scale turbulence to detect the vortex structures in the flow fields. Various statistics conditioned on the structures and volume of the flow were presented and compared. To investigate the interaction of the vortices with the background fluid, enstrophy transport equation was evaluated in the radial and axial direction of the vortices. In addition, the entrainment velocity was calculated on the boundary of the vortices. Overall, it was shown that the vortices interacted with the surrounding fluid by exchanging mass, enstrophy, and momentum in a manner that is very similar to turbulent entrainment

in free shear flows.

In the decay study, the stationary homogeneous turbulence generated by the counter-rotating impellers went though a free decay process by stopping the impellers. This decay process was characterized by measuring the flow field using stereoscopic PIV. This procedure was repeated many times to ensure a reasonable convergence of turbulence statistics. It was shown that when considering the velocity magnitude from all three velocity components to monitor the decay of the turbulent kinetic energy, an exponential decay in time was obtained with an exponent of $n = -1.62$, $k(t) \sim t^n$, steeper than the theoretical predictions of Saffman ($n = -1.2$) and Loitsiansky ($n = -1.43$). However, analyzing the individual velocity components, revealed that the decay in the axial direction closely followed Loitsiansky prediction with an exponent of $n = -1.38$ whereas, the radial and circumferential velocity components were in the saturation/confinement regime with an exponent of $n = -1.99$. The growth rates of the integral length-scales in time also confirmed the Loitsiansky prediction in the axial direction, and the saturation/confinement regime in the other directions.

The third study was motivated by the findings of Baj et al. [2019] who identified the presence of an energetic slowly rotating structure in a von Kármán swirling flow. To investigate this, various cases were designed and measured using stereoscopic PIV. It was shown that when the Reynolds number was lower than a critical value as hypothesized by Cortet et al. [2010], an energetic large-scale structure emerged in the stationary flow oscillating in all directions at approximately twice the frequency of the impellers. However, at a Reynolds number beyond the critical range, the structure was not observed. Various scenarios of harmonic and random modulations were imposed on the impellers to investigate the dependence on turbulent boundary conditions on the appearance or suppression of the instability. The structure clearly emerges when a harmonic phase shift is imposed in between the impellers during the modulation. The structure accounted for approximately 40% of the kinetic energy of the flow and oscillated in the axial and circumferential directions. The oscillation in the axial direction was more pronounced. Moreover, the structure had an oval shape and the frequency of its oscillation was locked to the modulation frequency. The cross-correlation between the velocity field and forcing revealed that the axial oscillation phase was approximately 0.2π ahead of the oscillation phase in the circumferential direction.

Preface

This thesis was submitted to the Norwegian University of Science and Technology (NTNU) for partial fulfillment of the requirements for the degree of philosophiae doctor. The doctoral work was carried out in the Thermo Fluids group at the Department of Energy and Process Engineering (EPT), from September 2020 to September 2024. The work has been supervised by Professor James R. Dawson and co-supervised by Professor Markus Holzner.

The research was funded internally by the Faculty of Engineering (IV), Norwegian University of Science and Technology (NTNU).

The thesis is made up of four chapters and three scientific articles. Chapter 1 presents an introduction to the topic, a brief literature review on von Kármán swirling flows, along with the objectives and outline. Chapter 2 provides the turbulence theory and the related concepts along with the mathematical analysis techniques used in this thesis. This chapter helps the reader to understand and interpret the motivations and findings of the present work. Chapter 3 provides an overview of the apparatus, the measurement diagnostics (PIV), along with the conducted experiments. A brief conclusion of the work and summary of the scientific articles are given in chapter 4. The articles are attached in full text at the end of the thesis and cover three main topics. Article 1 investigates the interaction between small-scale vortex structures and the surrounding fluid. Article 2 investigates the free decay of turbulence in a von Kármán swirling flow. Article 3 investigates harmonic large-scale motions in a von Kármán swirling flow with and without forcing modulations.

A list of the articles with a summary of the authors contribution is provided:

Article 1:

Entrainment, detrainment and enstrophy transport by small-scale vortex structures
Farid Aligolzadeh, Markus Holzner, and James R. Dawson
Published in Journal of Fluid Mechanics

Authors' contributions: **Farid Aligolzadeh**: Conceptualization, Methodology, Software, Formal analysis, Writing - Original Draft. **Markus Holzner**: Conceptualization, Writing - Review & Editing, Supervision. **James R. Dawson**: Conceptualization, Writing - Review & Editing, Supervision, Funding acquisition.

Article 2:

Experiments of turbulent decay in a von Kármán swirling flow at high Reynolds number
Farid Aligolzadeh, Pawel Baj, and James R. Dawson
Under consideration for publication in Journal of Fluid Mechanics

Authors' contributions: **Farid Aligolzadeh**: Conceptualization, Methodology, Investigation, Formal analysis, Writing - Original Draft. **Pawel Baj**: Formal analysis, Writing - Review & Editing. **James R. Dawson**: Conceptualization, Writing - Review & Editing, Supervision, Funding acquisition.

Article 3:

Experimental investigation of large-scale harmonic motions in a von Kármán swirling flow
Farid Aligolzadeh, Pawel Baj, and James R. Dawson
Under consideration for publication in Journal of Fluid Mechanics

Authors' contributions: **Farid Aligolzadeh**: Conceptualization, Methodology, Investigation, Formal analysis, Writing - Original Draft. **Pawel Baj**: Conceptualization, Methodology, Investigation, Writing - Review & Editing. **James R. Dawson**: Conceptualization, Writing - Review & Editing, Supervision, Funding acquisition.

Additional articles that are not officially in the thesis:

Appendix A:

Study of fine-scale vortical structures in a von Kármán mixing flow
Farid Aligolzadeh, Markus Holzner, and James R. Dawson
Proceeding of the 12^{th} *International Symposium on Turbulence and Shear Flow Phenomena (TSFP12), July 19-22, 2022, Osaka, Japan (Online)*

Authors' contributions: **Farid Aligolzadeh**: Conceptualization, Methodology, Software, Formal analysis, Writing - Original Draft. **Markus Holzner**: Conceptualization, Writing - Review & Editing, Supervision. **James R. Dawson**: Conceptualization, Writing - Review & Editing, Supervision, Funding acquisition.

Appendix B:

Large-scale forcing modulation of high Reynolds number turbulence in a von Kármán swirling flow

Farid Aligolzadeh, Pawel Baj, and James R. Dawson
Proceeding of the 13^{th} *International Symposium on Turbulence and Shear Flow Phenomena (TSFP13), June 25-28, 2024, Montréal, Canada*

Authors' contributions: **Farid Aligolzadeh**: Conceptualization, Methodology, Investigation, Formal analysis, Writing - Original Draft. **Pawel Baj**: Conceptualization, Methodology, Investigation, Writing - Review & Editing. **James R. Dawson**: Conceptualization, Writing - Review & Editing, Supervision, Funding acquisition.

Acknowledgements

Now that I am approaching the end of my PhD, I would like to express my gratitude to everyone who has supported me over the past four years.

First and foremost, I want to acknowledge and thank my supervisor Professor James R. Dawson for choosing and trusting me to pursue this PhD in the first place. James' openness to new ideas, his outside-the-box thinking, and his capability to see the big picture have been quite helpful. I am deeply grateful for the freedom he gave me to explore topics that interested me during my PhD.

Additionally, I extend my thanks to Professor Markus Holzner and Professor Pawel Baj. Their assistance in the papers we worked on together and the insightful discussions we had enriched my research experience.

Professors Philippe Lavoie, Ramis Örlü, and R. Jason Hearst served as committee members to assess this thesis. I appreciate the time and effort they invested and their valuable comments.

Lastly, my heartfelt appreciation goes out to my family, friends, and colleagues whose kindness has warmed my heart.

Contents

Chapter 1

Introduction

1.1 What is turbulence?

'Turbulence is the most important unsolved problem of classical physics.'
Richard Feynman (1970) [Feynman et al., 2011]

Turbulence does not have a precise definition but its features are recognizable and can be described. Turbulence is the random and chaotic motion of fluid elements that rapidly transfers momentum, compared to the slow transfer of momentum in laminar flow where fluid elements move in parallel layers. At low flow velocities, viscosity is able to damp instabilities in the system keeping the fluid elements in an ordered structure. However, at sufficiently high velocities the inertia of the fluid element exceeds viscous effects which paves the way for various instabilities to grow and drive the system to turbulence.

Turbulence is ubiquitous in nature and engineering applications, because it transfers heat, mass, momentum, and species. Thus, understanding turbulence is essential. We see fluid motion everywhere in our world and in most cases, this motion belongs to a category of turbulent flows. In contrast with other complex phenomena in physics, we can often easily see turbulence with the naked eye, for example, fast flowing rivers, smoke from a chimney, and atmosphere and ocean currents. However, it remains extremely challenging to comprehend, interpret, and describe [Tsinober, 2009].

The motion of a fluid element in an incompressible turbulent flow far from any boundaries is determined by a competition between inertia, viscous, and pressure forces and described by the Navier-Stokes equation. The Navier-Stokes equation is a second order nonlinear partial differential equation (PDE) for the momentum field derived from Newton's second law of motion. The reason behind the complexity of turbulence can be summarized briefly with 3N's that are intrinsic features of the Navier-Stokes equation, i.e. nonlinearity, nonlocality, and non-integrability. Nonlinearity, which is expressed through the inertia term, causes self-interactions between different structures of turbulence inside the flow field. Nonlocality, which is due to the pressure gradient term, passes the information between distinct regions of the flow field via pressure waves so that the motion of a fluid element can be affected by the motion of far away fluid elements. Finally, if it was possible to integrate the Navier-Stokes equations analytically over a volume, one could determine all fluid motions subjected to any forcing. However, Navier-Stokes at large velocities possess mechanisms of self-randomization which makes the dynamical system non-integrable [Tsinober, 2009].

Depending on the distance of the flow from a wall (boundary), incompressible turbulent flows can be divided into two general groups of (i) free shear and (ii) wall bounded flows. In free shear flows, turbulence is caused by mean velocity differences, remote from walls. Jets, wakes, and mixing layers are well-known examples of free shear flows and are shown in figure 1.1. On the other hand, most turbulent flows in nature and engineering applications are bounded by at least one solid surface (wall). Wall bounded flows include internal flows, such as flows in pipes and ducts, and external flows, such as atmospheric boundary layer and the flow of rivers [Pope, 2000].

Due to its great significance in natural phenomena and technological applications, turbulence has been studied for over a century. There have been groundbreaking findings along the way that altered our understanding of turbulence yet we still lack a complete theory. Most of these findings have been possible thanks to the rapid advancements in computers and experimental measurement techniques in the recent decades. However, our understanding of turbulence is still limited and it seems we still have a long and challenging path ahead of us.

1.2 Von Kármán swirling flow

This thesis focuses on stationary turbulence generated in a closed cylindrical container in between two counter-rotating impellers, known as von Kármán swirling flow which is essentially a stirred vessel. This type of flow has gained considerable attention in turbulence research since the original work of von Kármán [1921] where the flow induced by an infinitely large rotating disk was analytically investigated. Later on, Batchelor [1951] introduced a second counter-rotating disk. Batchelor [1951] and Stuart [1954] performed analytical investigations on the flow generated between the two infinite coaxial disks. Stewartson [1953] and Picha and Eckert [1958] considered finite counter-rotating disks which became a

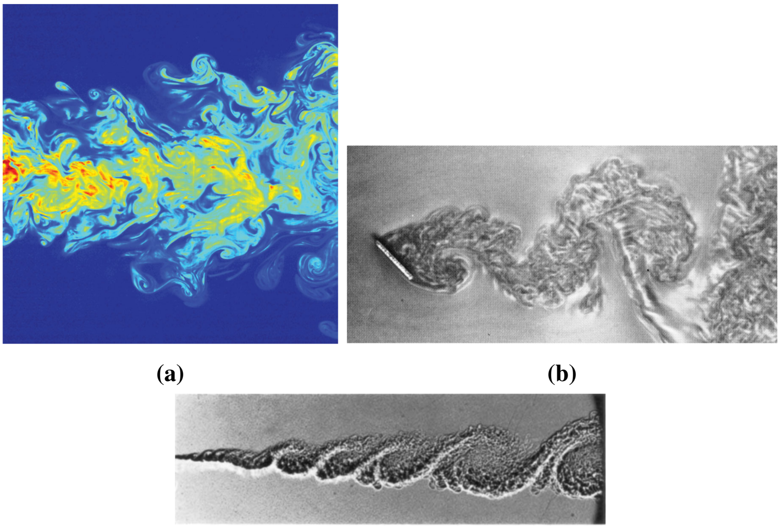

(c)

Figure 1.1: Examples of free shear flows; (a) far field of a turbulent jet, source: Westerweel et al. [2009], (b) turbulent wake behind an inclined flat plate, source: Cantwell [1981], and (c) turbulent mixing layer, source: Brown and Roshko [1974].

standard configuration in numerous experimental studies afterwards. A review of the analytical solutions available for infinite disks is presented in Zandbergen and Dijkstra [1987]. It is worth noting that the name 'von Kármán swirling flow' became common after being used in the above mentioned review paper. Overall, the attempts to find an analytical solution for von Kármán swirling flows with finite disks at high Reynolds numbers have not been successful.

Figure 1.2 shows the mean flow pattern of a von Kármán swirling flow consists of a primary rotationally shearing flow, horizontal shear layers, generated due to the counter-rotation of impellers. A secondary flow is induced by the pressure gradients in form of pumping circulations in the vertical planes around the flow axis. This stationary shear flow has been of interest in experimental studies of turbulence, as it can generate high Reynolds numbers in a relatively small-size facility where the region close to the geometrical center of the flow provides homogeneous turbulence with near zero mean flow and high velocity fluctuations [Lawson and Dawson, 2014, 2015]. Reynolds number for this flow is defined as $Re = \Omega R^2/\nu$ where Ω is impeller rotational speed, R is impeller radius, and ν is the kinematic viscosity of the flow. This definition indicates that for a constant kinematic viscosity, high Reynolds numbers are achieved in a von Kármán swirling flow either by increasing the rotational speed or radius of the impeller.

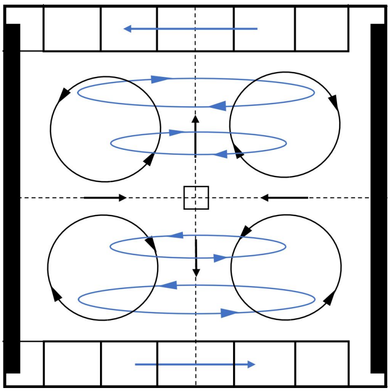

Figure 1.2: Schematic of the mean flow pattern in a von Kármán swirling flow. The horizontal shear layers are depicted in blue and the vertical circulation patterns are in black. The square at the center illustrates the region with high fluctuations and near zero mean flow. Source: Aligolzadeh et al. [2023].

Experimental studies can be generally categorized into two groups; i) studies of small-scale measurements where the focus is on the structures and statistics at the dissipation scale and ii) studies of large-scale measurements where the focus is on the dynamics and global instabilities of the flow motion in the inertial and energy injection scales.

Many studies have been devoted to the investigation of small-scale structures and intermittency [Belin et al., 1996; Bonn et al., 1993; Cadot et al., 1995; Chainais et al., 1999; Douady et al., 1991; Faller et al., 2021; Fauve et al., 1993; La Porta et al., 2000; Worth, 2010; Worth and Nickels, 2011], as well as Lagrangian tracking and dynamics of accelerating particles in turbulence [Angriman et al., 2020; Brown et al., 2009; Cheminet et al., 2022; Huck et al., 2017; La Porta et al., 2001; Ouellette et al., 2006a,b; Volk et al., 2011; Voth et al., 1998, 2002]. Moreover, dissipation scaling [Zocchi et al., 1994], velocity gradients dynamics [Lawson and Dawson, 2015], assessment of Kolmogorov's refined hypothesis [Lawson et al., 2019], the inter-scale energy transfer [Knutsen et al., 2020], and non-viscous dissipation [Debue et al., 2021] are examples of other small-scale related topics investigated using a von Kármán swirling flow.

On the other hand, experimental studies of the large-scale flow motions are not as well reported as the small-scales, but have shown interesting phenomena, in particular global instabilities and symmetry breaking. Ravelet et al. [2008] investigated the transition from laminar regime to fully developed turbulence over a wide range of Reynolds numbers. They found that the transition started at $Re \approx 1000$ reaching a fully turbulent state at $Re \approx 3300$. Furthermore, they suggested that the transition in a von Kármán swirling flow is globally supercritical, i.e. the dynamics of transition can be characterized by the velocity fluctuations in the flow.

The majority of these large-scale studies are focused on the symmetry breaking behaviors in the flow in the form of instabilities. The mean velocity field of a von Kármán swirling flow with counter-rotating impellers is geometrically symmetric with respect to any π radian rotation around any line on the equatorial plane passing the axis of rotation, i.e. R_π symmetry in figure 1.3(a). The deviation from R_π symmetry (symmetry breaking) can be measured in time by space-averaged angular momentum. When this parameter is not equal to zero, the symmetry is broken. An example of such a symmetry breaking behavior is shown in figure 1.3(b) which shows how the time-series of angular momentum is not instantaneously zero but fluctuates. The features and dynamics of the symmetry breaking have been investigated by Cadot et al. [2003]; Cortet et al. [2010]; de la Torre and Burguete [2007]; Ravelet et al. [2004]. Cortet et al. [2010] showed experimental evidence that the symmetry breaking behavior goes through a critical phase transition within the range $5 \times 10^4 < Re < 10^5$.

In a recent series of studies, Baj et al. [2019]; Berning and Rösgen [2023]; Berning et al. [2017] observed energetic large-scale flow structures slowly rotating around the axis of rotation as illustrated in figure 1.4. Baj et al. [2019] reported that the identified structure resembled macro-instabilities in stirred vessels [Doulgerakis et al., 2011]. Aside from the effects that the symmetry breaking and instability structures can have on the overall dynamics of turbulence, they can be of interest from a practical point of view, e.g. manipulation of the mixing features within the system.

Due to the size and complexity of von Kármán swirling flows, performing direct numerical simulations (DNS) to study the turbulence, even for low Reynolds numbers, still remains very challenging. To avoid this complexity at high Reynolds numbers, some simplifications are necessary. For example, turbulence models and large eddy simulations (LES) can be employed to obtain limited information about the flow. Nore et al. [2003] studied symmetry breaking and bifurcation in a von Kármán swirling flow at low Reynolds numbers using the assumptions of axisymmetry and R_π symmetry to simplify the computations. Kreuzahler et al. [2014] performed a DNS study of the flow at $Re \approx 3000$ using a volume penalization method, i.e. activating source terms in equations to ensure the required boundary condition, which showed good agreement with previous experimental observations about the global flow profiles and the poloidal and toroidal mean velocities. Poncet et al. [2008] compared the results of a numerical simulation using a Reynolds stress model (RSM) with the available data from the experiments. They showed that the numerical predictions of the mean circumferential velocity profile were

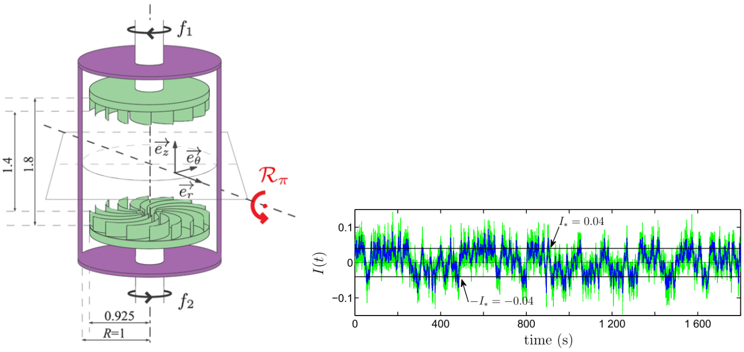

(a) **(b)**

Figure 1.3: Symmetry breaking behavior; (a) the mean velocity field of a von Kármán swirling flow with counter-rotating impellers is symmetric with respect to any π radian rotation around any line on the equatorial plane passing the axis of rotation, i.e. R_π symmetry and (b) when space-averaged angular momentum $I(t)$ is not zero, R_π symmetry is temporally broken. Source: Cortet et al. [2010].

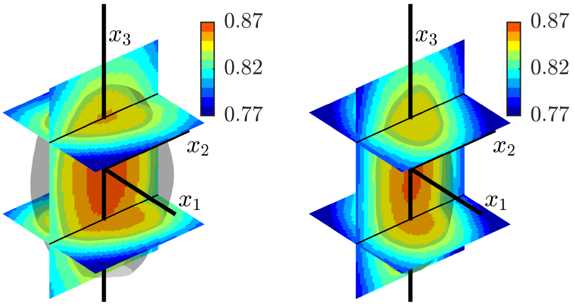

Figure 1.4: Topology of the first two POD modes at the center of a von Kármán swirling flow in Baj et al. [2019]. The iso-surfaces illustrate the magnitude of the contribution to the total velocity field normalized by the velocity fluctuations r.m.s. in mode 1 (on the left) and mode 2 (on the right). Mode 2 is a rotation of mode 1 around the vertical axis and together they form a structure. The structure slowly rotates around the axis at approximately 0.1 of the impeller frequency. Source: Baj et al. [2019].

in good agreement with point velocity measurements using laser Doppler velocimetry (LDV). In a more recent study, Nore et al. [2018] used LES to study the hydrodynamics and magneto-hydrodynamics in a von Kármán swirling flow for Reynolds numbers up to $Re = 10^5$. Their results supported the conjecture that by increasing the kinetic Reynolds number toward infinity, the critical magnetic Reynolds number approaches a constant.

1.3 Objectives

The objective of the thesis is to fill gaps regarding some fundamental features of turbulence and its dynamics in a von Kármán swirling flow at both the small and large-scales. The main objectives are:

i) to investigate the kinematics and dynamics of vortex structures at the dissipation scale and their interaction with the surrounding background fluid using an objective definition of vortices.

ii) to characterize the free decay of turbulence and its behavior in different directions of the flow, along with the comparison with the well-known analytical predictions in the turbulence theory.

iii) to understand the dynamics of the large-scale harmonic motions in the flow and their dependence on the Reynolds number and forcing modulations.

1.4 Outline

The thesis is organized as follows. In Chapter 2 the theoretical framework of turbulence is provided in some detail including the equations and key concepts, which is necessary to understand the motivations, analyses and results presented in this thesis. Chapter 3 first provides some details of the large-size von Kármán swirling flow facility in which the measurements were conducted. Next, principles of particle image velocimetry (PIV) and more specifically, stereoscopic PIV, that was used as the main experimental measurement technique, are described. The last section of this chapter explains the experiments performed in the facility. Chapter 4 provides a brief conclusion of the turbulence features investigated and summarizes the research articles that report the novel findings of this thesis. The research articles are attached to the end of the thesis.

Chapter 2

Turbulence theory

This chapter provides a brief theoretical background as a framework for understanding the motivations behind this research, the methods used, and the fundamental physics necessary to interpret the results. We refer the interested reader to well-known books on turbulent flows, such as Davidson [2015], Pope [2000], and Tsinober [2009], for more details and deeper discussions.

2.1 Governing equations

For an incompressible three dimensional flow ($x_{i=1,2,3}$), the continuity (mass conservation) and momentum (Navier-Stokes) equations are presented in equations 2.1 and 2.2, respectively:

$$\frac{\partial U_i}{\partial x_i} = 0 \tag{2.1}$$

$$\frac{DU_i}{Dt} = \frac{\partial U_i}{\partial t} + U_j \frac{\partial U_i}{\partial x_j} = -\frac{1}{\rho}\frac{\partial P}{\partial x_i} + \nu \frac{\partial^2 U_i}{\partial x_j^2} \tag{2.2}$$

$$\nabla^2 P = -\rho \frac{\partial U_i}{\partial x_j}\frac{\partial U_j}{\partial x_i} \tag{2.3}$$

$$P(x) = \frac{\rho}{4\pi} \int \left[\frac{\partial U_i}{\partial x_j}\frac{\partial U_j}{\partial x_i} \right]_{x=x^*} \frac{dx^*}{|x-x^*|} \tag{2.4}$$

where U_i is the velocity in the i^{th} direction, ρ is density, P is pressure, and ν is the kinematic viscosity of the flow. Equation 2.2 shows a balance between the inertia of the fluid element (left hand side of the equation, i.e. DU/Dt) and the forces imposed on it (right hand side of the equation, i.e. the pressure force: $-1/\rho\nabla P$ and the viscous force: $\nu\nabla^2 U$). By taking the divergence of the Navier-Stokes equation and using the continuity equation, a direct relation between the pressure field and the velocity field is derived in equation 2.3 for an incompressible flow known as the Poisson equation. The Poisson equation can be written in an integral form in equation 2.4 for a finite domain. These equations show an important feature in fluid dynamics, nonlocality, which is of special importance in turbulence. It means that the activities of the velocity field at any local region in the flow field is felt by the remote regions of the flow through the pressure field, P, and the force that it applies on the fluid elements, $-\nabla P$. The pressure field passes the information between different regions of the flow field via pressure waves that are infinitely fast, relative to speed of sound, in incompressible flows. For the case of turbulence this implies that at any time instant, eddies interact with each other no matter how far away they are located in the flow field. However, this interaction is a function of distance and activities within the closer regions in space are of more significance according to equation 2.4.

The vorticity vector describes the rotation of fluid elements and is defined in equation 2.5 as the curl of the velocity vector ($\omega = \nabla \times U$), where ξ_{ijk} is Levi-Civita (alternating) symbol. The vorticity evolution equation can be derived in equation 2.6 by taking the curl of the Navier-Stokes equation (equation 2.2).

$$\omega_i = \xi_{ijk}\frac{\partial U_k}{\partial x_j} \tag{2.5}$$

$$\frac{D\omega_i}{Dt} = \frac{\partial \omega_i}{\partial t} + U_j\frac{\partial \omega_i}{\partial x_j} = \omega_j S_{ij} + \nu\frac{\partial^2 \omega_i}{\partial x_j^2} \tag{2.6}$$

where $S_{ij} = (\partial U_i/\partial x_j + \partial U_j/\partial x_i)/2$ is the rate of strain tensor. This equation indicates that the material derivative of vorticity ($D\omega_i/Dt$) is balanced by the inviscid phenomenon of vortex stretching ($\omega_j S_{ij}$) and the viscous phenomenon of vorticity diffusion ($\nu\partial^2\omega_i/\partial x_j^2$). It is worth mentioning that the pressure term in the Navier-Stokes equation (2.2) vanishes in the vorticity evolution equation of an incompressible flow (2.6) ($-\nabla \times \nabla p/\rho = 0$). In most cases, we are more interested in the magnitude of vorticity rather than its direction. The square of the magnitude represents the local rotational energy that helps us identify turbulent structures within the flow. The rotational energy of the fluid element can be represented by enstrophy where $\omega^2 = \omega_i\omega_i$. Using equation 2.6, an evolution equation can be derived for enstrophy, i.e. enstrophy transport equation and is shown in equation

2.7:

$$\frac{D\omega^2}{Dt} = \frac{\partial \omega^2}{\partial t} + U_j \frac{\partial \omega^2}{\partial x_j} = 2\omega_i \omega_j S_{ij} + \nu \frac{\partial^2 \omega^2}{\partial x_j \partial x_j} - 2\nu \frac{\partial \omega_i}{\partial x_j} \frac{\partial \omega_i}{\partial x_j} \tag{2.7}$$

Similar to equation 2.6, equation 2.7 shows that the evolution of enstrophy ($D\omega^2/Dt$) is governed by a competition between the inviscid phenomenon of enstrophy production/ depression (vortex stretching) $2\omega_i\omega_j S_{ij}$ and the viscous phenomena of enstrophy diffusion $\nu\partial^2\omega^2/\partial x_j \partial x_j$ and enstrophy dissipation $-2\nu(\partial\omega_i/\partial x_j)(\partial\omega_i/\partial x_j)$.

Similar to enstrophy, total strain is defined as $S^2 = S_{ij}S_{ij}$. Total strain plays an important role in the dynamics of turbulence as it is directly connected to kinetic energy dissipation of fluid elements and turbulent structures. Evolution of total strain follows equation 2.8:

$$\frac{DS^2}{Dt} = -2S_{ij}S_{jk}S_{ki} - \frac{1}{2}\omega_i\omega_j S_{ij} - 2S_{ij}\frac{\partial^2 P}{\partial x_i \partial x_j} + 2\nu S_{ij}\nabla^2 S_{ij} \tag{2.8}$$

The term $-2S_{ij}S_{jk}S_{ki} - (1/2)\omega_i\omega_j S_{ij} - 2S_{ij}(\partial^2 P/(\partial x_i \partial x_j))$ on the right hand side of equation 2.8 is called inviscid production of total strain, similar to the inviscid enstrophy production term $2\omega_i\omega_j S_{ij}$ in equation 2.7. In homogeneous turbulence, it can be shown that on average $\langle -2S_{ij}S_{jk}S_{ki} - (1/2)\omega_i\omega_j S_{ij}\rangle = \langle \omega_i\omega_j S_{ij}\rangle > 0$ are strictly positive, whereas $\langle S_{ij}(\partial^2 P/(\partial x_i \partial x_j))\rangle = 0$. Therefore, these inviscid terms generate total strain and enstrophy within the flow when we consider the average picture of homogenous turbulence [Betchov, 1956; Taylor, 1938a; Tsinober, 2009].

2.2 Statistical approach to turbulence

Even though the Navier-Stokes equation is deterministic, it can only be solved analytically for simplified flows at low Reynolds numbers, i.e. laminar flow. By increasing the Reynolds number sufficiently, the flow becomes turbulent where the velocity field shows chaotic behavior. This was first studied in the pioneering experiments of Reynolds [1883] in a tube as shown in figure 2.1. Reynolds injected dye at the inlet of a tube flow. He observed that when flow velocity was low, the dye followed a straight line in the tube. However, when he increased the flow velocity the dye pattern became wavy and eventually random. Reynolds proposed that this random velocity can be treated as fluctuations around a mean value. This led to Reynolds decomposition in equation 2.9:

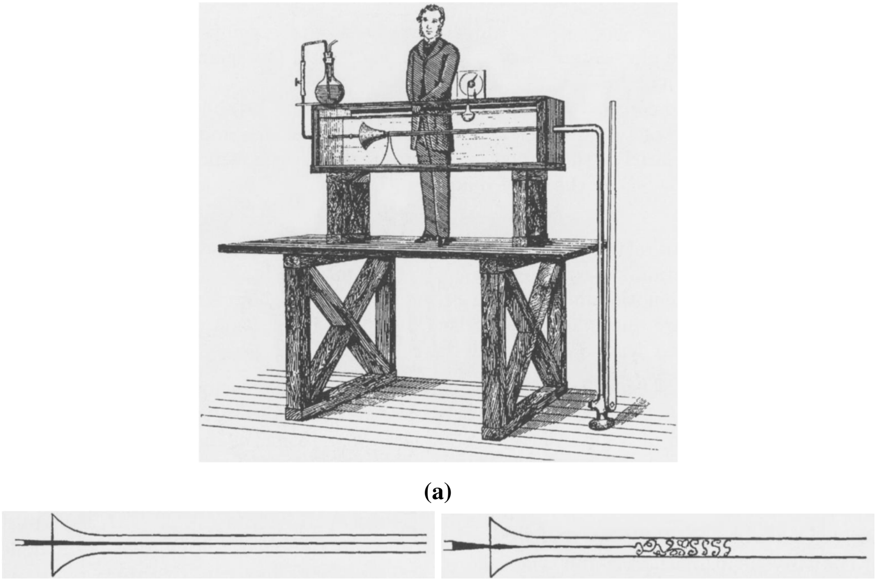

(a)

(b)

(c)

Figure 2.1: Reynolds' pioneering experiments on transition from laminar to turbulent flow in a tube; (a) sketch of the setup, (b) injected dye follows a straight line at low velocity (laminar flow), and (c) by increasing the flow velocity, the dye pattern becomes wavy and eventually random (turbulent flow). Source: Reynolds [1883].

$$U_i(x_j,t) = \langle U_i \rangle + u_i(x_j,t) \tag{2.9}$$

where $U_i(x_j,t)$ is the instantaneous velocity, $\langle U_i \rangle$ is the ensemble average velocity, and $u_i(x_j,t)$ is the velocity fluctuations. This decomposition provides a useful statistical approach to study stationary turbulence and is illustrated schematically in figure 2.2. The instantaneous velocity in this figure $U_i(t)$, fluctuates around a mean value over time. The same procedure can be used for other quantities. For example, the pressure field can be decomposed as $P(x_j,t) = \langle P \rangle + p(x_j,t)$.

Reynolds [1895] applied the decomposition to the Navier-Stokes equation to derive an average momentum equation for steady turbulence known as Reynolds average Navier-Stokes (RANS) equation in 2.10:

$$\frac{\partial \langle U_i \rangle}{\partial t} + \langle U_j \rangle \frac{\partial \langle U_i \rangle}{\partial x_j} = -\frac{1}{\rho}\frac{\partial \langle P \rangle}{\partial x_i} + \nu \frac{\partial^2 \langle U_i \rangle}{\partial x_j^2} - \frac{\partial \langle u_i u_j \rangle}{\partial x_j} \tag{2.10}$$

Equation 2.10 is similar to the Navier-Stokes equation in 2.2, except for an extra

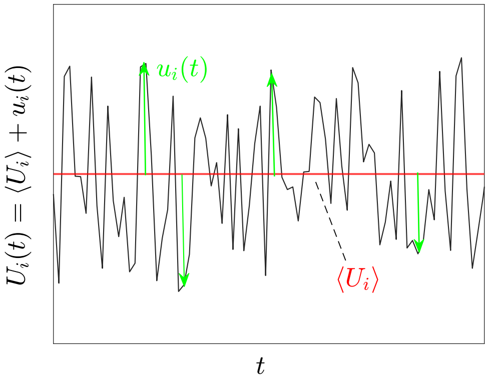

Figure 2.2: Instantaneous velocity of stationary turbulence $U_i(t)$ fluctuates $u_i(t)$ around a mean value $\langle U_i \rangle$ over time.

term $-\partial \langle u_i u_j \rangle / \partial x_j$ that only appears in the RANS equation. The term is known as the Reynolds stresses. Appearance of the Reynolds stresses leads to a closure problem in the system of equations as there are more unknowns than equations. In a steady 3D turbulence four equations exist, the RANS equations in each direction and one equation for continuity. However, we have more than four unknowns, average velocities in each direction, average pressure and the Reynolds stresses. This makes the RANS equations unsolvable unless extra information about the Reynolds stresses is provided or assumed. Therefore, the statistical approach in turbulence necessarily leads to the closure problem, which requires ad-hoc hypotheses or assumptions to close the system of equations.

By taking a statistical approach we moved from a deterministic system of equations to an under-determined system. The Navier-Stokes equation is deterministic but produces quantities, U_i and P , with chaotic behavior at high Reynolds numbers. However, the quantities of interest in the statistical approach, for example $\langle u_i u_j \rangle$, do not show random behavior and are reproducible in any experiment [Davidson, 2015].

Using Reynolds decomposition one can assess how turbulent the flow is; the root mean square (r.m.s.) of the velocity fluctuation field, u'_i, is defined in equation 2.11 and the turbulent kinetic energy (TKE), k, is defined in equation 2.12:

$$r.m.s.(u_i) = u'_i = \langle u_i^2 \rangle^{1/2} \tag{2.11}$$

$$k = \frac{1}{2} \langle u_i u_i \rangle \tag{2.12}$$

The evolution of TKE follows equation 2.13 and is governed by transport, production, and dissipation terms (equations 2.14-2.16):

$$\frac{\partial k}{\partial t} + \langle U_i \rangle \frac{\partial k}{\partial x_i} + \frac{\partial T'_i}{\partial x_i} = \mathscr{P} - \langle \varepsilon \rangle \tag{2.13}$$

where:

$$T'_i = \frac{1}{2}\langle u_i u_j u_j \rangle + \langle u_i p \rangle / \rho - 2\nu \langle u_j s_{ij} \rangle \ : transport \tag{2.14}$$

$$\mathscr{P} = -\langle u_i u_j \rangle \frac{\partial \langle U_i \rangle}{\partial x_j} \ : production \tag{2.15}$$

$$\langle \varepsilon \rangle = 2\nu \langle s_{ij} s_{ij} \rangle \ : dissipation \tag{2.16}$$

Equation 2.13 indicates that the material derivative of TKE, $Dk/Dt = \partial k/\partial t + \langle U_i \rangle \partial k/\partial x_i$ is balanced by three phenomena: (i) the production term $\mathscr{P}$ in equation 2.15 generally transfers energy from the mean flow to the turbulence, (ii) the dissipation term $\langle \varepsilon \rangle$ in equation 2.16 drains the energy of turbulence and dissipates it into heat, and (iii) the transport term $\partial T'_i/\partial x_i$ in equation 2.14 spatially redistributes TKE within the flow via motion of turbulent eddies, pressure perturbations, and viscous stresses.

2.3 Homogeneity and isotropy

Taking the statistical approach in turbulence leads to quantities that are non-random and reproducible. This is a big advantage compared to the chaotic behavior of the variables in the non-statistical approach. However, one needs to use some assumptions or hypotheses to address the closure problem in the statistical approach. Homogeneity and isotropy are examples of such assumptions that have been widely used in the statistical approach. Taylor [1938a] and Batchelor [1946] defined and used these concepts for velocity fluctuations u_i, whereas Kolmogorov [1941b] used them for velocity increments $\delta u_i(x,r) = u_i(x+r) - u_i(x)$. Here, we present and adopt the definition of local homogeneity/ isotropy provided by Monin and Yaglom [1975] based on the velocity increments. In this definition, turbulence is locally homogeneous when statistical properties of the velocity increment are independent of position x in space. Local isotropy holds when in addition to the local homogeneity, the statistical properties of the velocity increment are invariant under all rotations and projections of the coordinate axes within the flow.

Perfectly homogeneous isotropic turbulence (HIT) does not exist in nature and engineering applications, but grid turbulence in wind tunnels is a good approximation for HIT in its spanwise direction and has been used extensively over the past few decades to study turbulence. In addition, the theory of turbulence is based on HIT. To provide some examples of the resulting simplifications, the average product of fluctuations in different directions are zero, $\langle u_i u_j \rangle = 0$ and the average dissipation rate simplifies to $\langle \varepsilon \rangle = 15\nu \langle (\partial u_1 / \partial x_1)^2 \rangle$. Equation 2.13 for the evolution of TKE, takes its simplest form $\partial k / \partial t = -\langle \varepsilon \rangle$ as the transport and production terms become zero. The main reasons behind the popularity of HIT in turbulence research can be summarized to: (i) it is a simplified version of real flow that is easier to work with in analytical theories and (ii) it does not have a fingerprint of often linear external forcing resulting from mean shear, buoyancy, etc. in real flow. These fingerprints are difficult to separate from the nonlinear behavior of turbulence which is assumed to be at least partially universal [Tsinober, 2009].

2.4 The energy cascade and scales in turbulence

The concept of the energy cascade is the bedrock of the turbulence theory. It was first conceptualized by Richardson [1926] and later on formulated and theorized by Kolmogorov [1941b]. These are shown schematically in figures 2.3 and 2.4. It states that, on average, energy is externally injected into the flow at the largest scale $\mathscr{L}_0$, whose size is comparable to a characteristic length of the flow geometry. This is shown by energy containing range in figure 2.4. The injected energy cascades down internally, into the universal equilibrium range, toward increasingly smaller scales. The process continues until it reaches the end of the cascade, where the energy dissipates into heat at the smallest scale through action of viscosity. This is known as dissipation or Kolmogorov length-scale, η. If one considers that there is a large enough separation between large and small-scales, the length-scales involved in the universal equilibrium range can be divided into two subranges; (i) the inertial subrange where the viscous phenomena are negligible and the strain field of the flow transfers the energy to the smaller scales by inviscid mechanisms, and (ii) the viscous or dissipation subrange where the viscous phenomena become significant enough and eventually dominant. These are shown in figure 2.4. Kolmogorov [1941b] hypothesized that the motion of the flow at the smallest scales is self-similar and only depends on two parameters; kinematic viscosity ν and dissipation rate ε. Consequently, Kolmogorov length η, time τ_η, and velocity u_η scales are defined in equations 2.17-2.19:

$$\eta = \left(\frac{\nu^3}{\varepsilon} \right)^{1/4} \tag{2.17}$$

$$\tau_\eta = \left(\frac{\nu}{\varepsilon} \right)^{1/2} \tag{2.18}$$

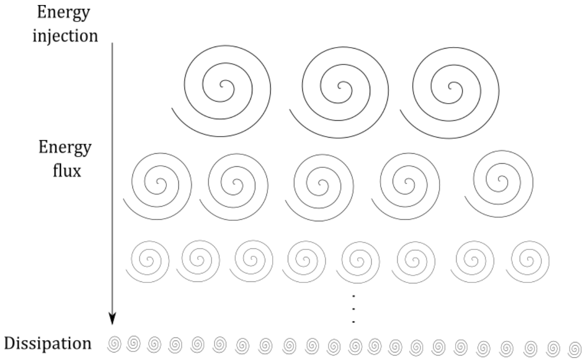

Figure 2.3: Based on the Richardson-Kolmogorov picture of turbulence, kinetic energy cascades down toward the smaller scales on average. This process continues until the dissipation scale, where the kinetic energy is dissipated into heat.

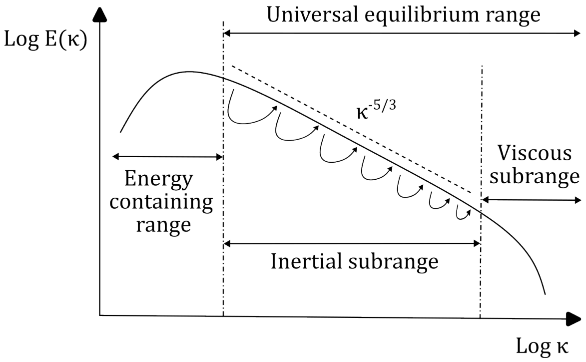

Figure 2.4: Energy spectrum of turbulence (the energy cascade) based on wavenumber $E(\kappa)$ and the related subranges. The spectrum follows Kolmogorov's -5/3 law in the inertial subrange.

$$u_\eta = (\nu\varepsilon)^{1/4} \tag{2.19}$$

The rate of the energy injected into the flow can be estimated as $\mathscr{U}_0^2/\mathscr{T}_0 = \mathscr{U}_0^3/\mathscr{L}_0$ where $\mathscr{U}_0$, $\mathscr{L}_0$, and $\mathscr{T}_0$ are the characteristic velocity, length, and time scales at the large-scale. Since this energy rate is equal to the dissipation rate at the smallest scale, following the Kolmogorov theory, the scaling argument $\varepsilon \sim \mathscr{U}_0^3/\mathscr{L}_0$ is valid and is used to find a relation that estimates the ratio between the smallest and the largest scales of turbulence (scale separation) in equation 2.20:

$$\frac{\eta}{\mathscr{L}_0} \sim Re^{-3/4} \tag{2.20}$$

Equation 2.20 suggests that by increasing the Reynolds number $Re = \mathscr{U}_0\mathscr{L}_0/\nu$ in the same facility, i.e. fixed $\mathscr{L}_0$, the Kolmogorov length-scale becomes continuously smaller and a wider range of scale separation can be achieved. However, the decrease in the Kolmogorov length-scale poses a challenge as it makes the experimental measurements of the small-scales difficult.

Another widely used length-scale in turbulence is Taylor micro-scale, λ, defined in equation 2.21 for homogeneous isotropic turbulence (HIT). This length-scale belongs to the inertial sub-range $\eta \ll \lambda \ll \mathscr{L}_0$, but it does not have a clear physical interpretation [Pope, 2000]. The Reynolds number based on the Taylor micro-scale R_λ is consequently defined in equation 2.22.

$$\lambda = u'\sqrt{\frac{15\nu}{\langle\varepsilon\rangle}} \tag{2.21}$$

$$R_\lambda = \frac{u'\lambda}{\nu} \tag{2.22}$$

The Kolmogorov theory of turbulence is based on the velocity increments $\delta u_i(x,r) = u_i(x+r) - u_i(x)$, instead of velocity fluctuations itself. The velocity increments of different orders are represented by the p-order structure function in equation 2.23. The Kolmogorov theory predicts that equations 2.24 and 2.25 should hold for the second and third order structure functions in the inertial subrange, $\eta \ll r \ll \mathscr{L}_0$, at high Reynolds numbers. Equation 2.24 is known as Kolmogorov's $2/3$ law in physical space or equivalently, $-5/3$ law in Fourier space based on wavenumber as shown in figure 2.4. In these formulations, C_2 and C_K were believed to be absolute constants valid for any turbulent flow at high enough Reynolds numbers. Equation

2.25 is usually referred to as Kolmogorov's $-4/5$ law. These equations indicate the distribution and fluxes of turbulent kinetic energy among different scales of flow motion within the inertial subrange. They can also be used to estimate the dissipation rate of the flow, when highly resolved velocity field is not available to calculate the dissipation rate directly.

$$S_p(r) = \left\langle \left([\mathbf{u}(\mathbf{x}+\mathbf{r}) - \mathbf{u}(\mathbf{x})] \cdot \frac{\mathbf{r}}{r} \right)^p \right\rangle \tag{2.23}$$

$$S_2(r) = C_2 \langle \varepsilon \rangle^{2/3} r^{2/3} \Leftrightarrow E(\kappa) = C_K \langle \varepsilon \rangle^{2/3} \kappa^{-5/3} \tag{2.24}$$

$$S_3(r) = -\frac{4}{5} \langle \varepsilon \rangle r \tag{2.25}$$

To identify and measure turbulent structures, the two-point correlation of the velocity fluctuations is defined in equation 2.26 for homogeneous turbulence ($R_{ij}(x,r,t) = R_{ij}(r,t)$):

$$R_{ij}(r,t) = \langle u_i(x+r,t) u_j(x,t) \rangle \tag{2.26}$$

The integral length-scale is then defined as the area under the curve of the normalized two-point correlation function in equation 2.27. The integral length-scale is a good approximation for the average size of the largest coherent motions (eddies) within the flow field. The integrand in equation 2.27, $R_{ij}(r,t)/R_{ij}(0,t)$, decays from 1 at $r = 0$ to 0 at $r = \infty$. Therefore, the integral is bounded. However, it is not usually practical to reach large distances due to the limited spatial extent of the measurements or numerical simulations. A solution has been proposed by De Jong et al. [2009] in which an exponential decay function is fitted to the available profile of $R_{ij}(r,t)/R_{ij}(0,t)$ in the range $0 < r < r_{max}$. The fit extrapolates the missing tail, i.e. $A\exp(-Br)$ in the range $r_{max} < r < \infty$.

$$L_{ij}(t) = \int_0^\infty \frac{R_{ij}(r,t)}{R_{ij}(0,t)} \, \mathrm{d}r = \int_0^{r_{max}} \frac{R_{ij}(r,t)}{R_{ij}(0,t)} \, \mathrm{d}r + \int_{r_{max}}^\infty A\exp(-Br) \, \mathrm{d}r \tag{2.27}$$

2.5 The dynamics of the small-scales of turbulence

"*This suggests that the most important processes associated with production of vorticity and energy transfer resemble a jet collision and not the swirling of a contracting jet.*" Betchov [1956]

The most prominent features of turbulence are the rotation of fluid elements and the dissipation of kinetic energy. These two features are interconnected through the velocity gradient tensor (VGT), $A_{ij} = \partial u_i / \partial x_j$, where the rate of strain tensor (dissipation) $S_{ij} = (A_{ij} + A_{ij}^T)/2$ is the symmetric part and the rotation tensor $W_{ij} = (A_{ij} - A_{ij}^T)/2$ is the antisymmetric part of VGT, $A_{ij} = S_{ij} + W_{ij}$. The velocity field can be fully determined by the vorticity field ($\nabla^2 u_i = -(\nabla \times \omega)_i$) or the strain field ($\nabla^2 u_i = 2\partial s_{ij}/\partial x_j$) along with appropriate boundary conditions. However, the connection between the fields of vorticity and strain is strongly nonlocal and turbulence statistics show that they are weakly correlated in space.

Since the seminal studies of Taylor [1937, 1938a] and Kolmogorov [1941a,b], velocity gradients have been used extensively to investigate the dynamics of turbulence and the energy cascade. The velocity gradients determine the structures of vorticity and strain, along with their interactions in the universal equilibrium range. Thus, after the flow becomes self-similar (the universal equilibrium range) the mechanisms of turbulence are fully governed by VGT. For example, dissipation which is commonly agreed to be the final stage of the energy cascade process is represented by the symmetric part of VGT, i.e. the field of strain $\varepsilon = 2\nu s_{ij} s_{ij} = 2\nu s^2$.

The nonlinear interaction between the vorticity and strain fields results in the inviscid phenomenon of vortex stretching/ compression. Vortex stretching produces enstrophy on average, $\langle \omega_i \omega_j s_{ij} \rangle > 0$, which was first discovered in the theoretical study of HIT by Taylor [1938a]. It turns out that 3D turbulence cannot exist (or sustain itself) without a net production of enstrophy. Even though vortex stretching/ enstrophy production is an important process in turbulence dynamics, it is not the leading agent in the energy cascade. The energy cascade and dissipation in particular are strongly associated with the self-amplification of the rate of strain and vortex compression rather than vortex stretching as discovered by Betchov [1956]. In addition to $\langle \omega_i \omega_j s_{ij} \rangle$ being positive, the self-production of strain $-\langle s_{ij} s_{jk} s_{ki} \rangle$ in equation 2.8 is also positive in turbulent flows on average. Since the enstrophy production term appears with a negative sign in this equation, it works on average as a sink term that drains the energy of strain (dissipation), s^2. Thus, enstrophy production/ vortex stretching suppresses the energy cascade and it does not act in favor of it, as suggested by Taylor [1938a].

Self-amplification of the velocity derivatives both in the shape of enstrophy production and production of total strain is an intrinsic feature of turbulence. It is worth mentioning that these productions are orders of magnitude higher than the productions directly resulting from the external forcing. This can be checked in DNS studies of HIT boxes where the flow is commonly forced by activating an external body force term, f, in the Navier-Stokes equation. This external body force appears in the equations for the evolution of total strain and enstrophy as $s_{ij}f_{ij}$ and $\omega_i(\nabla \times f)_i$ terms, respectively. It turns out that in the range of moderate to high Reynolds numbers, the magnitudes of these terms are orders of magnitude smaller than the magnitudes of the self-amplification terms. This difference increases with Reynolds number [Tsinober, 2009]. Thus, the self-amplification of velocity gradients, i.e. production of enstrophy and total strain, is a universal feature of turbulence and independent from the external forcing at the large-scales.

Another important feature of self-amplification is that it is quasi-stationary in time. This means when the whole volume of flow considered, the production of enstrophy or total strain is balanced by the viscous destruction of these quantities at any time instant. This is a result of Tennekes and Lumley (TL) balance, i.e. $\langle \omega_i \omega_j s_{ij} \rangle \approx -\nu \langle \omega_i \nabla^2 \omega_i \rangle$ in homogeneous turbulence [Tsinober, 2009]. Therefore, the time derivative of the overall enstrophy or total strain is significantly smaller than the corresponding production and destruction values.

When geometrical statistics of the small-scales are considered, certain features appear to be valid in a wide range of turbulent flows. The preferential alignment between the vorticity vector and the direction of intermediate principal strain was first discovered in DNS of HIT by Kerr [1985] and Ashurst et al. [1987] and has been observed in many other studies afterward, both numerically and experimentally. Some examples of such an alignment are shown in figure 2.5 from the studies of Elsinga and Marusic [2010] in a turbulent boundary layer, Buxton and Ganapathisubramani [2010] in an axisymmetric turbulent jet, and Buaria et al. [2020] in DNS of forced isotropic turbulence. The results show a preferential alignment between the vorticity vector and the intermediate principal direction, whereas a tendency to orient normally to the compressive principal direction is observed. The intermediate eigenvalue is positive on average. Therefore, the alignment leads to production of enstrophy via vortex stretching.

Another geometrical feature that seems to be universal is the average radius of the small-scale vortex structures or so-called 'worms'. In the DNS study of Jiménez et al. [1993], the average radius was calculated and reported to be approximately 5η. Similar sizes have been observed by many experimental and numerical studies later on [da Silva et al., 2011; Ganapathisubramani et al., 2008; Ghira et al., 2022; Neamtu-Halic et al., 2021]. In addition, Jiménez et al. [1993] and Jiménez and Wray [1998] showed that these structures possess a low level of stretching and are relatively stable, i.e. they are frozen/ passive within the flow field. When the statistics of the alignment between the vorticity vector and the principal strain directions is conditioned inside the small-scale vortex structures, a strong tendency is observed for the vorticity vector to align with the intermediate eigendirection,

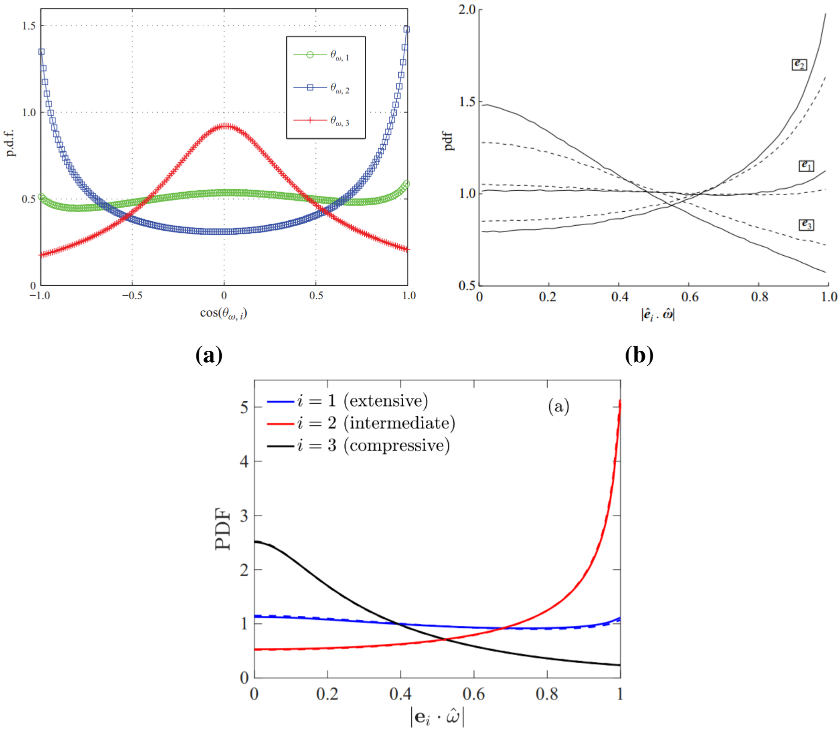

(a) **(b)**

(c)

Figure 2.5: Examples of probability distribution functions of cosine of the angles between the eigendirections of the rate of strain tensor and the vorticity vector. Here, $i = 1$ is the largest stretching, $i = 2$ is the intermediate, and $i = 3$ is the most compressive eigendirection: (a) turbulent boundary layer, source: Elsinga and Marusic [2010], (b) axisymmetric turbulent jet, source: Buxton and Ganapathisubramani [2010], and (c) DNS of forced isotropic turbulence, source: Buaria et al. [2020].

but being normal to the extensive and compressive eigendirections [Buaria et al., 2020; Frisch, 1995].

Self-amplification is a nonlinear process and is mostly associated with large strain, i.e. alignment between the largest strain and vorticity, and finite curvature of the vortex lines. Thus, the regions of the flow occupied by the structures of intense vorticity/ enstrophy (small-scale vortices or 'worms') are the regions with reduced nonlinearity and self-amplification is negligible in these regions. This means that small-scale vortex structures do not play a significant role in the overall dynamics of turbulence. On the other hand, structures of intense strain, where nonlinearity is maximized, are significant for turbulence dynamics and the cascade process.

As discussed in this subsection, vortices at the dissipation scale are considered insignificant in overall dynamics of turbulence due to their lack of self-amplification and being frozen in the flow field. However, are they active in other important aspects, for example, exchange of mass, momentum, and enstrophy with the background flow? We will investigate this question in Article 1.

2.6 The dynamics of the large-scales of turbulence

The Kolmogorov theory addresses certain fundamental questions in the small and intermediate range of scales in turbulence, the universal equilibrium range. However, it does not provide any information about the large-scales of turbulence, where the energy is injected into the flow. Large-scale dynamics are of practical importance in natural phenomena and engineering applications, but finding a universal theory at the large-scales is not possible. The reason is that the large-scale motions of turbulence have the characteristic size comparable to the size of the apparatus that the flow is generated in. Thus, they are partially determined by the flow geometry, boundary conditions, and the specific instabilities in the flow. In other words, these motions are case dependent and can change from one flow to another.

Numerous studies have been performed to investigate these motions in different flows, such as spanwise structures, hairpin vortices, and uniform momentum zones (UMZs) in boundary layers [Adrian, 2007; de Silva et al., 2016; Lee et al., 2017; Lee, 2017; Tomkins and Adrian, 2003], large-scale and very-large-scale motions (VLSMs) in pipe flows [Hellström et al., 2015, 2016; Kim and Adrian, 1999], quiescent cores, long motions of streamwise velocity fluctuations, and large-scale circulations in channel flows [Asadi et al., 2022; Hwang et al., 2016; Kwon et al., 2014; Lee et al., 2014; Liu et al., 2001; Zampiron et al., 2020], large-scale circulation (LSC) in turbulent Rayleigh-Bénard convection [Brown and Ahlers, 2009; Funfschilling and Ahlers, 2004; Mishra et al., 2011], and Taylor rolls in turbulent Taylor-Couette flows [Grossmann et al., 2016; Huisman et al., 2012; Ostilla-Mónico et al., 2014, 2016] to name just a few. In a nutshell, these studies show that the behavior of turbulence at the large-scale is quite nonlocal in time and space. This means turbulence (i) has a long memory of the past motions and (ii) is affected by the activities in the distant regions of the flow. For these reasons, large-scale turbulence shows a richer range of behaviors compared to the intermediate and small-scales [Pope, 2000].

One of the first attempts in understanding the dynamics of the large-scales was made by Loitsyansky. He claimed that an integral invariant in isotropic turbulence, $\mathscr{I}$ in equation 2.28, existed [Loitsiansky, 1939]. Later on, Landau indicated that this invariant was the consequence of conservation of angular momentum in the flow, i.e. a cloud of turbulent motion maintained its angular momentum as it evolved [Landau and Lifshitz, 1959].

$$\mathscr{I} = -\int r^2 \langle U_i u_i \rangle dr = constant. \tag{2.28}$$

Based on this hypothesis, Kolmogorov [1941a] derived a relation for freely decaying turbulence in equation 2.29, also known as Loitsyansky decay law. This equation indicates a temporal exponential decay of TKE (exponent: $-10/7 \approx -1.43$) and an exponential growth of the integral length-scale (exponent: $2/7 \approx 0.29$).

$$k(t) = \frac{1}{2} u_i u_i \sim t^{-10/7}, L(t) \sim t^{2/7} \tag{2.29}$$

In 1956, Batchelor proved that the assumption Loitsyansky made about the non-local effect of the pressure field to derive equation 2.28 was not always valid. Therefore, the claims about the Loitsyansky invariant became problematic. Batchelor showed that the pressure field can pass information through pressure waves between remote regions of the flow, in contrast with the assumption of Loitsyansky [Batchelor and Proudman, 1956]. Saffman showed that the integral in equation 2.28 diverges for some cases of isotropic turbulence [Saffman, 1967]. This was a solid end to the validity of the Loitsyansky invariant and thereafter has been called Loitsyansky integral. Nevertheless, this integral plays an important role in the energy transfer process. In Fourier space, the energy spectrum based on wavenumber $E(\kappa)$ can be approximated in equation 2.30 where $\mathscr{I}$ appears in the coefficient of the κ^4 term and $\mathscr{L}$ known as Saffman integral, defined in equation 2.31, appears in the coefficient of the κ^2 term. When the conservation of linear momentum is assumed, it can be shown that the Saffman integral, $\mathscr{L}$, is an invariant. However, this assumption is not generally valid.

$$E(\kappa) = \frac{\mathscr{L}\kappa^2}{4\pi^2} + \frac{\mathscr{I}\kappa^4}{24\pi^2} + \cdots \tag{2.30}$$

$$\mathscr{L} = \int \langle U_i u_i \rangle dr \tag{2.31}$$

When the conservation of angular momentum is assumed, $\mathscr{L} = 0$ and the energy spectra will be of the type $E(\kappa) \sim \mathscr{I}\kappa^4 + \cdots$, known as Batchhelor spectra or Batchelor turbulence. On the other hand, when the conservation of linear momentum is assumed, $\mathscr{L} \neq 0$ and the spectra will be of the type $E(\kappa) \sim \mathscr{L}\kappa^2 + \cdots$, known as Saffman spectra or Saffman turbulence. Similar to the Loitsyansky decay law in equation 2.29 in Batchelor turbulence, relations for the temporal decay of TKE ($k(t)$) and growth of the integral length-scale ($L(t)$) are derived for the free decay of Saffman turbulence in equation 2.32. Here, the decay exponent is $-6/5 = -1.2$ and the growth exponent is $2/5 = 0.4$:

$$k(t) \sim t^{-6/5}, L(t) \sim t^{2/5} \tag{2.32}$$

The most common way of studying turbulent decay experimentally is by passing a steady flow through a grid, shown in figure 2.6(a), and measuring the flow velocity field downstream as exemplified in the seminal work of Batchelor and Townsend [1948], where it was shown that the decay of grid turbulence follows a power-law decay function. For downstream of the grid, the flow is homogeneous in spanwise direction and the TKE decays with streamwise distance. When only point measurements are available, Taylor's frozen flow hypothesis [Taylor, 1938b] can be used to perform a linear conversion of the measured spatial data into temporal data. Taylor's hypothesis states that when the mean flow is significantly higher than the fluctuations, turbulent structures or eddies are advected by the mean flow and do not evolve over short distances.

After the original work of Batchelor and Townsend [1948], decay of grid turbulence has been extensively studied in wind tunnel experiments. Comte-Bellot and Corrsin [1966] found the decay exponent to lie within the range $[-1.29, -1.15]$ and Warhaft and Lumley [1978] estimated it to be -1.34. More recently, Krogstad and Davidson [2009, 2011] used classical and multi-scale grids, shown in figure 2.6(b), to investigate the decay of homogeneous turbulence in a large wind tunnel facility. They found the Saffman decay exponent ($k \sim t^{-1.2}$) sufficiently downstream from the grids in both cases. Sinhuber et al. [2015] used a classical grid to study the decay of moderate to high Reynolds numbers homogeneous flow ($10^4 < Re < 5 \times 10^6$) using a low-viscosity fluid. They also reported the Saffman

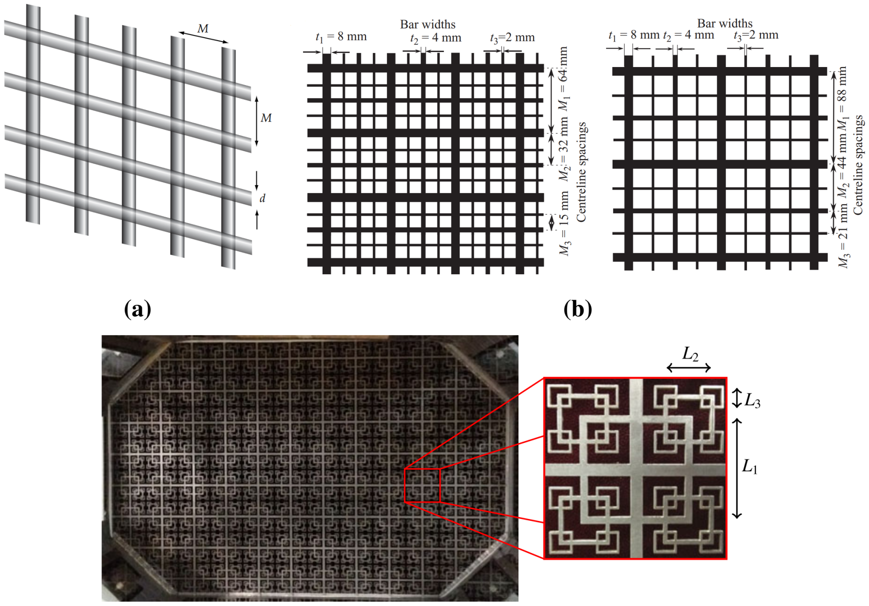

(a) **(b)**

(c)

Figure 2.6: Grid turbulence; (a) schematic of a classical square mesh grid made of bars with diameter d and mesh size M, source: Pope [2000], (b) schematic of multi-scale grids, source: Krogstad and Davidson [2011], (c) a square-fractal-element grid, source:Hearst and Lavoie [2014].

decay exponent within the range of the Reynolds numbers studied. The decay has also been measured after fractal grids. It started with the study of Hurst and Vassilicos [2007] where a very rapid exponential decay was reported after the grid and George and Wang [2009] proposed an analytical solution for decay that was in agreement with the observed exponential behavior. However, measurements of Valente and Vassilicos [2011] showed that the flow after the fractal grids followed a power-law decay with a high exponent of $n \approx -2.5$. In another study, Hearst and Lavoie [2014] studied a square-fractal-element grid shown in figure 2.6(c). The grid pattern and its dimensions were designed proportional to the size of the wind tunnel. This enabled the emergence of different regimes of decay downstream of the grid. They found a decay exponent of -1.38 ($k \sim t^{-1.38}$), far away from the grid which is close to the Loitsyansky prediction of -1.43. However, the decay exponent was reported to be -2.79 in the near grid region. The authors stated that this rapid decay was due to poor transverse homogeneity of the mean flow close to the grid.

In addition to the wind tunnel grid experiments, the free decay of turbulence can be studied in other flow configurations which produce homogeneous flow. Esteban et al. [2019] studied the decay of homogeneous anisotropic turbulence generated by Random Jet Arrays (RJAs) with zero-mean flow and high fluctuations. They identified three consecutive regimes of decay within their measurements; (i) during the initial period, a quick decay rate was observed with an exponent of -2.3, (ii) a classical Loitsyansky decay regime emerged with an exponent of -1.4, (iii) the final decay regime appeared with an exponent of -1.8. They showed that the final regime was caused by the finite size of the facility and that this confinement prevented the continuous growth of the integral length-scale. This effect is known as saturation or confinement effect in the decay literature [Panickacheril John et al., 2022; Skrbek and Stalp, 2000].

Freely decaying turbulence has also been studied numerically using DNS in HIT boxes with periodic boundary conditions. Panickacheril John et al. [2022] gathered and reviewed the decay exponents available in the literature with a focus on DNS studies. The collected decay exponents vary by 100% among different studies and lie somewhere within the range $[-2,-1]$. The authors concluded that the initial condition and the arbitrariness in identifying the virtual origin (used to fit the power-law decay function) were the main reasons behind these variations.

The studies available on decay measurements in homogeneous flows with near zero mean are very limited and to the best of author's knowledge do not exist in von Kármán swirling flows. We will investigate the decay behavior in a von Kármán swirling flow in Article 2. In addition, dynamics of large-scale motions in the flow are not well-studied and in Article 3 we will investigate the effects of Reynolds number and forcing strategy on these dynamics.

2.7 Entrainment and detrainment of turbulent mixing

An important feature of turbulent flows at the small-scales is intermittency as shown in the pioneering work of Batchelor and Townsend [1949]. This means the flow field is occupied locally and non-uniformly by turbulent structures, i.e. small-scale vortices, embedded in a less active (less rotational) background fluid. As discussed earlier in the dynamics of the small-scales, the vortex structures are passive and not significant in the overall dynamics of turbulence. However, they can be significant when one considers their interactions with the background fluid to exchange mass, momentum, and enstrophy across the vortex boundary. This can be investigated by adopting a methodological approach used in the study of turbulent non-turbulent interface (TNTI) [Holzner and Lüthi, 2011; Kankanwadi and Buxton, 2022; Mathew and Basu, 2002; Mistry et al., 2016, 2019; Neamtu-Halic et al., 2019, 2020; Westerweel et al., 2005; Wolf et al., 2012].

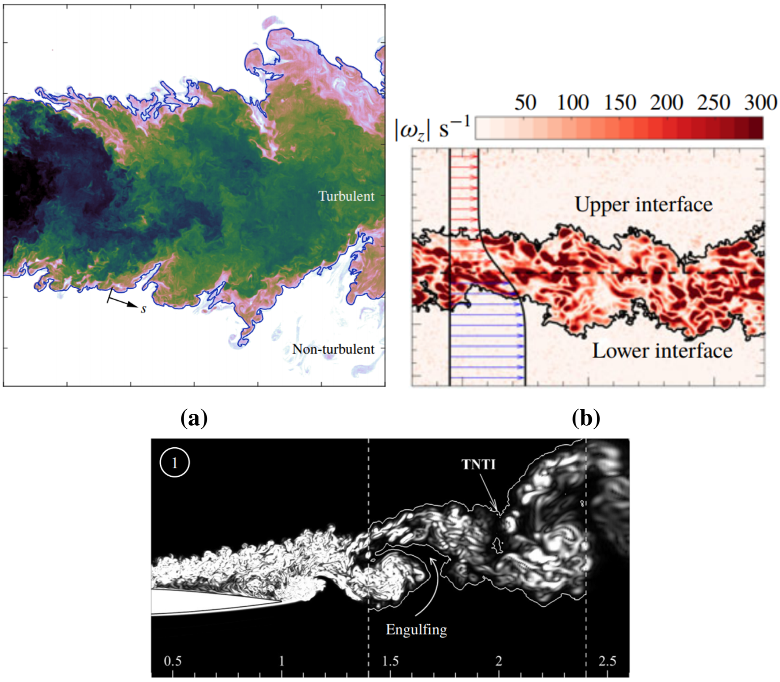

(a) **(b)**

(c)

Figure 2.7: Examples of TNTI in: (a) turbulent jet, source: Mistry et al. [2016], (b) turbulent mixing layer, source: Balamurugan et al. [2020], and (c) turbulent wake after an airfoil, source: Zhang and Wu [2022].

In this section, we briefly introduce local entrainment across TNTI which plays an important role in transfer of mass and momentum. The coexistence and interaction between turbulent and irrotational non-turbulent regions are important phenomena in turbulence. These two regions are separated by a sharp and highly contorted interface known as turbulent non-turbulent interface (TNTI). The interactions through the interface are observable in a variety of flow configurations both in nature and engineering applications, e.g. jets, wakes, and mixing layers shown in figure 2.7 just to mention a few.

In the seminal study of entrainment in a turbulent jet by Westerweel et al. [2005], it was shown that a finite jump in the tangential velocity existed at the interface between the turbulent and non-turbulent regions. This jump contributed to propagation of the interface toward the non-turbulent region by inducing small-scale eddy motions in the irrational fluid (viscous nibbling). This resulted in the conclusion that the non-viscous process of large-scale engulfment is not a dominant phenomenon in local entrainment physics. Later, Holzner and Lüthi [2011]

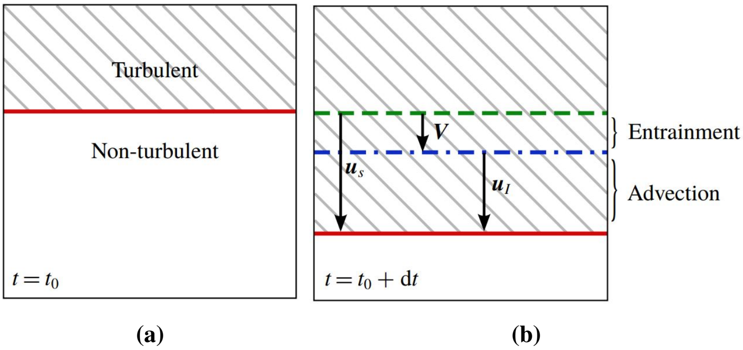

Figure 2.8: Schematic of the evolution of TNTI between time step t_0 in (a) and $t_0 + dt$ in (b). The movement of the interface (TNTI) is the superposition of the entrainment and local fluid velocity at the interface (advection). Source: Mistry et al. [2019].

proved the existence of a laminar superlayer at the interface, which was initially proposed by Corrsin and Kistler [1955], with a thickness and local velocity comparable to the Kolmogorov scales that controls the entrainment process. They showed that the small local velocity of the laminar superlayer is compensated by the large contorted area of the interface which keeps the overall rate of entrainment independent of the flow viscosity, but governed by the non-viscous motions of large-scale eddies.

The entrainment velocity is defined as the relative velocity normal to the TNTI, $V = v_n n = u_s - u_I$ where u_s is the velocity of the interface and u_I is the local velocity of the fluid at the interface. This is shown in figure 2.8. The unit vector $n = \nabla\omega^2/|\nabla\omega^2|$ denotes the normal vector at TNTI , an iso-surface of enstrophy, that points toward the turbulent region. Here, $v_n \leq 0$ means entrainment of the irrotational non-turbulent fluid into the turbulent region, while $v_n > 0$ indicates that the fluid elements in the turbulent region are detrained out to the non-turbulent region across TNTI [Mistry et al., 2019].

Given that TNTI is an iso-surface of enstrophy, i.e. $D_s\omega^2/D_st = 0$, Holzner and Lüthi [2011] derived equations 2.33 and 2.34 for evolution of the TNTI. By combining equation 2.34 and the enstrophy transport equation 2.7, they derived equation 2.35 for the entrainment velocity across TNTI as:

$$\frac{D_s\omega^2}{D_st} = \frac{\partial\omega^2}{\partial t} + u_{s,j}\frac{\partial\omega^2}{\partial x_j} = \frac{\partial\omega^2}{\partial t} + (V_j + u_{I,j})\frac{\partial\omega^2}{\partial x_j} = 0 \qquad (2.33)$$

$$\frac{\partial \omega^2}{\partial t} + u_{I,j}\frac{\partial \omega^2}{\partial x_j} = -V_j\frac{\partial \omega^2}{\partial x_j} = -v_n|\nabla \omega^2| \tag{2.34}$$

$$v_n = -\frac{2\omega_i\omega_j s_{ij}}{|\nabla \omega^2|} - \frac{\nu\frac{\partial^2 \omega^2}{\partial x_j \partial x_j}}{|\nabla \omega^2|} + \frac{2\nu\frac{\partial \omega_i}{\partial x_j}\frac{\partial \omega_i}{\partial x_j}}{|\nabla \omega^2|} \tag{2.35}$$

Even though this equation was initially derived to calculate the entrainment velocity across TNTI, it can also be applied on any iso-surface of enstrophy within the flow field ($D_s\omega^2/D_st = 0$). The obtained velocity can be physically interpreted as the relative flow velocity, i.e. the flow velocity observed by the observer moving with the iso-surface. Equation 2.35 will be used in Article 1 to evaluate the entrainment/ detrainment behavior at the boundary of the vortices.

2.8 Some stochastic methods to study turbulence

2.8.1 Cross-correlation and auto-correlation of time signals

The cross-correlation of two time signals is a measure of the similarity between them when one signal is shifted with respect to the other one. The mathematical formulation is presented in equation 2.36. In this equation, ρ_{FG} is the normalized cross-correlation of the signals $F(t) = \langle F\rangle + f(t)$ and $G(t) = \langle G\rangle + g(t)$ as a function of the signal shift, s. When the cross-correlation is performed with the same signal, it is called auto-correlation in equation 2.37. Based on these normalized definitions, $-1 \leq \rho_{FG}(s) \leq 1$ and $\rho_{FF}(0) = 1$.

$$\rho_{FG}(s) = \frac{\langle f(t)g(t+s)\rangle}{\sqrt{\langle f^2(t)\rangle\langle g^2(t)\rangle}} \tag{2.36}$$

$$\rho_{FF}(s) = \frac{\langle f(t)f(t+s)\rangle}{\langle f^2(t)\rangle} \tag{2.37}$$

2.8.2 Power spectral density (PSD)

In certain problems, it is useful to present a time signal in frequency domain, i.e. Fourier space. This becomes specially relevant when harmonic motions are involved in the time signal. Power spectral density (PSD) expresses the energy distribution of a time signal in Fourier space. Therefore, PSD analysis facilitates the assessment of the frequencies that are connected to the energetic harmonic motions and their significance based on the amplitudes. PSD of a velocity fluctuation signal, ψ_{uu}, is defined as the Fourier transform of the auto-correlation of that signal (non-normalized) in the time domain in equation 2.38. Using Parseval theorem and given that PSD is an even function of frequency f, equation 2.39 is derived. This equation indicates that the kinetic energy distribution of the velocity fluctuation signal in time, $u^2(t)$, is represented by PSD in frequency domain, $\psi_{uu}(f)$.

$$\psi_{uu}(f) = \int_{-\infty}^{\infty} \rho_{uu}(s) \langle u^2(t) \rangle \, e^{-i2\pi f s} \, ds \tag{2.38}$$

$$\langle u^2(t) \rangle = 2 \int_{0}^{\infty} \psi_{uu}(f) \, df \tag{2.39}$$

2.8.3 Proper orthogonal decomposition (POD)

As mentioned earlier, two-point velocity correlations are useful to study turbulence. They can be interpreted as an indication of coherent motions or structures within the flow. Proper orthogonal decomposition (POD) is a model order reduction technique that uses two-point velocity correlations to decompose the flow field into characteristic flow motions in space, i.e. modes $\Phi_n(x_j)$. Each of these modes are modulated by a time coefficient, $a_n(t)$ in equation 2.40. These characteristic motions are orthonormal spatial functions, equation 2.41, resulting from eigenvalue analysis. Using the definition of POD in equation 2.40 combined with the orthonormal property of the deterministic spatial functions in equation 2.41, equation 2.42 is derived for the coefficients. The modes are ordered based on the average kinetic energy in a descending order, i.e. mode $n = 1$ is the most energetic. The kinetic energy of each mode in time can be simply calculated as $a_n^2(t)$ because the modes (spatial functions) are orthonormal (equation 2.41). Therefore, the kinetic energy of the flow is equal to the summation of the average kinetic energy of the modes in equation 2.43. In the present work, economy-size singular value decomposition (SVD) is used to calculate the POD modes and their time coefficients from the velocity fluctuations. We refer the interested reader to Brunton and Kutz [2022] for a detailed discussion about POD and the calculation methods.

$$u_i(x_j,t) = \sum_{n=1}^{\infty} a_n(t) \, \Phi_n(x_j) \tag{2.40}$$

$$\iiint_V \Phi_n(x_j)\Phi_m(x_j) \, dV = \left\{ \begin{array}{lll} 0 & \text{for} & n \neq m \\ 1 & \text{for} & n = m \end{array} \right. \tag{2.41}$$

$$a_n(t) = \iiint_V u_i(x_j,t) \, \Phi_n(x_j) \, dV \tag{2.42}$$

$$k = \frac{1}{2}\langle u_i u_i \rangle = \frac{1}{2}\sum_{n=1}^{\infty}\langle a_n^2 \rangle \tag{2.43}$$

Chapter 3

Apparatus and experiments

In this chapter, first the facility that was used to conduct the experiments is described. Next, the principles of the experimental measurement technique used in this study, particle image velocimetry (PIV), are briefly explained. We refer the interested readers to Adrian and Westerweel [2011], Raffel et al. [2018], and LaVision GmbH [2020] for the detailed discussions about various aspects of PIV. The last section of the chapter provides some details of the performed experiments.

3.1 The von Kármán swirling flow facility

The rig that was used for the experimental measurements is a large size von Kármán flow facility which is made of a dodecagonal Plexiglass tank with 2 m height and 2 m across filled with water. A schematic of the facility with the main dimensions is presented in figure 3.1. The top and bottom of the facility are fitted with two identical impellers with a diameter $D = 1.6$ m. The impellers have 8 straight vanes and are spaced $H = 1.25$ m away from each other in the vertical direction. This gives an aspect ratio of $D/H = 1.6/1.25 = 1.28$ for the facility. The impellers are driven by two stepper motors which transfer the rotational motion to the impellers through pulleys and gearboxes. The impellers can be driven and controlled independently at a speed within the range of 0.1 to 5 RPM. The main reason behind the physically large size of the facility is to reach high Reynolds numbers, $Re = R^2\Omega/\nu$, at relatively low flow velocities. This makes the Kolmogorov scales large and slow, since $\eta \sim \mathscr{L}_0 \, Re^{-3/4}$ in equation 2.20. As a result, it will be possible to perform state of the art volumetric measurements of turbulent structures at the dissipation scale as exemplified in Lawson and Dawson [2014, 2015] and Worth [2010]; Worth and Nickels [2011].

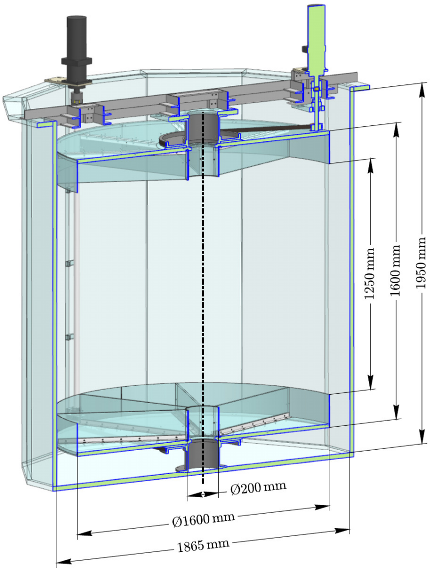

Figure 3.1: Schematic of the von Kármán swirling flow facility used in the present study.

In normal operation the two impellers counter rotate at a fixed angular velocity and a stationary von Kármán swirling flow is generated. The counter rotation creates rotational shear flow in cylindrical coordinates (toroidal shearing motion) acting in opposite directions, at the equatorial horizontal plane passing through the center point of the axis of rotation. The circumferential velocity magnitude, from the toroidal shearing, decreases when moving away from the impeller (forcing boundary), until it reaches almost zero in the horizontal equatorial plane where the two shear layers meet as shown in figure 3.2 by green. This rotational shear flow drives a centrifugal pumping force that leads to a secondary circulatory flow pattern in the vertical plane passing through the axis of rotation (poloidal circulating motion shown in figure 3.2 by red), where the flow is pulled away from the high pressure/ low velocity region close to the axis toward the low pressure/ high velocity region near the tip of the impeller. The mean flow pattern composed of the toroidal and poloidal motions are sketched in figure 3.2. In the region close to the geometrical center of the facility, the mean flow approaches zero and is dominated by velocity fluctuations. The turbulence generated in this region is homogeneous but not isotropic as the flow preserves some axisymmetric features from the large-scale forcing [Lawson and Dawson, 2014, 2015]. The facility was previously used in a number of studies to investigate the dynamics and kinematics of turbulence at the dissipation scale [Cardesa et al., 2013; Hunt et al., 2013; Lawson and Dawson, 2014, 2015; Worth, 2010; Worth and Nickels, 2011].

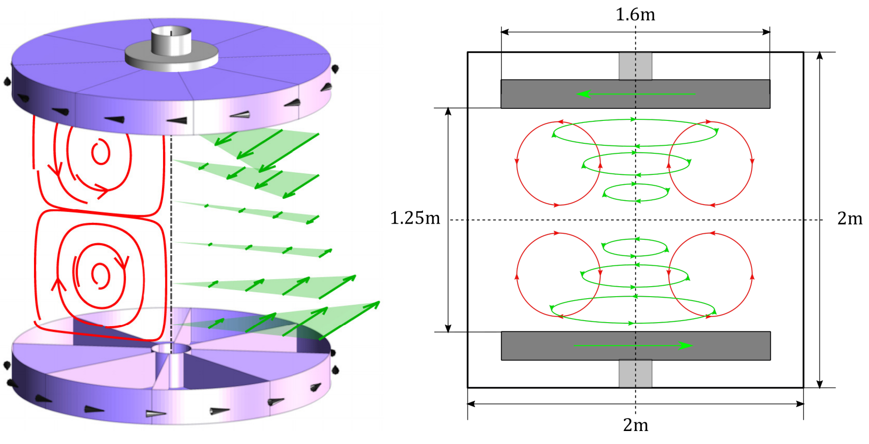

(a) (b)

Figure 3.2: Mean flow pattern of von Kármán swirling flow as a superposition of toroidal (green vectors) and poloidal (red streamlines) motions.

3.2 Particle Image Velocimetry (PIV)

Particle image velocimetry (PIV) is a non-intrusive optical measurement technique that has become a standard tool in experimental fluid mechanics to measure velocity fields and indirectly pressure field. In the recent years, due to the improvement and affordability of digital lasers and cameras, along with robust image processing algorithms, one can measure the velocity field in a plane or a volume of the flow.

The main idea of the technique is straightforward. A flow field is seeded with small neutrally buoyant particles that have a small Stokes number and can follow the flow field. A light source, usually a laser or LEDs, is focused into a sheet or volume of the flow. When the seeding particles scatter light, they make a clear contrast with the background fluid as exemplified in the images in figure 3.3.

For seeding particles with a diameter similar or larger than the wavelength of the incoming light source, this will be an elastic scattered light referred to as Mie scattering. The intensity of the scattered light in Mie scattering is proportional to the square diameter of the seeded particle. After taking consecutive images from the seeded flow, the velocity field can be calculated either by adopting a Lagrangian framework in which we track the particles over time, known as particle tracking velocimetry (PTV), or we can adopt an Eulerian framework, known as PIV. In PIV, a common technique is implementing cross-correlation between the consecutive images as shown in figures 3.4 and 3.5. The particle images are divided into smaller sub-areas known as interrogation windows. Each interrogation window in the first frame at time t is cross-correlated within the neighboring region in the

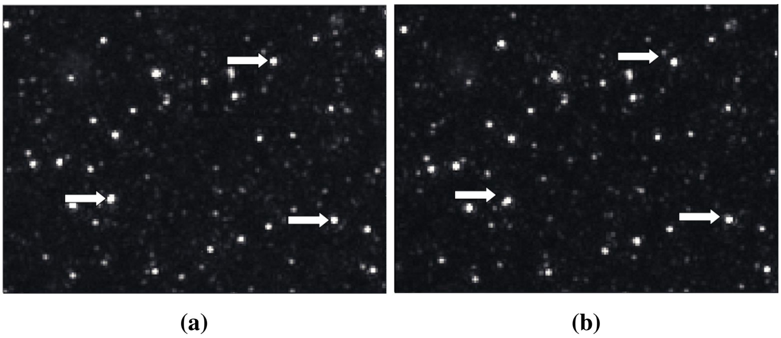
(a) (b)

Figure 3.3: Consecutive images of a flow seeded with particles scattering light. The particles move approximately 5 pixels in the horizontal direction between the two images. Source: LaVision GmbH [2017].

second frame at time $t + dt$. This will give a cross-correlation map for each interrogation window (figure 3.5). The position of the peak in the cross-correlation map indicates the distance that the particles in each interrogation window have moved between the times t and $t + dt$. The displacement distance is used to calculate the most probable velocity vector that represents the average velocity of the particle within each interrogation window. This procedure provides an Eulerian velocity field in the measurement domain at time t. More details and the related mathematical formulations can be found in Adrian and Westerweel [2011] and Raffel et al. [2018].

The PIV technique measures the velocity of the tracer particles as a surrogate for velocity field, making it important to ensure that the tracer particles follow the flow field as precisely as possible. To assess how well particles track the flow, a non-dimensional number known as the Stokes number is used and defined in equation 3.1 where τ_f is the characteristic time-scale of the flow field and τ_p is the tracer particle response time defined in equation 3.2. In this equation, L_f and U_f are the characteristic length and velocity of the flow, ρ_p is the density of particle, ρ_f is the flow density, μ_f is the dynamic viscosity of the flow, and d_p is the diameter of the particle.

$$Stk = \frac{\tau_p}{\tau_f} < 0.1 \tag{3.1}$$

$$\tau_p = \frac{(\rho_p - \rho_f)d_p^2}{18\mu_f}, \ \tau_f = \frac{L_f}{U_f} \Rightarrow Stk = \frac{(\rho_p - \rho_f)d_p^2 U_f}{18\mu_f L_f} \tag{3.2}$$

Equation 3.1 shows that the Stokes number needs to be near zero for the particle to

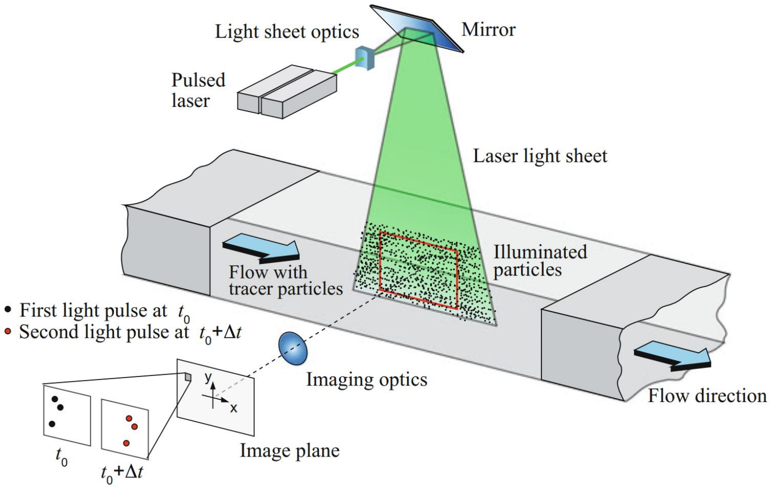

Figure 3.4: Example of the set-up and measurement procedure for 2C-2D PIV in a wind tunnel. Source: Raffel et al. [2018].

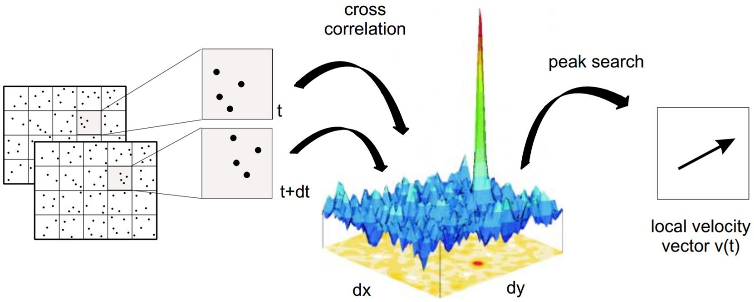

Figure 3.5: PIV cross correlation between the two frames of a double frame image to find the peak and consequently, the local velocity vector. Source: LaVision GmbH [2020].

follow the flow field most accurately. This requires the diameter of the particle to be as small as possible. On the other hand with reference to the earlier discussion about Mie scattering, very small particles are not practical in PIV as the intensity of the light scattered from the particle is proportionate to the square of its diameter (d_p^2) and very small particles will give poor signal to noise ratio. Thus, this works as an opposing requirement for the diameter of the particle and a trade off needs to be made. As a rule of thumb, $Stk < 0.1$ is considered sufficient [Tropea et al., 2007].

Pulsed lasers are commonly used in PIV measurements as the light source, because they act as a flash and one can collimate their beams. In low speed PIV (low acquisition frequency), high power double pulse lasers are used. Use of low speed PIV is common in turbulence research because statistics obtained over many large eddy turnover times are desirable for the convergence of turbulence statistics. These lasers provide two consecutive high energy pulses delayed by a very short time gap, dt. These pulses go through an arrangement of optics to make a thin laser sheet illuminating the particles field. The time delay between the two laser pulses is adjusted based on the flow velocity. On the one hand, the time delay should not be too large as the particles in the first image might be gone out of the field of view before the second image is taken, i.e. no or weak cross-correlation between the images will be obtained. On the other hand, very short time delay between the two images results in the particles almost not moving. This introduces a significant uncertainty in evaluation of the velocity fields. These maximum and minimum limits for the displacement of particles limits the dynamic range in PIV. A trade off needs to be made for the time delay to reach acceptable cross-correlation and uncertainty values.

Similar to most measurements techniques, a calibration process is necessary. The camera captures the position of the tracer particle on the digital sensor indicated by the pixel coordinate. Thus, it is necessary to establish a mapping function between pixel space and physical/real space of measurement. This is achieved by placing a calibration target with a known grid pattern in the field of view for the measurement, aligned with the light sheet. By taking images from the calibration target, a grid pattern is obtained in pixel space. The coordinates of the same grid pattern are known in both the real and pixel spaces and a mapping function can be fitted. Different options can be used as the calibration mapping function but the most common ones in PIV are the pinhole model and polynomials. The pinhole model is the simplest camera model that uses basic trigonometrical relations as the mapping function. However, the polynomial fit uses third or higher order polynomials to model the perspective and optical image distortions [LaVision GmbH, 2020]. Since the polynomial fit provides higher accuracy, it was used as the preferred

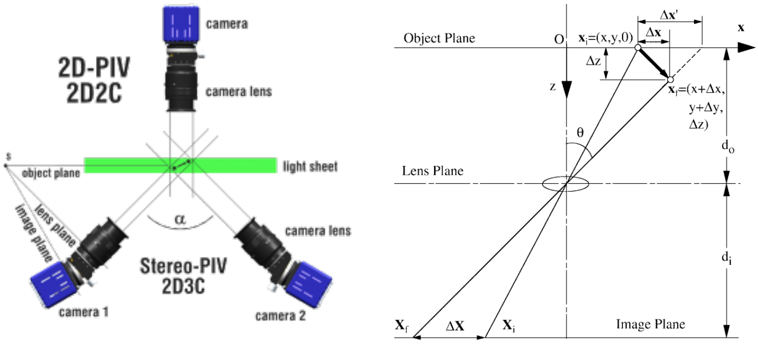

(a) (b)

Figure 3.6: 2D versus stereoscopic PIV; (a) 2D PIV only captures the projection of the velocity vector on the light sheet, which introduces significant perspective error when the flow is not parallel to the light sheet. However, stereoscopic PIV avoids perspective error by benefiting from two independent views and triangulation to measure all the three components of velocity. Source: LaVision GmbH [2020]. (b) Perspective error when an out of plane motion is captured by a single camera. Source: Prasad [2000].

method of calibration in the thesis.

Two-dimensional PIV can only capture the projection of the velocity vectors into the plane of the light sheet as shown in figure 3.6(a). If the flow is fully three dimensional, significant projection errors can be introduced as the particles move through the laser sheet. The resulting perspective error is shown in figure 3.6(b) and formulated in equation 3.3 [Prasad, 2000]. The error intensifies by the ratio between the out-of-plane to in-plane motion ($\Delta z/\Delta x$ and $\Delta z/\Delta y$) along with the projection of the off-axis angle (θ_x and θ_y). Therefore, to minimize the projection error in the 2D PIV measurement of a fully three dimensional flow, it is recommended to ensure a large viewing distance compared to the dimension of the field of view, i.e. using a long focal lens on the camera [Raffel et al., 2018].

$$PE = (PE_x, PE_y) = \left(\frac{\Delta x'}{\Delta x} - 1, \frac{\Delta y'}{\Delta y} - 1\right) = \left(\frac{\Delta z}{\Delta x}\tan\theta_x, \frac{\Delta z}{\Delta y}\tan\theta_y\right) \tag{3.3}$$

An effective way to address this problem is to use an extra camera. The two cameras look at the light sheet from different angles, known as stereoscopic PIV, enables the projection of the velocity vectors to be obtained in two planes as shown in figure 3.6(a). These projections and the angles of the cameras to the light sheet are then used to work out all three components of velocity through triangulation to obtain a 2D-3C velocity field. Since stereoscopic PIV is based on three dimen-

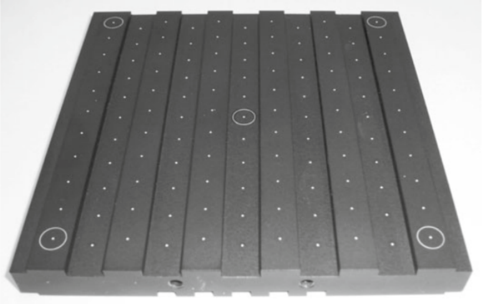

Figure 3.7: A two-level calibration target used in stereoscopic PIV. Here, the distance between the levels is 2 mm and the dots are located on a 10 mm grid. Source: Raffel et al. [2018].

sional triangulation, the calibration needs to be performed on at least two separate levels in space. This is usually achieved by using a two-level grid pattern as shown in figure 3.7.

Another advantage of using stereoscopic PIV is self-calibration. Self-calibration process maps the spatial position of the tracer particles in the images taken at the same time from the two cameras. A particle is expected to be reconstructed at the exact same position in space from the two cameras. However, error sources such as misalignment between the light sheet and the calibration target, that the mapping function is initially based on, lead to disparity. The self-calibration process uses the disparity to modify the mapping function and minimizes the calibration errors resulting form different sources to almost zero. These are shown in figures 3.8 and 3.9.

Like any other measurement technique, PIV is prone to errors and uncertainties. The uncertainty can result among others from particle image size, velocity gradients, interrogation window size, light intensity, and delay time in double-frame images. In order to minimize the uncertainty in the measurements of this study: (i) it was ensured to have particles moved in double-frame images at least 1/4 of the interrogation window size (32/4=8 pixels), (ii) the size of the particles in the images were approximately 2-3 pixels to avoid peak locking, (iii) the uncertainty maps calculated based on the method proposed by Wieneke [2015] in DaVis software were checked to ensure the minimum level of uncertainty in the measurements [LaVision GmbH, 2020], (iv) the peaks in the spatial correlation maps at different spots in the images were checked to ensure having a reasonable signal to noise ratio, and (v) self-calibration was used to minimize the uncertainty from calibration errors.

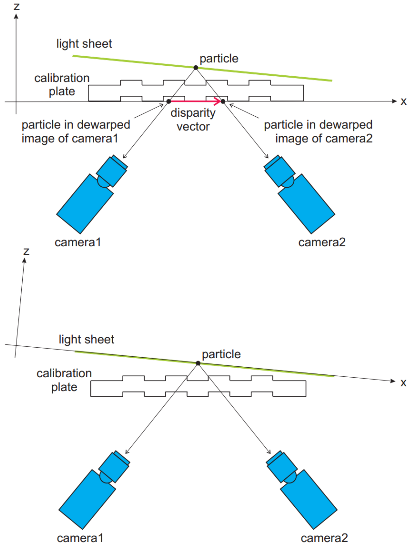

Figure 3.8: Self-calibration uses the disparity of the particle positions from the different camera images to rectify the mapping function. The goal is to minimize the calibration errors through minimizing the disparity. Here, self-calibration is used to rectify the misalignment between the calibration target and the light sheet. Source: LaVision GmbH [2020].

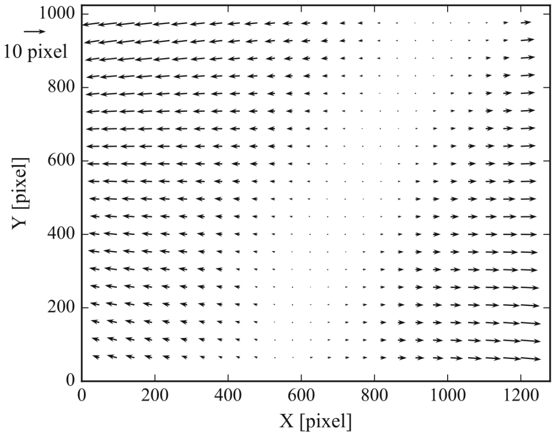

Figure 3.9: An example of the disparity field between the reconstructed positions of the particles from two cameras, because of a slight misalignment between the calibration target and the light sheet. Performing self-calibration minimizes the disparity. Source: Raffel et al. [2018].

3.3 Experiments

Three different experiments were performed in the facility: (i) characterization of the mean flow and its fluctuations, (ii) decay experiments, and (iii) forcing modulations experiments. The next sub-sections describe these measurements.

3.3.1 Mean flow characterization

The first experiment aimed at characterizing the mean flow in the facility both in the center and regions close to the boundaries (wall and impellers). Due to the large size of the facility and its dodecagonal geometry, simultaneous measurement of the field of view this large was not feasible. A composite/ stitched image of the measured mean flow inside the facility is shown in figure 3.10(a). The mean flow was produced by stitching the separate mean flows from smaller fields of view, 50cm×50cm, shown in figure 3.10(b). The mean flow clearly shows the toroidal and poloidal motions. The span of the measurement covered more than a quarter of the vertical plane passing through the center of the tank, i.e. $1.1R$ in the axial and $1.2R$ in the radial direction. The stationary flow was measured at 1, 2, and 3 RPM corresponding to $Re = R^2\Omega/\nu = 6 \times 10^4$, 1.2×10^5, and 1.8×10^5. Stereoscopic PIV with a forward-forward scattering configuration was used to perform the measurements.

To quantify the uncertainty in this measurement, the uncertainty of mean is evaluated [Benedict and Gould, 1996]. Figure 3.11 illustrates the histogram of uncertainty of axial mean velocity over the spatial points in a field of view of $50cm \times 50cm$ located at the center of the tank. The uncertainty at each point is normalized by the impeller tip velocity $\Delta V/R\Omega$. In total, $N = 3910$ snapshots with $407 \times 408 = 166056$ spatial points were used to calculate the histogram. The histogram has values whithin the range $3 \times 10^{-3} < \Delta V/R\Omega < 3.4 \times 10^{-3}$ where the peak is located at $\Delta V/R\Omega = 3.14 \times 10^{-3}$.

3.3.2 Decay experiments

Figure 3.12 illustrates the setup that was used to study freely decaying turbulence. In this study, after reaching the stationary flow condition, the counter-rotating impellers were stopped and the velocity field measurement was started immediately. A field of view (FoV) of 18cm×18cm was located at the geometrical center of the tank where the flow is homogeneous and has a negligible mean flow. The measurement continued until the flow came to rest. The measurement was repeated to ensure a reasonable convergence of turbulence statistics. The stationary flows of 2, 3, and 4 RPM corresponding to Reynolds numbers of $Re = R^2\Omega/\nu = 1.27 \times 10^5, 1.91 \times 10^5$, and 2.54×10^5 were used as initial conditions. These cases are referred to as 1, 2, and 3 in table 3.1. They correspond

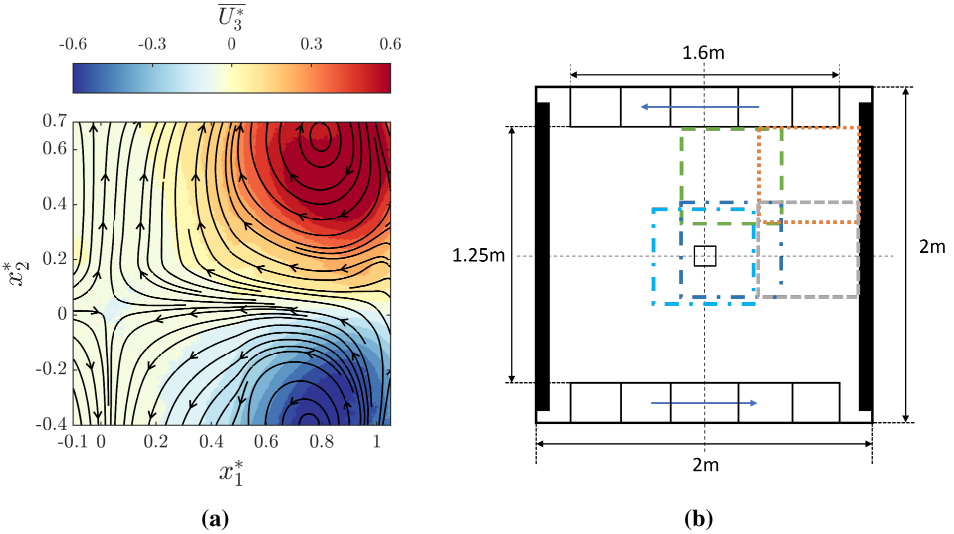

(a) **(b)**

Figure 3.10: (a) Mean velocity profile of the stationary flow at $Re = 1.21 \times 10^5$ measured in the facility using stereoscopic PIV . The filled color contour represents the out of plane (circumferential) velocity and the stream lines represent the radial and axial velocities. The spatial coordinates are normalized by the impeller radius R and the velocities are normalized by the impeller tip velocity $R\Omega$. (b) The mean velocity profile was generated by stitching the mean flows from four fields of view. The field of views are shown by colored squares and each covered $50cm \times 50cm$ inside the tank. The measurement was extended spatially in the radial and axial directions to cover more than the impeller radius in both directions.

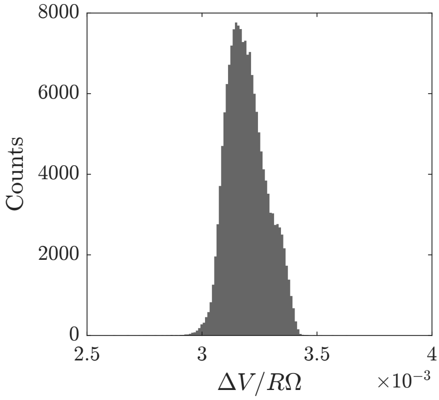

Figure 3.11: Histogram of uncertainty of axial mean velocity over the spatial points in a field of view of $50cm \times 50cm$ located at the center of the tank. The uncertainty at each point is normalized by the impeller tip velocity $\Delta V/R\Omega$.

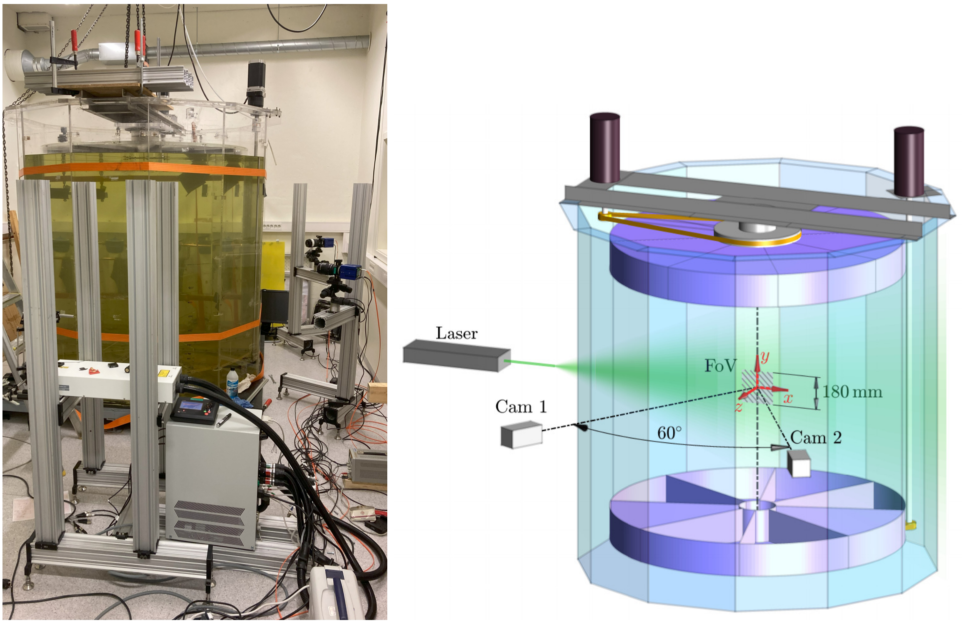

(a) **(b)**

Figure 3.12: The von Kármán swirling flow facility along with the stereoscopic PIV setup used in the study of turbulence decay; (a) image of the setup in the laboratory and (b) sketch of the measurement setup. The cameras and the laser sheet were arranged in a forward-backward scattering configuration.

to measurement duration of 10, 15, and 20 impeller revolutions, respectively (approximately 5 minutes). Each of the cases was repeated 30 times. In addition, another case of 4 RPM was measured 168 times, but with a shorter duration of 8.4 impeller revolutions (approximately 2.1 minutes). This case is referred to as 4 in table 3.1. In total, $3 \times 30 + 168 = 258$ runs of decay were measured. A special requirement for this measurement was adjusting the PIV double-frame time gap dt, as through the measurements the flow velocity decayed and the time gap needed to be increased continuously. We used a linear cumulative increase of dt, $dt^{n+1} = dt^n + \delta t$, where δt is a constant and the acquisition order is shown by the superscript n.

	Case 1	Case 2	Case 3	Case 4
Re	1.27×10^5	1.91×10^5	2.54×10^5	2.54×10^5
RPM	2	3	4	4
T_I (impeller revolution period) (s)	30	20	15	15
spatial resolution (mm)	2.67	2.67	2.67	2.67
PIV overlap	75%	75%	75%	75%
PIV interrogation window (pixel)	32×32	32×32	32×32	32×32
PIV double-frame (dt^1, δt) (ms)	(5, 0.15)	(3.5, 0.15)	(2, 0.15)	(2, 0.1)
number of samples per run	400	400	400	180
measurement duration normalized by T_I	10	15	20	8.4
total number of runs	30	30	30	168

Table 3.1: Measurement specifications in the decay study.

3.3.3 Forcing modulations experiments

Figure 3.13 depicts the measurement setup employed in the study of large-scale harmonic motions with and without forcing modulations. For these measurements, two sets of cameras were used (four cameras in total). One set of cameras were focused on a large field of view, while the other set were focused on a small field of view to perform simultaneous measurements with different spatial resolutions. In addition, a mirror was attached at the end side of the tank where the light sheet would leave the facility. Reflecting back the light sheet into the measurement field using this mirror helped increasing the intensity of the light sheet and improved the signal to noise ratio. In total, 13 cases were investigated consisting of four groups: sub-critical Reynolds number, supercritical Reynolds number (reference), harmonic modulations, and random modulations. Table 3.2 provides an overview of the measurements. Here, sub-critical and supercritical Reynolds numbers refer to Reynolds numbers lower and higher than the critical Reynolds number range $5 \times 10^4 < Re_C < 10^5$ proposed by Cortet et al. [2010] where the symmetry-breaking behavior in a von Kármán swirling flow is most significant. In the harmonic and random modulation cases, the duration of the measurements covered at least 1000 revolutions of the impellers. In the sub-critical Reynolds number case, the two impellers counter-rotated at 0.2 RPM ($f_L = 0.2/60 = 3.3 \times 10^{-3}\,Hz$ and $\Omega_L = 2\pi f_L$). In the reference case (supercritical Reynolds number), the two impellers counter-rotated at a constant speed of 2 RPM ($f_0 = 2/60 = 3.3 \times 10^{-2}\,Hz$ and $\Omega_0 = 2\pi f_0$). In the harmonic modulation cases, the rotational speed of the top and bottom impellers were set to equations 3.4 and 3.5, respectively. In these equations, the harmonic modulations are characterized by A_m as the amplitude, f_m as the frequency, and $\Delta\phi_m$ as the phase shift between impellers. These three were varied to generate different harmonic forcing cases. The base case was set to $(A_m, f_m/f_0, \Delta\phi_m) = (0.25, 0.1, \pi)$. The remaining harmonic cases were generated from the base case by changing a single variable: $A_m = (0.15, 0.25, 0.35)$, $f_m/f_0 = (0.05, 0.10, 0.15)$, and $\Delta\phi_m = (\pi/4, \pi/2, 3\pi/4, \pi)$.

In the random modulation cases, equation 3.6 (Langevin equation, see Pope [2000]) was used to determine the impeller velocity. In this equation, the parameters were set to $\sigma = 0.255$ (equal to the normalized rms of velocity fluctuations in the reference case), $T_1 = 300s$ (corresponding to $1/f_m$ of the base harmonic case), and $T_2 = 1s$ (which sets the rms value of the angular accelerations to $\simeq \sigma/\sqrt{T_1 T_2}$). $N(0,1)$ represents a random number generator function that followed the standard normal distribution with an average of 0 and a standard deviation of 1. Δt was the time step of modulation. Two random modulations were investigated: synchronized random where $\Omega_t(t) = -\Omega_b(t) = \Omega_r(t)$ and asynchronized random where the random generator ($N(0,1)$) in equation 3.6 generated independent values for the top and bottom impellers, i.e. $\Omega_t(t) \neq -\Omega_b(t)$.

$$\Omega_t(t) = \Omega_0 + \Omega_0 A_m \sin(2\pi f_m t + \Delta\phi_m) \tag{3.4}$$

$$\Omega_b(t) = -\Omega_0 + \Omega_0 A_m \sin(2\pi f_m t) \tag{3.5}$$

$$\begin{aligned} \Omega_r(t) &= \Omega_0 + (\Omega_r(t-\Delta t) - \Omega_0)(1 - \frac{\Delta t}{T_1}) + \frac{\sigma\zeta(t)\Delta t}{\sqrt{T_1 T_2}}\sqrt{1 - e^{-2\frac{\Delta t}{T_2}}} \\ \zeta(t) &= \zeta(t-\Delta t)e^{-\frac{\Delta t}{T_2}} + N(0,1) \end{aligned} \tag{3.6}$$

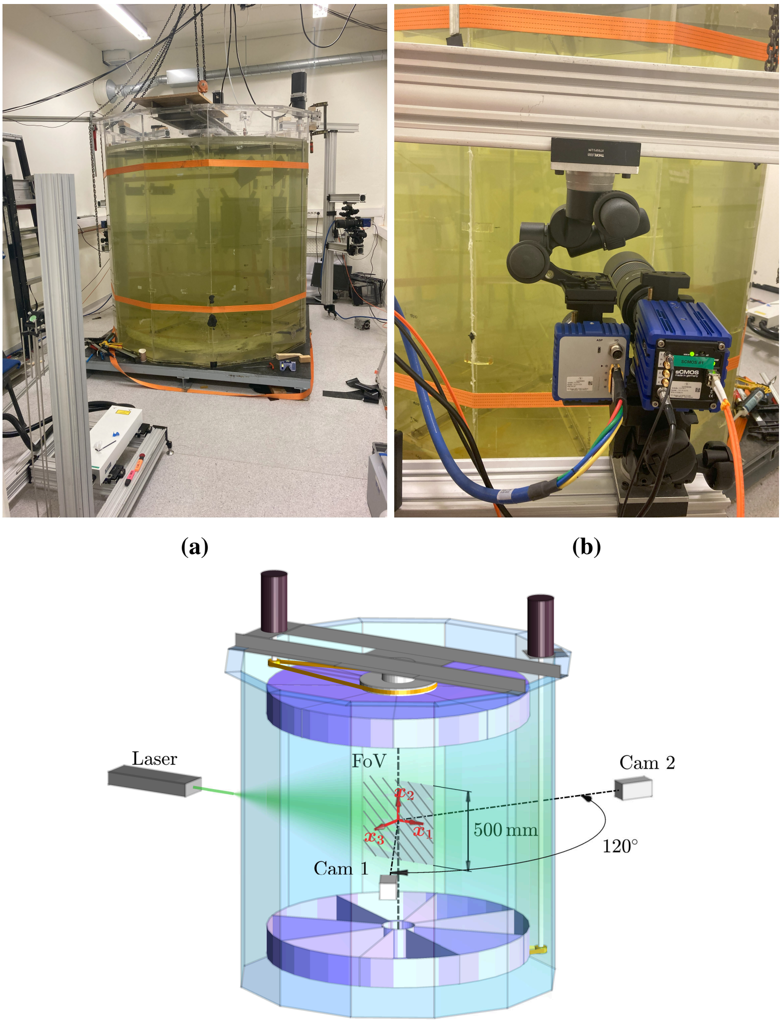
(a)

(b)

(c)

Figure 3.13: The von Kármán swirling flow facility along with the stereoscopic PIV setup used in the study of large-scale harmonic motions; (a) image of the setup in the laboratory, (b) two sets of cameras, four in total, were used to perform simultaneous measurements with different spatial resolutions, and (c) sketch of the measurement setup. The cameras and the laser sheet were arranged in a forward-forward scattering configuration.

Case number	Re	Harmonic (3.4-3.5) A_m	f_m/f_0	$\Delta\phi_m/\pi$	Random (3.6)	Counter-rotation
1 (sub-critical)	1.21×10^4	-	-	-	-	√
2 (reference)	1.21×10^5	-	-	-	-	√
3	1.21×10^5	0.25	0.05	0	-	×
4	1.21×10^5	0.25	0.05	1	-	√
5	1.21×10^5	0.25	0.1	0.25	-	×
6	1.21×10^5	0.25	0.1	0.5	-	×
7	1.21×10^5	0.25	0.1	0.75	-	×
8	1.21×10^5	0.15	0.1	1	-	√
9	1.21×10^5	0.25	0.1	1	-	√
10	1.21×10^5	0.35	0.1	1	-	√
11	1.21×10^5	0.25	0.15	1	-	√
12 (synchronized random)	1.21×10^5	-	-	-	√	√
13 (asynchronized random)	1.21×10^5	-	-	-	√	√

Table 3.2: An overview of the measured cases in the study of large-scale harmonic motions.

Chapter 4

Summary of the research articles

4.1 Brief concluding remarks

In this thesis, dynamics of turbulence were studied both at the small and large scales in a von Kármán swirling flow.

In the study of the small-scales in *Article 1*, an experimental data set of volumetric scanning PIV at the center of a von Kármán swirling flow [Lawson and Dawson, 2014, 2015] along with a DNS data set of homogeneous isotropic turbulence [Li et al., 2008] were analyzed. This was the first successful implementation of a recent objective definition of vortex structures proposed by Haller et al. [2016] that resulted in 3D vortices at the dissipation scale of turbulence in experimental data. Our analysis showed that even though small-scale vortex structures are not active in overall dynamics of turbulence due to the lack of self-amplification [Jiménez et al., 1993; Tsinober, 2009], they are important in another aspect, i.e. interaction with the surrounding background fluid through exchange of mass, momentum, and enstrophy.

Next, in *Article 2* our measurements of freely decaying turbulence in a von Kármán swirling flow at high Reynolds number showed that TKE decayed faster than the well known theoretical predictions of Loitsiansky [1939] and Saffman [1967]. However, after decomposing TKE into the contributions from different velocity components, it was observed that the velocity field followed the Loitsyansky decay in the axial direction of the flow whereas other components, radial and circumferential, were in the saturation/confinement regime.

Finally, in *Article 3* measurements were conducted to investigate a large-scale energetic and slowly rotating structure in von Kármán flows previously reported by

Baj et al. [2019]. The results showed that the structure only appeares below the critical Reynolds number suggested by Cortet et al. [2010]. In addition, the structure emerges at a Reynolds number higher than the critical value by applying a harmonic forcing modulation that imposes a harmonic phase shift between the two impellers. This structure is expected to affect the mixing property of the flow at the large-scale along with a fingerprint through various scales of motion.

4.2 Summary of articles

The rest of this chapter summarizes the three research articles that are attached in their full lengths to the end of this thesis.

Article 1:

Entrainment, detrainment and enstrophy transport by small-scale vortex structures
Farid Aligolzadeh, Markus Holzner, and James R. Dawson
Published in Journal of Fluid Mechanics

In *Article 1*, we investigated features of small-scale vortices in both experimental and DNS data to show consistency between the results. In the experimental data set, three dimensional three components (3D-3C) velocity field was produced from scanning PIV measurements at the center of a von Kármán swirling flow facility with a spatial resolution of 1η where $R_\lambda = 179$ [Lawson and Dawson, 2014, 2015]. The DNS data set was forced isotropic turbulence of $R_\lambda = 418$ with a spatial resolution of 2.2η, from Johns Hopkins turbulence database [Li et al., 2008].

To detect the vortex structures, we implemented the definition of Objective Eulerian Coherent Structures (OECSs) proposed by Haller et al. [2016]. The main advantages of this method are (i) avoiding thresholding (arbitrariness in defining the vortex boundary) and (ii) being observer independent. The analysis was performed on 1003 available volumetric snapshots of the experimental data set where 12500 vortices were detected in total, along with 9274 vortices identified in 50 snapshots of the DNS data set. The average radius of the vortices was equal to 5.1η occupying 1.4% of the volume of the flow, in agreement with the available studies [da Silva et al., 2011; Ganapathisubramani et al., 2008; Ghira et al., 2022; Jiménez and Wray, 1998; Jiménez et al., 1993].

To gain an insight into the distinctions between the vortices and the flow field as a whole, we provided statistics conditioned on the vortices versus the whole volume of the flow. The p.d.f.s and joint p.d.f. of enstrophy and dissipation showed that the vortices were intense realizations of enstrophy covered by the regions of high straining (dissipation). In addition, enstrophy and dissipation scale together inside the vortices. The p.d.f.s of the alignment between the vorticity vector and eigenvectors of the rate of strain tensor were calculated, as this alignment is important in the phenomena of vortex stretching and compression. The results indicated that the vorticity vector had a strong preference to be aligned with the intermediate eigenvector while orienting normal to the extensive and compressive eigenvectors. This was different from the volume of the flow where the vorticity vector showed a tendency to orient normal to the compressive eigenvector, align with the intermediate eigenvector, and neutral to the extensive eigenvector.

To investigate the interaction between the detected vortex structures and the surrounding fluid (background flow), all the terms in the enstrophy transport and entrainment velocity equations were calculated on the radial and axial directions of the vortices. The p.d.f. of the radial entrainment/ detrainment velocity at the boundary of the vortices was slightly skewed in favor of entrainment. Overall, the entrainment p.d.f. at the boundary was very similar to TNTI in free shear flows such as jets and mixing layers. Contour of the average entrainment velocity in the radial and axial directions showed that the entrainment velocity was maximum at the center of the vortex, while decaying when marching out in the radial and axial directions. From this picture and the flow being statistically stationary, i.e. vortices do not grow in size over time, it was conjectured that the net average entrainment in the radial direction at the boundary was balanced by a net average detrainment at the two axial ends of the vortices.

It was shown that the entrainment was highly correlated with the inviscid phenomenon of vortex stretching (enstrophy production), whereas the detrainment was highly correlated with the viscous phenomena of enstrophy diffusion and dissipation. This behavior was in contrast with TNTI where entrainment and detrainment are only controlled by the viscous phenomena due to the presence of viscous/laminar superlayer. However, our result resembled turbulent-turbulent interface (TTI) where vortex stretching plays a significant role in local entrainment.

A comparison was made between the detected vortices and Burgers' vortex model. The p.d.f.s of the radii from the structures and Burgers' vortices showed a good agreement, but it was found that Burgers' vortex model overestimated the radial enstrophy decay compared to detected structures. The average enstrophy transport equation conditioned on the radial direction of the vortices and Burgers' vortex model showed a consistent competition between the vortex stretching and the viscous diffusion and dissipation. However, Burgers' vortex model was not able to predict the enstrophy transport/ entrainment behavior observed in the axial direction of the detected vortex structures.

Article 2:

Experiments of turbulent decay in a von Kármán swirling flow at high Reynolds number

Farid Aligolzadeh, Pawel Baj, and James R. Dawson
Under consideration for publication in Journal of Fluid Mechanics

In *Article 2*, we reported the results of our measurements at the center of a high Reynolds number von Kármán swirling flow after the impellers were stopped. This study belongs to a category in turbulence referred to as freely decaying turbulence that has been extensively studied both numerically in HIT boxes and experimentally, mostly in grid turbulence. However to the best knowledge of the authors, freely decaying turbulence has not been studied experimentally or numerically in a von Kármán swirling flow, even though this flow has served a canonical role in studies of turbulence over the past few decades. As discussed in §2.6, study of the decay provides useful information about the dynamics of the large-scales in the stationary turbulence, because the stationary flow is the initial condition for the decay after removing the energy injection into the system.

In this study, we investigated three Reynolds numbers, $Re = R^2\Omega/\nu = 1.27 \times 10^5$, 1.91×10^5, and 2.54×10^5. After stopping the impellers, we monitored the evolution of the velocity field in time by using stereoscopic PIV. The measurement lasted 10-20 impeller rotation periods, depending on the case. We repeated the identical measurements many times to ensure a reasonable convergence of turbulence statistics. In total, 258 runs of turbulent decay were measured.

The results showed that the decay of TKE consisted of two parts. An initial transition period where TKE remained almost constant over 2.58 impeller rotation periods, as a result of the inertia of the stationary flow, followed by a classical power-law decay with an exponent of $n = -1.62$, i.e. $k(t) \sim t^{-1.62}$. The decay process was further investigated by evaluating the contributions to TKE from different velocity components. The velocity components in the radial and circumferential directions showed a decay exponent of $n = -1.99$, wheras the exponent was $n = -1.38$ in the axial direction. These exponents suggested the saturation/confinement effect in the radial and circumferential directions and the Loitsyansky decay in the axial direction. This was further explored by evaluating the evolution of longitudinal integral length-scales in the axial and radial direction, which showed a power-law increase in the axial direction with an exponent close to $2/7$ (Loitsyansky prediction), whereas the length-scale did not grow in the radial direction (saturation/confinement). Overall, this study found the Loitsyansky decay pattern in the axial direction of the flow, but the saturation regimes in other directions.

Article 3:

Experimental investigation of large-scale harmonic motions in a von Kármán swirling flow

Farid Aligolzadeh, Pawel Baj, and James R. Dawson

Under consideration for publication in Journal of Fluid Mechanics

In *Article 3*, the large-scales of a high Reynolds number von Kármán swirling flow were studied. Even though most studies in von Kármán swirling flows are focused on the structures and dynamics of turbulence at the dissipation scales, close to the stagnation point of the flow, some interesting phenomena have been observed at the large-scales, e.g. symmetry breaking behavior [de la Torre and Burguete, 2007] and presence of an energetic and large structure that rotates slowly around the flow axis [Baj et al., 2019]. This study was motivated by the findings of Baj et al. [2019] about the rotating structure observed at $Re = 3 \times 10^4$. The aim of this study was to investigate the effects of the Reynolds number below and beyond the critical range, i.e. $5 \times 10^4 < Re_c < 10^5$ suggested by Cortet et al. [2010], and forcing modulations on the appearance or suppression of the instability. Experimental measurements were performed using stereoscopic PIV in a $50cm \times 50cm$ field of view at the center of a large von Kármán flow facility.

In the below critical Reynolds number case without forcing modulation $Re = 1.2 \times 10^4$, we observed an oval-shape, large energetic structure similar to the structure reported in Baj et al. [2019]. However, our detected structure showed a different oscillation frequency $f/f_0 \approx 2$, f_0 is the impeller frequency, whereas it was reported to be $f/f_0 \approx 0.1$ in Baj et al. [2019]. In addition, our structure showed oscillations in all directions of the flow, i.e. radial, circumferential, and axial, whereas Baj et al. [2019] reported the oscillations only in the radial and circumferential directions. Our conjecture was that the observed discrepancies were because of the geometrical differences between the two facilities in which the experiments were conducted. This is aligned with the large-scales of turbulence being sensitive to the features of the apparatus, boundary conditions, intrinsic instabilities, etc.

Next, the Reynolds number was increased beyond the critical range to $Re = 1.2 \times 10^5$, labeled as the reference case. However, the large-scale harmonic structure did not appear in this case. We applied modulations to the impellers in the reference case to identify whether the instability emerges as a result. We investigated a broad range of parameters space $(A_m, f_m, \Delta\phi_m)$ in harmonic forcing modulations in forms of $\Omega_t(t) = \Omega_0(1 + A_m \sin(2\pi f_m t + \Delta\phi_m))$ for the top impeller and $\Omega_b(t) = \Omega_0(-1 + A_m \sin(2\pi f_m t))$ for the bottom impeller, in addition to two random modulations (Langevin forcing with and without phase shift between the impellers). In the harmonic cases, a parameter space of $A_m = (0.15, 0.25, 0.35)$, $f_m/f_0 = (0.05, 0.1, 0.15)$, and $\Delta\phi_m = (\pi/4, \pi/2, 3\pi/4, \pi)$ was assessed.

The results showed that only when a harmonic phase shift ($\Delta\phi_m \neq \pi$) existed between the two impellers, the harmonic motion in the flow was activated. When $\Delta\phi_m = 3\pi/4$, a large-scale oscillation in the axial direction of the flow was observed at the modulation frequency $f_m/f_0 = 0.1$. On the other hand, the oscillation appeared in both the axial and circumferential directions of the flow when $\Delta\phi_m = \pi/2$ and $\pi/4$. Further analysis showed that this large-scale structure was an energetic oval-shape flow pattern that accounted for approximately 40% of the kinetic energy of the flow oscillating along the axial and circumferential directions, locked to the modulation frequency. Changing the other two parameters, A_m and f_m, did not activate the harmonic motion when there was no harmonic phase shift between the impellers. In addition, the random modulation forcing both with and without phase shift did not activate a harmonic flow pattern. In the harmonic modulation cases with a significant phase shift between the impellers, $\Delta\phi_m = \pi/2$ and $\pi/4$, the oscillation in the axial direction was more pronounced than the circumferential direction. Investigation of the cross-correlations between the forcing and velocity field showed a phase delay of approximately 0.2π between the oscillations in the axial and circumferential directions.

Bibliography

RJ Adrian. Hairpin vortex organization in wall turbulence. *Physics of Fluids*, 19 (4), 2007.

RJ Adrian and J Westerweel. *Particle image velocimetry*. Cambridge University Press, 2011.

F Aligolzadeh, M Holzner, and JR Dawson. Entrainment, detrainment and enstrophy transport by small-scale vortex structures. *Journal of Fluid Mechanics*, 973:A5, 2023.

S Angriman, PD Mininni, and PJ Cobelli. Velocity and acceleration statistics in particle-laden turbulent swirling flows. *Physical Review Fluids*, 5(6):064605, 2020.

M Asadi, M Kamruzzaman, and RJ Hearst. The effect of inlet turbulence on the quiescent core of turbulent channel flow. *Journal of Fluid Mechanics*, 935:A37, 2022.

WT Ashurst, AR Kerstein, RM Kerr, and CH Gibson. Alignment of vorticity and scalar gradient with strain rate in simulated Navier–Stokes turbulence. *Physics of Fluids*, 30(8):2343–2353, 1987.

P Baj, JR Dawson, NA Worth, AN Knutsen, JM Lawson, and E Bodenschatz. Very large-scale motions in von Kármán flow. In *Proceedings of the 11th International Symposium on Turbulence and Shear Flow Phenomena (TSFP-11)*, 2019.

G Balamurugan, A Rodda, J Philip, and AC Mandal. Characteristics of the turbulent non-turbulent interface in a spatially evolving turbulent mixing layer. *Journal of Fluid Mechanics*, 894:A4, 2020.

GK Batchelor. The theory of axisymmetric turbulence. *Proceedings of the Royal Society of London. Series A. Mathematical and Physical Sciences*, 186(1007): 480–502, 1946.

GK Batchelor. Note on a class of solutions of the Navier-Stokes equations representing steady rotationally-symmetric flow. *Quarterly Journal of Mechanics and Applied Mathematics*, 4(1):29–41, 1951.

GK Batchelor and I Proudman. The large-scale structure of homogenous turbulence. *Philosophical Transactions of the Royal Society of London. Series A, Mathematical and Physical Sciences*, 248(949):369–405, 1956.

GK Batchelor and AA Townsend. Decay of isotropic turbulence in the initial period. *Proceedings of the Royal Society of London. Series A. Mathematical and Physical Sciences*, 193(1035):539–558, 1948.

GK Batchelor and AA Townsend. The nature of turbulent motion at large wavenumbers. *Proceedings of the Royal Society of London. Series A. Mathematical and Physical Sciences*, 199(1057):238–255, 1949.

F Belin, J Maurer, P Tabeling, and H Willaime. Observation of intense filaments in fully developed turbulence. *Journal de Physique II*, 6(4):573–583, 1996.

LH Benedict and RD Gould. Towards better uncertainty estimates for turbulence statistics. *Experiments in Fluids*, 22(2):129–136, 1996.

H Berning and T Rösgen. Suppression of large-scale azimuthal modulations in a von Kármán flow using random forcing. *Physics of Fluids*, 35(7), 2023.

H Berning, T Grünberg, and T Rösgen. Suppression of large scale structures in a turbulent von Kármán flow using random forcing. In *Proceedings of the 10th International Symposium on Turbulence and Shear Flow Phenomena (TSFP-10)*, 2017.

R Betchov. An inequality concerning the production of vorticity in isotropic turbulence. *Journal of Fluid Mechanics*, 1(5):497–504, 1956.

D Bonn, Y Couder, PHJ Van Dam, and S Douady. From small scales to large scales in three-dimensional turbulence: The effect of diluted polymers. *Physical Review E*, 47(1):R28, 1993.

E Brown and G Ahlers. The origin of oscillations of the large-scale circulation of turbulent Rayleigh–Bénard convection. *Journal of Fluid Mechanics*, 638: 383–400, 2009.

GL Brown and A Roshko. On density effects and large structure in turbulent mixing layers. *Journal of Fluid Mechanics*, 64(4):775–816, 1974.

RD Brown, Z Warhaft, and GA Voth. Acceleration statistics of neutrally buoyant spherical particles in intense turbulence. *Physical Review Letters*, 103:194501, 2009.

SL Brunton and JN Kutz. *Data-driven science and engineering: Machine learning, dynamical systems, and control.* Cambridge University Press, 2022.

D Buaria, E Bodenschatz, and A Pumir. Vortex stretching and enstrophy production in high Reynolds number turbulence. *Physical Review Fluids*, 5(10), 2020.

ORH Buxton and B Ganapathisubramani. Amplification of enstrophy in the far field of an axisymmetric turbulent jet. *Journal of Fluid Mechanics*, 651:483–502, 2010.

O Cadot, S Douady, and Y Couder. Characterization of the low-pressure filaments in a three-dimensional turbulent shear flow. *Physics of Fluids*, 7(3):630–646, 1995.

O Cadot, JH Titon, and D Bonn. Experimental observation of resonances in modulated turbulence. *Journal of Fluid Mechanics*, 485:161–170, 2003.

BJ Cantwell. Organized motion in turbulent flow. *Annual Review of Fluid Mechanics*, 13(1):457–515, 1981.

JI Cardesa, D Mistry, L Gan, and JR Dawson. Invariants of the reduced velocity gradient tensor in turbulent flows. *Journal of Fluid Mechanics*, 716:597–615, 2013.

P Chainais, P Abry, and J-F Pinton. Intermittency and coherent structures in a swirling flow: A wavelet analysis of joint pressure and velocity measurements. *Physics of Fluids*, 11(11):3524–3539, 1999.

A Cheminet, D Geneste, A Barlet, Y Ostovan, T Chaabo, V Valori, P Debue, C Cuvier, F Daviaud, J-M Foucaut, JP Laval, V Padilla, C Wiertel-Gasquet, and B Dubrulle. Eulerian vs Lagrangian irreversibility in an experimental turbulent swirling flow. *Physical Review Letters*, 129(12):124501, 2022.

G Comte-Bellot and S Corrsin. The use of a contraction to improve the isotropy of grid-generated turbulence. *Journal of Fluid Mechanics*, 25(4):657–682, 1966.

S Corrsin and AL Kistler. Free-stream boundaries of turbulent flows. Technical report, 1955.

P-P Cortet, A Chiffaudel, F Daviaud, and B Dubrulle. Experimental evidence of a phase transition in a closed turbulent flow. *Physical Review Letters*, 105(21): 214501, 2010.

C B. da Silva, RJN dos Reis, and JCF Pereira. The intense vorticity structures near the turbulent/non-turbulent interface in a jet. *Journal of Fluid Mechanics*, 685: 165–190, 2011.

PA Davidson. *Turbulence: an introduction for scientists and engineers*. Oxford University Press, 2015.

J De Jong, L Cao, SH Woodward, JPLC Salazar, LR Collins, and H Meng. Dissipation rate estimation from PIV in zero-mean isotropic turbulence. *Experiments in Fluids*, 46:499–515, 2009.

A de la Torre and J Burguete. Slow dynamics in a turbulent von Kármán swirling flow. *Physical Review Letters*, 99(5):054101, 2007.

CM de Silva, N Hutchins, and I Marusic. Uniform momentum zones in turbulent boundary layers. *Journal of Fluid Mechanics*, 786:309–331, 2016.

P Debue, V Valori, C Cuvier, F Daviaud, JM Foucaut, JP Laval, C Wiertel, V Padilla, and B Dubrulle. Three-dimensional analysis of precursors to non-viscous dissipation in an experimental turbulent flow. *Journal of Fluid Mechanics*, 914: A9, 2021.

S Douady, Y Couder, and ME Brachet. Direct observation of the intermittency of intense vorticity filaments in turbulence. *Physical Review Letters*, 67(8):983, 1991.

Z Doulgerakis, M Yianneskis, and A Ducci. On the manifestation and nature of macroinstabilities in stirred vessels. *AIChE Journal*, 57(11):2941–2954, 2011.

GE Elsinga and I Marusic. Universal aspects of small-scale motions in turbulence. *Journal of Fluid Mechanics*, 662:514–539, 2010.

LB Esteban, JS Shrimpton, and B Ganapathisubramani. Laboratory experiments on the temporal decay of homogeneous anisotropic turbulence. *Journal of Fluid Mechanics*, 862:99–127, 2019.

H Faller, D Geneste, T Chaabo, A Cheminet, V Valori, Y Ostovan, L Cappanera, C Cuvier, F Daviaud, JM Foucaut, JL Guermond, JP Laval, C Nore, V Padilla, C Wiertel, and B Dubrulle. On the nature of intermittency in a turbulent von Kármán flow. *Journal of Fluid Mechanics*, 914:A2, 2021.

S Fauve, C Laroche, and B Castaing. Pressure fluctuations in swirling turbulent flows. *Journal de physique II*, 3(3):271–278, 1993.

RP Feynman, RB Leighton, and M Sands. *The Feynman lectures on physics, Vol. I: The new millennium edition: mainly mechanics, radiation, and heat*, volume 1. Basic books, 2011.

U Frisch. *Turbulence: the legacy of AN Kolmogorov*. Cambridge University Press, 1995.

D Funfschilling and G Ahlers. Plume motion and large-scale circulation in a cylindrical Rayleigh-Bénard cell. *Physical Review Letters*, 92(19):194502, 2004.

B Ganapathisubramani, K Lakshminarasimhan, and NT Clemens. Investigation of three-dimensional structure of fine scales in a turbulent jet by using cinematographic stereoscopic particle image velocimetry. *Journal of Fluid Mechanics*, 598:141–175, 2008.

WK George and H Wang. The exponential decay of homogeneous turbulence. *Physics of Fluids*, 21(2), 2009.

AA Ghira, GE Elsinga, and CB Da Silva. Characteristics of the intense vorticity structures in isotropic turbulence at high Reynolds numbers. *Physical Review Fluids*, 7(10):104605, 2022.

S Grossmann, D Lohse, and C Sun. High-Reynolds number Taylor-Couette turbulence. *Annual Review of Fluid Mechanics*, 48:53–80, 2016.

G Haller, A Hadjighasem, M Farazmand, and F Huhn. Defining coherent vortices objectively from the vorticity. *Journal of Fluid Mechanics*, 795:136–173, 2016.

RJ Hearst and P Lavoie. Decay of turbulence generated by a square-fractal-element grid. *Journal of Fluid Mechanics*, 741:567–584, 2014.

LHO Hellström, B Ganapathisubramani, and AJ Smits. The evolution of large-scale motions in turbulent pipe flow. *Journal of Fluid Mechanics*, 779:701–715, 2015.

LHO Hellström, I Marusic, and AJ Smits. Self-similarity of the large-scale motions in turbulent pipe flow. *Journal of Fluid Mechanics*, 792:R1, 2016.

M Holzner and B Lüthi. Laminar superlayer at the turbulence boundary. *Physical Review Letters*, 106(13):134503, 2011.

PD Huck, N Machicoane, and R Volk. Production and dissipation of turbulent fluctuations close to a stagnation point. *Physical Review Fluids*, 2(8), 2017.

SG Huisman, DPM Van Gils, S Grossmann, C Sun, and D Lohse. Ultimate turbulent taylor-couette flow. *Physical Review Letters*, 108(2):024501, 2012.

JCR Hunt, T Ishihara, NA Worth, and Y Kaneda. Thin shear layer structures in high Reynolds number turbulence. *Flow, Turbulence and Combustion*, 92(3): 607–649, 2013.

D Hurst and JC Vassilicos. Scalings and decay of fractal-generated turbulence. *Physics of Fluids*, 19(3), 2007.

J Hwang, J Lee, HJ Sung, and TA Zaki. Inner–outer interactions of large-scale structures in turbulent channel flow. *Journal of Fluid Mechanics*, 790:128–157, 2016.

J Jiménez and AA Wray. On the characteristics of vortex filaments in isotropic turbulence. *Journal of Fluid Mechanics*, 373:255–285, 1998.

J Jiménez, AA Wray, PG Saffman, and RS Rogallo. The structure of intense vorticity in isotropic turbulence. *Journal of Fluid Mechanics*, 255:65–90, 1993.

KS Kankanwadi and ORH Buxton. On the physical nature of the turbulent/turbulent interface. *Journal of Fluid Mechanics*, 942:A31, 2022.

RM Kerr. Higher-order derivative correlations and the alignment of small-scale structures in isotropic numerical turbulence. *Journal of Fluid Mechanics*, 153: 31–58, 1985.

KC Kim and RJ Adrian. Very large-scale motion in the outer layer. *Physics of Fluids*, 11(2):417–422, 1999.

AN Knutsen, P Baj, JM Lawson, E Bodenschatz, JR Dawson, and NA Worth. The inter-scale energy budget in a von Kármán mixing flow. *Journal of Fluid Mechanics*, 895:A11, 2020.

AN Kolmogorov. On degeneration (decay) of isotropic turbulence in an incompressible viscous liquid. In *Dokl. Akad. Nauk SSSR*, volume 31, pages 538–540, 1941a.

AN Kolmogorov. The local structure of turbulence in incompressible viscous fluid for very large Reynolds numbers. In *Dokl. Akad. Nauk SSSR*, volume 30, pages 301–305, 1941b.

S Kreuzahler, D Schulz, H Homann, Y Ponty, and R Grauer. Numerical study of impeller-driven von Kármán flows via a volume penalization method. *New Journal of Physics*, 16(10):103001, 2014.

PÅ Krogstad and PA Davidson. Is grid turbulence Saffman turbulence? *Journal of Fluid Mechanics*, 642:373–394, 2009.

PÅ Krogstad and PA Davidson. Freely decaying, homogeneous turbulence generated by multi-scale grids. *Journal of Fluid Mechanics*, 680:417–434, 2011.

YS Kwon, J Philip, CM de Silva, N Hutchins, and JP Monty. The quiescent core of turbulent channel flow. *Journal of Fluid Mechanics*, 751:228–254, 2014.

A La Porta, GA Voth, F Moisy, and E Bodenschatz. Using cavitation to measure statistics of low-pressure events in large-Reynolds-number turbulence. *Physics of Fluids*, 12(6):1485–1496, 2000.

A La Porta, GA Voth, AM Crawford, J Alexander, and E Bodenschatz. Fluid particle accelerations in fully developed turbulence. *Nature*, 409(6823):1017–1019, 2001.

LD Landau and EM Lifshitz. *Fluid Mechanics*. Pergamon Press, London, 1959.

LaVision GmbH. *Flowmaster: product manual for Davis 8.4*. Göttingen, Germany, 2017.

LaVision GmbH. *Flowmaster: product manual for Davis 10.1*. Göttingen, Germany, 2020.

JM Lawson and JR Dawson. A scanning PIV method for fine-scale turbulence measurements. *Experiments in Fluids*, 55(12), 2014.

JM Lawson and JR Dawson. On velocity gradient dynamics and turbulent structure. *Journal of Fluid Mechanics*, 780:60–98, 2015.

JM Lawson, E Bodenschatz, AN Knutsen, JR Dawson, and NA Worth. Direct assessment of Kolmogorov's first refined similarity hypothesis. *Physical Review Fluids*, 4(2):022601, 2019.

J Lee, JH Lee, J Choi, and HJ Sung. Spatial organization of large-and very-large-scale motions in a turbulent channel flow. *Journal of Fluid Mechanics*, 749: 818–840, 2014.

J Lee, HJ Sung, and TA Zaki. Signature of large-scale motions on turbulent/non-turbulent interface in boundary layers. *Journal of Fluid Mechanics*, 819:165–187, 2017.

JH Lee. Large-scale motions in turbulent boundary layers subjected to adverse pressure gradients. *Journal of Fluid Mechanics*, 810:323–361, 2017.

Y Li, E Perlman, M Wan, Y Yang, C Meneveau, R Burns, S Chen, A Szalay, and G Eyink. A public turbulence database cluster and applications to study Lagrangian evolution of velocity increments in turbulence. *Journal of Turbulence*, 9, 2008.

Z Liu, RJ Adrian, and TJ Hanratty. Large-scale modes of turbulent channel flow: transport and structure. *Journal of Fluid Mechanics*, 448:53–80, 2001.

LG Loitsiansky. Some basic laws of isotropic turbulent flow. *Technical Report 440, Central Aero-Hydrodynamic Institute, Moscow*, 1939.

J Mathew and AJ Basu. Some characteristics of entrainment at a cylindrical turbulence boundary. *Physics of Fluids*, 14(7):2065–2072, 2002.

PK Mishra, AK De, MK Verma, and V Eswaran. Dynamics of reorientations and reversals of large-scale flow in Rayleigh–Bénard convection. *Journal of Fluid Mechanics*, 668:480–499, 2011.

D Mistry, J Philip, JR Dawson, and I Marusic. Entrainment at multi-scales across the turbulent/non-turbulent interface in an axisymmetric jet. *Journal of Fluid Mechanics*, 802:690–725, 2016.

D Mistry, J Philip, and JR Dawson. Kinematics of local entrainment and detrainment in a turbulent jet. *Journal of Fluid Mechanics*, 871:896–924, 2019.

AS Monin and AM Yaglom. *Statistical fluid mechanics, volume II: mechanics of turbulence*, volume 2. 1975.

MM Neamtu-Halic, D Krug, G Haller, and M Holzner. Lagrangian coherent structures and entrainment near the turbulent/non-turbulent interface of a gravity current. *Journal of Fluid Mechanics*, 877:824–843, 2019.

MM Neamtu-Halic, D Krug, J-P Mollicone, M van Reeuwijk, G Haller, and M Holzner. Connecting the time evolution of the turbulence interface to coherent structures. *Journal of Fluid Mechanics*, 898, 2020.

MM Neamtu-Halic, JP Mollicone, M van Reeuwijk, and M Holzner. Role of vortical structures for enstrophy and scalar transport in flows with and without stable stratification. *Journal of Turbulence*, pages 1–20, 2021.

C Nore, LS Tuckerman, O Daube, and S Xin. The 1:2 mode interaction in exactly counter-rotating von Kármán swirling flow. *Journal of Fluid Mechanics*, 477: 51–88, 2003.

C Nore, DC Quiroz, L Cappanera, and J-L Guermond. Numerical simulation of the von Kármán sodium dynamo experiment. *Journal of Fluid Mechanics*, 854: 164–195, 2018.

R Ostilla-Mónico, EP Van Der Poel, R Verzicco, S Grossmann, and D Lohse. Exploring the phase diagram of fully turbulent Taylor-Couette flow. *Journal of Fluid Mechanics*, 761:1–26, 2014.

R Ostilla-Mónico, D Lohse, and R Verzicco. Effect of roll number on the statistics of turbulent Taylor-Couette flow. *Physical Review Fluids*, 1(5):054402, 2016.

NT Ouellette, H Xu, and E Bodenschatz. A quantitative study of three-dimensional Lagrangian particle tracking algorithms. *Experiments in Fluids*, 40:301–313, 2006a.

NT Ouellette, H Xu, M Bourgoin, and E Bodenschatz. An experimental study of turbulent relative dispersion models. *New Journal of Physics*, 8(6):109, 2006b.

J Panickacheril John, DA Donzis, and KR Sreenivasan. Laws of turbulence decay from direct numerical simulations. *Philosophical Transactions of the Royal Society A*, 380(2218):20210089, 2022.

KG Picha and ERG Eckert. Study of the air flow between coaxial disks rotating with arbitrary velocities in an open or enclosed space. *Proceedings of the 3rd U.S. National Congress of Applied Mechanics*, 1958.

S Poncet, R Schiestel, and R Monchaux. Turbulence modeling of the von Kármán flow: viscous and inertial stirrings. *International Journal of Heat and Fluid Flow*, 29(1):62–74, 2008.

SB Pope. *Turbulent Flows*. Cambridge University Press, 2000.

AK Prasad. Stereoscopic particle image velocimetry. *Experiments in Fluids*, 29 (2):103–116, 2000.

M Raffel, CE Willert, F Scarano, CJ Kähler, ST Wereley, and J Kompenhans. *Particle image velocimetry: a practical guide*. Springer, 2018.

F Ravelet, L Marié, A Chiffaudel, and F Daviaud. Multistability and memory effect in a highly turbulent flow: Experimental evidence for a global bifurcation. *Physical Review Letters*, 93(16):164501, 2004.

F Ravelet, A Chiffaudel, and F Daviaud. Supercritical transition to turbulence in an inertially driven von Kármán closed flow. *Journal of Fluid Mechanics*, 601: 339–364, 2008.

O Reynolds. An experimental investigation of the circumstances which determine whether the motion of water shall be direct or sinuous, and of the law of resistance in parallel channels. *Philosophical Transactions of the Royal society of London*, (174):935–982, 1883.

O Reynolds. On the dynamical theory of incompressible viscous fluids and the determination of the criterion. *Philosophical Transactions of the Royal Society of London*, (186):123–164, 1895.

LF Richardson. Atmospheric diffusion shown on a distance-neighbour graph. *Proceedings of the Royal Society of London. Series A, Containing Papers of a Mathematical and Physical Character*, 110(756):709–737, 1926.

PG Saffman. The large-scale structure of homogeneous turbulence. *Journal of Fluid Mechanics*, 27(3):581–593, 1967.

M Sinhuber, E Bodenschatz, and GP Bewley. Decay of turbulence at high Reynolds numbers. *Physical Review Letters*, 114(3):034501, 2015.

L Skrbek and SR Stalp. On the decay of homogeneous isotropic turbulence. *Physics of Fluids*, 12(8):1997–2019, 2000.

K Stewartson. On the flow between two rotating coaxial disks. *Mathematical Proceedings of the Cambridge Philosophical Society*, 49(2):333–341, 1953.

JT Stuart. On the effects of uniform suction on the steady flow due to a rotating disk. *Quarterly Journal of Mechanics and Applied Mathematics*, 7(4):446–457, 1954.

GI Taylor. The statistical theory of isotropic turbulence. *Journal of the Aeronautical Sciences*, 4(8):311–315, 1937.

GI Taylor. Production and dissipation of vorticity in a turbulent fluid. *Proceedings of the Royal Society of London. Series A-Mathematical and Physical Sciences*, 164(916):15–23, 1938a.

GI Taylor. The spectrum of turbulence. *Proceedings of the Royal Society of London. Series A-Mathematical and Physical Sciences*, 164(919):476–490, 1938b.

CD Tomkins and RJ Adrian. Spanwise structure and scale growth in turbulent boundary layers. *Journal of Fluid Mechanics*, 490:37–74, 2003.

C Tropea, AL Yarin, and JF Foss (editors). *Springer handbook of experimental fluid mechanics*, volume 1. Springer, 2007.

A Tsinober. *An informal conceptual introduction to turbulence*, volume 483. Springer, 2009.

PC Valente and JC Vassilicos. The decay of turbulence generated by a class of multiscale grids. *Journal of Fluid Mechanics*, 687:300–340, 2011.

R Volk, E Calzavarini, E Leveque, and J-F Pinton. Dynamics of inertial particles in a turbulent von Kármán flow. *Journal of Fluid Mechanics*, 668:223–235, 2011.

T von Kármán. Über laminare und turbulente reibung. *Zeitschrift für Angewandte Mathematik und Mechanik*, 1:233–252, 1921.

GA Voth, K Satyanarayan, and E Bodenschatz. Lagrangian acceleration measurements at large Reynolds numbers. *Physics of Fluids*, 10(9):2268–2280, 1998.

GA Voth, A La Porta, AM Crawford, J Alexander, and E Bodenschatz. Measurement of particle accelerations in fully developed turbulence. *Journal of Fluid Mechanics*, 469:121–160, 2002.

Z Warhaft and JL Lumley. An experimental study of the decay of temperature fluctuations in grid-generated turbulence. *Journal of Fluid Mechanics*, 88(4): 659–684, 1978.

J Westerweel, C Fukushima, JM Pedersen, and JCR Hunt. Mechanics of the turbulent-nonturbulent interface of a jet. *Physical Review Letters*, 95(17): 174501, 2005.

J Westerweel, C Fukushima, JM Pedersen, and JCR Hunt. Momentum and scalar transport at the turbulent/non-turbulent interface of a jet. *Journal of Fluid Mechanics*, 631:199–230, 2009.

B Wieneke. PIV uncertainty quantification from correlation statistics. *Measurement Science and Technology*, 26(7):074002, 2015.

M Wolf, B Lüthi, M Holzner, D Krug, W Kinzelbach, and A Tsinober. Investigations on the local entrainment velocity in a turbulent jet. *Physics of Fluids*, 24 (10):105110, 2012.

NA Worth. *Tomographic PIV measurement of coherent dissipation scale structures*. PhD thesis, University of Cambridge, 2010.

NA Worth and TB Nickels. Time-resolved volumetric measurement of fine-scale coherent structures in turbulence. *Physical Review E*, 84:025301, 2011.

A Zampiron, S Cameron, and V Nikora. Secondary currents and very-large-scale motions in open-channel flow over streamwise ridges. *Journal of Fluid Mechanics*, 887:A17, 2020.

PJ Zandbergen and D Dijkstra. Von Kármán swirling flows. *Annual Review of Fluid Mechanics*, 19(1):465–491, 1987.

H Zhang and X Wu. Dynamics of turbulent and nonturbulent interfaces in cylinder and airfoil near wakes. *AIAA Journal*, 60(1):261–275, 2022.

G Zocchi, P Tabeling, J Maurer, and H Willaime. Measurement of the scaling of the dissipation at high Reynolds numbers. *Physical Review E*, 50(5):3693, 1994.

Article 1

Entrainment, detrainment and enstrophy transport by small-scale vortex structures

Farid Aligolzadeh, Markus Holzner and James R. Dawson

Published in Journal of Fluid Mechanics

J. Fluid Mech. (2023), *vol.* 973, A5, doi:10.1017/jfm.2023.745

JFM PAPERS

Entrainment, detrainment and enstrophy transport by small-scale vortex structures

Farid Aligolzadeh[1,†], **Markus Holzner**[2,3] **and James R. Dawson**[1]

[1]Department of Energy and Process Engineering, Norwegian University of Science and Technology, N-7491 Trondheim, Norway

[2]Swiss Federal Institute of Forest, Snow and Landscape Research WSL, 8903 Birmensdorf, Switzerland

[3]Swiss Federal Institute of Aquatic Science and Technology Eawag, 8600 Dübendorf, Switzerland

(Received 18 May 2023; revised 3 August 2023; accepted 3 September 2023)

The interaction of small-scale vortical structures with the surrounding fluid are studied using a fully resolved three-dimensional experimental data set of homogeneous turbulence measured at the centre of a von Kármán mixing flow facility and a direct numerical simulation (DNS) data set of forced isotropic turbulence. To identify the small-scale vortices and their boundaries, an objective observer-independent definition was implemented to avoid arbitrariness and is the first implementation applied to experimental measurements of small-scale turbulence. Volume-averaged and conditional statistics are presented to demonstrate consistency between the experimental and DNS data sets. To examine the interaction of the structures with the surrounding flow field, we examine the flow across the boundary of vortex structures by adopting a similar methodological approach to that used to investigate the local entrainment and detrainment across the turbulent–non-turbulent interface. The probability density function (p.d.f.) of entrainment velocity conditioned on the vortex boundary exhibited a non-Gaussian distribution that skewed slightly in favour of entrainment and is remarkably similar to the p.d.f.s of entrainment velocity observed in boundary layers and jets. We analyse the enstrophy transport equation conditioned on radial and axial coordinates of the vortices to quantify the inviscid and viscous components of the entrainment/detrainment process. A comparison with Burgers vortices is made and it is found that the Burgers vortex model captures the vortex structure average size and the mechanisms of enstrophy transport in the radial direction, but is unable to capture local statistics and describe the governing physics along the axes of the vortices.

Key words: homogeneous turbulence, vortex dynamics

---

† Email address for correspondence: farid.aligolzadeh@ntnu.no

1. Introduction

The nature and structure of small-scale vortex structures have received considerable attention in turbulence research and are typically defined as concentrated regions of high enstrophy with life-times greater than the characteristic time scale of the flow (Dubief & Delcayre 2000). These vortex tubes, filaments or so-called worms are the most prominent small-scale structures at the dissipation scale having been identified in early numerical simulations and experimentally observed by, amongst others, Siggia (1981), Kerr (1985), She, Jackson & Orszag (1990), Vincent & Meneguzzi (1991), Cadot, Douady & Couder (1995), Jiménez *et al.* (1993), Jiménez & Wray (1998) and Ishihara, Gotoh & Kaneda (2009). Over the last few decades, the growth in computational power and new experimental methods have enabled observation of small-scale vortices at ever higher Reynolds numbers and in an increasingly wide range of flows. They appear to have some universal features such as the preferential alignment of the vorticity vector with the direction of intermediate principal strain found by Ashurst *et al.* (1987) and their average radius of about 5η, where η is the Kolmogorov length scale, as verified in homogeneous isotropic turbulence (Jiménez *et al.* 1993; Jiménez & Wray 1998; Ghira, Elsinga & Da Silva 2022), jets (Ganapathisubramani, Lakshminarasimhan & Clemens 2008; da Silva, dos Reis & Pereira 2011), channel flows (Kang, Tanahashi & Miyauchi 2009) and stratified flows (Neamtu-Halic *et al.* 2021). Although the alignment of the vorticity vector with the intermediate principal strain holds at small scales, and has been observed in a wide range of flows, at larger length scales the vorticity preferentially aligns instead with the most stretching principal strain (Ishihara, Yamazaki & Kaneda 2001; Leung, Swaminathan & Davidson 2012).

In the seminal direct numerical simulation (DNS) of homogeneous isotropic turbulence by Jiménez *et al.* (1993), it was found that small-scale vortex tubes produced low levels of stretching demonstrating that self-amplification did not play a significant role in their evolution. Jiménez *et al.* (1993) draw attention to the resemblance between these small-scale vortices and axially stretched stable Burgers vortices by considering their stability and lack of coupling with the strain field. The implication of this is significant as it showed that at the small scale, these high-enstrophy vortex structures do not play a significant role in the overall dynamics of the flow and can therefore be considered passive. This was also emphasized by Tsinober (2009), who noted that the lack of self-amplification via interaction with the strain field means that the worms are rather passive and decoupled from the strain field. This is in direct contrast with sheet-like, strained vortices whose presence modifies the local strain field significantly (Moffatt, Kida & Ohkitani 1994; Le Dizes, Rossi & Moffatt 1996; Davidson 2015). In a later study, Jiménez & Wray (1998) investigated the relationship between stretching at the points of maximum vorticity inside the worms with their corresponding radii. The joint probability density function (p.d.f.) of these two parameters showed good agreement with the values of radii based on the stable Burgers vortex model. These observations have been expanded to include other flows, for example the turbulent plane jet by da Silva *et al.* (2011). However, the lack of interaction with the strain field does not mean that vortex tubes do not interact with the local flow in other important ways, for example through the exchange of mass and momentum with their surroundings. These interactions have not been investigated in detail to date. In this paper we employ a fully resolved experimental data set and DNS to investigate the interaction of vortex filaments with the surrounding flow. This is done by implementing a robust method to detect the boundary of the vortices and then analysing conditional flow features to show that they entrain and detrain mass and momentum.

When it comes to precisely defining and detecting small-scale vortical structures, researchers usually adopt one of two well-known and broadly used approaches:

thresholding on the vorticity (Hussain 1986; Jiménez *et al.* 1993; da Silva *et al.* 2011; Ghira *et al.* 2022) or the vorticity relative to the strain field (Hua & Klein 1998). The problem with these classical detection methods is that they are arbitrary and depend on the observer's frame of reference (Haller 2005). For instance, using classical detection methods, an observer in fixed laboratory coordinates will not identify the same vortex structures as an observer that is moving with the flow. Methods developed in a recent string of research articles, summarized in the review paper by Haller (2015), have been shown to overcome these limitations and permit identification of objective (i.e. observer-independent) coherent structures necessary for repeatable experiments. The method proposed by Haller *et al.* (2016) to detect rotationally coherent structures from the vorticity field was previously adapted and implemented to identify large-scale vortex structures in three-dimensional turbulence measurements of a gravity flow by Neamtu-Halic *et al.* (2019). The primary advantage of this method is that it provides an objectively defined vortex boundary permitting an investigation of the conditional fluxes across it to reveal how small-scale vortical structures interact with the surrounding flow from both a local and global perspective.

The aim of this study is to investigate the interaction of objectively identified small-scale vortical structures in more detail than what has been done so far in the literature to obtain a better understanding of their interaction with the surrounding flow. We adopt an approach which treats them as turbulent structures embedded in a turbulent background flow and borrows a similar methodological approach to that used to investigate local entrainment across turbulent–non-turbulent interfaces (TNTIs) as exemplified by Mathew & Basu (2002), Westerweel *et al.* (2005), Holzner & Lüthi (2011), Wolf *et al.* (2012), Mistry *et al.* (2016) and Mistry, Philip & Dawson (2019) in order to evaluate their interaction with the surrounding flow by evaluating the enstrophy transport equation which enables direct comparison with the Burgers vortex model. (Although we adopt a similar methodology to that of these studies, we are not suggesting an equivalence between the boundary of a vortex structure and the TNTI.) To do this we make use of two data sets. The first is a fully resolved three-dimensional experimental data set of stationary homogeneous turbulence measured at the centre of a von Kármán mixing flow with a Reynolds number based on the Taylor microscale of $R_\lambda = 179$ (Lawson & Dawson 2014, 2015). Until recently, experimental access to the full velocity gradient tensor of small-scale turbulence at reasonably high Reynolds number has remained elusive and almost all previous studies of small-scale vortical structures have been restricted to DNS data sets without an experimental counterpart. This is the first time that the three-dimensional objective vortex definition of Haller *et al.* (2016) has been implemented on an experimental data set of resolved small-scale turbulence. To complement the experimental data set, results are compared with the DNS data set of homogeneous isotropic turbulence of Li *et al.* (2008) at $R_\lambda = 418$.

The paper is organized as follows. Section 2 describes the large-scale von Kármán facility, a brief description of the experimental data set from Lawson & Dawson (2014, 2015) and the implementation of the detection method by Haller *et al.* (2016) for objective Eulerian coherent structures (OECS) as well as how to calculate the entrainment velocity from the enstrophy transport equation derived by Holzner & Lüthi (2011). The results in § 3 begin with presenting volume-averaged and conditional statistics of the small-scale vortices to illustrate consistency between the experimental and DNS data sets. Attention is then turned to statistics of entrainment and the balance of the different terms in the enstrophy transport equation. The enstrophy balance is considered from two different perspectives, the first being conditioning on the radial direction of the vortices and the

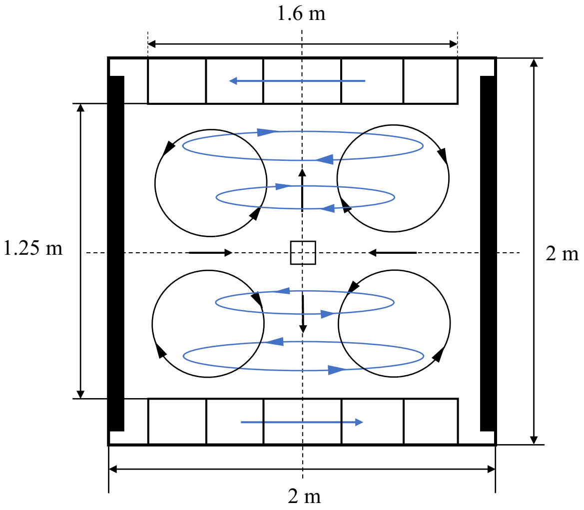

Figure 1. Two-dimensional schematic of the large tank facility with dimensions. The blue lines show the flow pattern in azimuthal (horizontal) planes and the black lines show the flow pattern in an axial (vertical) plane passing the geometric centre of the tank. The measurement volume is represented by a square at the centre of the tank.

second from conditioning on their axes. The results are discussed and interpreted in the context of expected quantities from the Burgers vortex model.

2. Methods

2.1. *Description of facility and data sets*

The experimental data set used in this study is from the scanning particle image velocimetry measurements of homogeneous axisymmetric turbulence produced by the large von Kármán mixing flow facility reported in Lawson & Dawson (2014, 2015). Due to the large size of the facility and the slow rotation rate of the impellers, spatially and temporally resolved measurements at the Kolmogorov scale were achievable. A two-dimensional schematic of the experimental facility is shown in figure 1 highlighting key dimensions and the general flow pattern. The flow inside the tank can be considered a superposition of a stationary axisymmetric shear flow generated by the counter-rotating impellers and a centrifugal pumping leading to a radially inward flow along the mid-plane of the tank and axial flow away from the geometric centre along the rotational symmetry axis. The shear generated by the counter-rotation of the impellers results in a region of homogeneous, axisymmetric turbulence near the centre of the tank with a near-zero mean velocity in all directions (Lawson & Dawson 2014, 2015).

The facility is comprised of a large dodecagonal Perspex tank that is 2 m tall and 2 m in cross-section that was filled with water. The impellers at the top and bottom of the tank were 1.6 m in diameter and operated at constant angular velocity in a counter-rotating mode. Vertical baffles were placed at each vertex with the same height as the tank protruding 100 mm into the flow. The Reynolds number based on the impeller radius defined as $Re = \Omega_I R_I^2/\nu$, where Ω_I is the rate of rotation of the impellers, R_I is the radius of the impellers and ν is the kinematic viscosity of the flow, was 23 000. The Reynolds number based on Taylor microscale was $R_\lambda = 179$ and the Kolmogorov length scale was $\eta = 0.926$ mm. The measurement volume was located at the geometric centre of the tank with dimensions $L_x \times L_y \times L_z = 129\,\text{mm} \times 128\,\text{mm} \times 26.2\,\text{mm}$. The spatial resolution of the data set was approximately 1η over a non-dimensional measurement volume of $L_x/\eta \times L_y/\eta \times L_z/\eta = 135 \times 134 \times 25.4$. The data set consists of 1003 statistically independent volumes constructed from a time series of 10 volumetric vector fields with a particle image velocimetry separation time of $\approx 0.068\tau_\eta$, where τ_η is the Kolmogorov time scale. There was no spatial averaging applied to the data. A predictor-corrector scheme was implemented in a Lagrangian tracking algorithm performing forward and backward in time over the time-resolved velocity fields to minimize noise (Novara & Scarano 2013). The data set is of very low noise and highly resolved enabling direct comparisons with DNS up to third-order gradient statistics (Lawson & Dawson 2014, 2015).

A DNS data set of forced isotropic turbulence of $R_\lambda = 418$ from the Johns Hopkins Turbulence Database (Li *et al.* 2008) was also analysed for comparison with the experimental data set. This DNS data set is a time series of a periodic forced cube with 1024^3 nodes over five large-eddy turnover times. Fifty independent volumes of the flow (snapshots of the cubes with 128^3 nodes) with a dimension size of $L_x/\eta \times L_y/\eta \times L_z/\eta = 279 \times 279 \times 279$ were chosen at random time steps over the five large-eddy turnover times. The spatial resolution is about 2.2η.

2.2. *Detection of OECS*

To analyse the intense small-scale vortex structures a robust detection method based on the definition of OECS proposed by Haller *et al.* (2016) was implemented. The OECS are detected using a scalar field corresponding to the instantaneous vorticity deviation (IVD) which is defined in (2.1):

$$\mathrm{IVD}(\boldsymbol{x}, t) = |\boldsymbol{\omega}(\boldsymbol{x}, t) - \bar{\boldsymbol{\omega}}(t)|, \tag{2.1}$$

where $\boldsymbol{\omega}(\boldsymbol{x}, t)$ is the vorticity vector at the time step t at point $\boldsymbol{x}$ in space and $\bar{\boldsymbol{\omega}}(t)$ is the average value of vorticity over the volume of the flow at the time step t. Since the DNS is homogeneous and isotropic and the experimental data are also approximately homogeneous and isotropic with negligible mean flow, the normalization by the volumetric average is not sensitive to volume size. However, in other flows that are not homogeneous and isotropic, the normalization by the volumetric average in the OECS method may introduce a dependence of the results on volume size that should be taken into account. This definition is an observer-independent (objective) scalar field that represents the local rotation rate of fluid elements. The OECS are defined as a nested family of tubular level surfaces of $\mathrm{IVD}(\boldsymbol{x}, t)$ in which the value of $\mathrm{IVD}(\boldsymbol{x}, t)$ is non-increasing when moving outward from the centre. Along each of these tubular surfaces the rotation rates of the fluid elements are equal. The boundary is defined as the outermost almost convex level surface of $\mathrm{IVD}(\boldsymbol{x}, t)$ and the centre is the maximum level surface of the nested family. As discussed in Haller *et al.* (2016), this definition detects vortical structures that are observer-independent and ensures instantaneous coherence in the rate of their material bulk rotation. No thresholding is therefore needed to define/detect these vortical structures. We refer the reader to Haller (2015) and Haller *et al.* (2016) for further details.

The numerical detection algorithm used to detect the three-dimensional OECS to the data set of Lawson & Dawson (2015) is described in detail by Neamtu-Halic *et al.* (2019). Therefore we only provide a brief description of the detection algorithm for completeness. The detection algorithm consists of three main steps. In the first step, the vorticity field is evaluated followed by the IVD scalar field according to (2.1). In the second step, ridges corresponding to the local maximum values of the IVD are detected using a three-dimensional gradient ascent method starting from point clouds of high spatial gradient of IVD values as the initial guess. The Cauchy–Lipschitz theorem was used to solve the ordinary differential equation of the gradient ascent algorithm. The ridges represent the centre lines of the vortex structures. In the third step, two-dimensional contours of IVD are calculated on planes locally normal to the ridges which are then used to build three-dimensional level surfaces for the structures. The outermost convex level surface is chosen as the boundary of the structure. Successful implementation for the detection of small-scale structures requires a fully resolved three-dimensional three-component velocity field with low levels of noise. So far, this has only been applied to the experimental data set by Neamtu-Halic *et al.* (2019) where the resulting structures were comparatively large on average ($R \approx 15\eta$).

2.3. *Equations and models*

To investigate the flow field within and immediately surrounding the vortex filaments as well as compare with the Burgers vortex model, the detected boundaries of the vortex filaments are treated with the methodological approach applied to the TNTI enabling the investigation of the fluxes passing across it. To do this we evaluate various terms in the enstrophy transport equation (2.2), where the first term on the right-hand side ($2\omega_i\omega_j s_{ij}$) corresponds to the inviscid production/destruction of enstrophy by vortex stretching/compression, the second term ($\nu(\partial^2\omega^2/\partial x_j\partial x_j)$) is the viscous diffusion of enstrophy due to the presence of gradients and the final term ($-2\nu(\partial\omega_i/\partial x_j)(\partial\omega_i/\partial x_j)$) corresponds to the viscous dissipation of enstrophy (Pope 2000; Tsinober 2009):

$$\frac{\mathrm{D}\omega^2}{\mathrm{D}t} = 2\omega_i\omega_j s_{ij} + \nu\frac{\partial^2\omega^2}{\partial x_j\partial x_j} - 2\nu\frac{\partial\omega_i}{\partial x_j}\frac{\partial\omega_i}{\partial x_j}. \tag{2.2}$$

Using the enstrophy transport equation, Holzner & Lüthi (2011) derived an equation for the entrainment velocity, v_n, which can be applied at the boundary of the structures:

$$v_n = -\frac{2\omega_i\omega_j s_{ij}}{|\boldsymbol{\nabla}\boldsymbol{\omega}^2|} - \frac{\nu\dfrac{\partial^2\omega^2}{\partial x_j\partial x_j}}{|\boldsymbol{\nabla}\boldsymbol{\omega}^2|} + \frac{2\nu\dfrac{\partial\omega_i}{\partial x_j}\dfrac{\partial\omega_i}{\partial x_j}}{|\boldsymbol{\nabla}\boldsymbol{\omega}^2|}, \tag{2.3}$$

where the entrainment velocity, v_n, is defined as $\boldsymbol{V} = v_n\hat{\boldsymbol{n}} = \boldsymbol{u}^s - \boldsymbol{u}$. In this definition, $\boldsymbol{u}^s$ is the velocity vector of an iso-surface element, for example the boundary of the vortex structure, $\boldsymbol{u}$ is the fluid velocity vector at the iso-surface and $\hat{\boldsymbol{n}} = \boldsymbol{\nabla}\boldsymbol{\omega}^2/|\boldsymbol{\nabla}\boldsymbol{\omega}^2|$ is the iso-surface normal vector. Based on this definition, $v_n \leq 0$ corresponds to the entrainment of fluid from the surroundings into the structures whereas $v_n > 0$ corresponds to the detrainment of fluid from inside the structures to the surrounding fluid (Holzner & Lüthi 2011; Mistry *et al.* 2019). Based on the entrainment velocity, the local flux of other quantities across the boundary can be calculated through multiplication with v_n. For example, the specific flux of enstrophy defined as $v_n\omega^2$ and the kinetic energy $v_n u_i u_i$. Equation (2.3) is valid on an iso-surface of enstrophy and follows from the fact that for an observer moving with an iso-surface (denoted by the superscript s) the iso-level is constant, i.e. $D^s\omega^2/D^s t = 0$ (Holzner & Lüthi 2011). According to the definition of the IVD in (2.1) and given that $\bar{\boldsymbol{\omega}}(t)$ is a constant under statistically stationary and homogeneous conditions, it follows that $D^s\omega^2/D^s t = 0$ and $D^s(\mathrm{IVD})/D^s t = 0$ are interchangeable. Thus, (2.3) can be used to calculate the entrainment velocity at the boundary of detected vortex structures where the IVD is considered.

We also compare features of the small-scale vortical structures with the classical Burgers vortex model to further elucidate similarities and differences. For a Burgers vortex (Burgers 1948), it is assumed that the flow is incompressible and the vorticity field is unidirectional. The vorticity field is normally assumed to be one-dimensional or both the vorticity field and the strain field axisymmetric (Saffman 1995). A sketch of Burgers vortex is shown in figure 2. The stability of the Burgers vortex results from a balance between the inviscid effects of vortex stretching and viscous effects of vorticity diffusion and dissipation. This leads to outflow along the axis of symmetry (u_z) and radial entrainment (u_r) to maintain the rotational energy and mass conservation. The radial velocity is shown in (2.4) where $\alpha > 0$ is the strain of the flow and it is a constant. Equation (2.5) governs the enstrophy profile where R_B is the Burgers vortex radius and ν is the kinematic viscosity. In the Burgers vortex model all the terms in the enstrophy transport equation (2.2) can be evaluated analytically by using (2.5)–(2.9) (Taveira & da Silva 2014; Davidson 2015; Watanabe *et al.* 2017).

$$u_r(r) = -\tfrac{1}{2}\alpha r, \tag{2.4}$$

$$\omega_z(r) = \omega_0 \exp\left(-\frac{r^2}{R_B^2}\right);\ \omega_0 = \omega(r=0),\ R_B^2 = \frac{4\nu}{\alpha}, \tag{2.5}$$

$$2\omega_i\omega_j s_{ij} = 2\omega_z^2(r)\alpha = 2\omega_0^2\alpha \exp\left(-2\frac{r^2}{R_B^2}\right), \tag{2.6}$$

$$\nu\frac{\partial^2\omega^2}{\partial x_j\partial x_j} = \nu\frac{1}{r}\frac{\partial}{\partial r}\left(r\frac{\partial\omega_z^2(r)}{\partial r}\right) = 2\alpha\omega_0^2\left(2\frac{r^2}{R_B^2}-1\right)\exp\left(-2\frac{r^2}{R_B^2}\right), \tag{2.7}$$

$$-2\nu\frac{\partial\omega_i}{\partial x_j}\frac{\partial\omega_i}{\partial x_j} = -2\nu\left(\frac{\partial\omega_z(r)}{\partial r}\right)^2 = -2\alpha\omega_0^2\left(\frac{r^2}{R_B^2}\right)\exp\left(-2\frac{r^2}{R_B^2}\right), \tag{2.8}$$

$$\frac{\mathrm{D}\omega^2}{\mathrm{D}t} = u_r(r)\frac{\partial\omega_z^2(r)}{\partial r} = 2\alpha\omega_0^2\left(\frac{r^2}{R_B^2}\right)\exp\left(-2\frac{r^2}{R_B^2}\right). \tag{2.9}$$

$$\tag{1}$$

3. Results

3.1. *Statistics of the structures and the flow field*

In this section, volume-averaged statistics and statistics conditioned on the inside of the structures from both the experimental and DNS data sets are presented and discussed. An example of the objectively identified three-dimensional intense vortical structures in a measured volume of the flow is shown in figure 3(*a*). The black curved lines denote the centre of the structures, the magenta surfaces the boundary of each structure and the colour shading corresponds to the normalized enstrophy field, $\omega^2/\langle\omega^2\rangle_s$, where $\langle\sim\rangle_s$ is the volume average of the corresponding snapshot. In total, 12 466 structures were detected over the 1003 snapshots of the experimental data set. A similar example is shown in figure 3(*b*) obtained from a single volume of the DNS data set. Overall 9274 structures were detected over the 50 snapshots of the DNS data set.

Figure 4 shows the p.d.f.s of the normalized radius of the structures for the experiment and DNS defined as $R^* = R/\eta$, where R is the distance between the centre of the structure

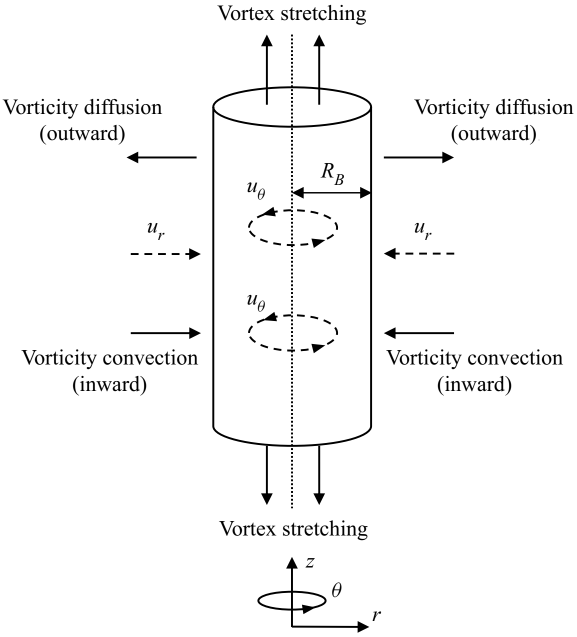

Figure 2. The Burgers vortex model.

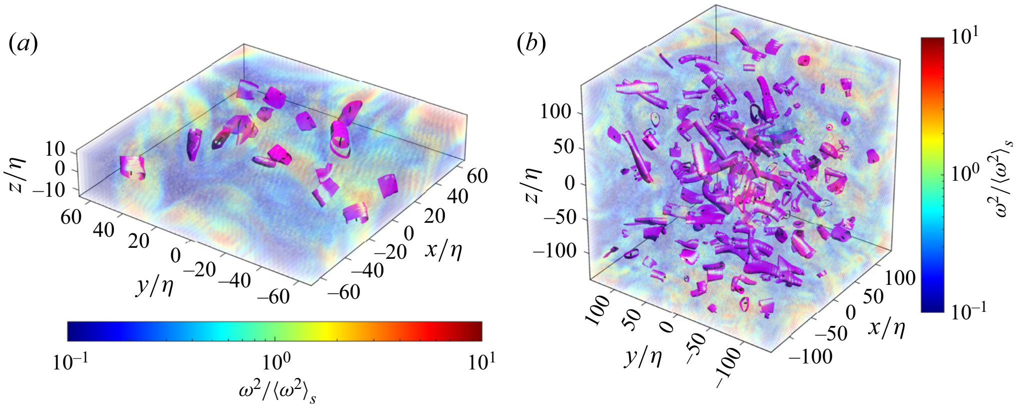

Figure 3. Examples of the structures (magenta surfaces) in single volumes of the (*a*) experimental and (*b*) DNS data sets with the corresponding enstrophy values. The enstrophy values are normalized by the corresponding volume average of the snapshots, $\langle\omega^2\rangle_s$. The spatial dimensions are normalized by the Kolmogorov length scale, η.

and its boundary. As the cross-sections of the structures are contorted, the radii are evaluated at various random points along the boundary of each structure with the average radius of the structures found to be $\langle R\rangle = 5.1\eta$ which is in a good agreement with previous studies (Jiménez *et al.* 1993; Ganapathisubramani *et al.* 2008; da Silva *et al.* 2011; Neamtu-Halic *et al.* 2021). The volume of the structures occupied 1.4 % of the whole volume of the flow field which is also in a good agreement with the value of ≈1 % reported by Jiménez *et al.* (1993). This confirms that both the identification method and the experimental data set are sufficiently well resolved and consistent with DNS as expected from previous work of Lawson & Dawson (2015).

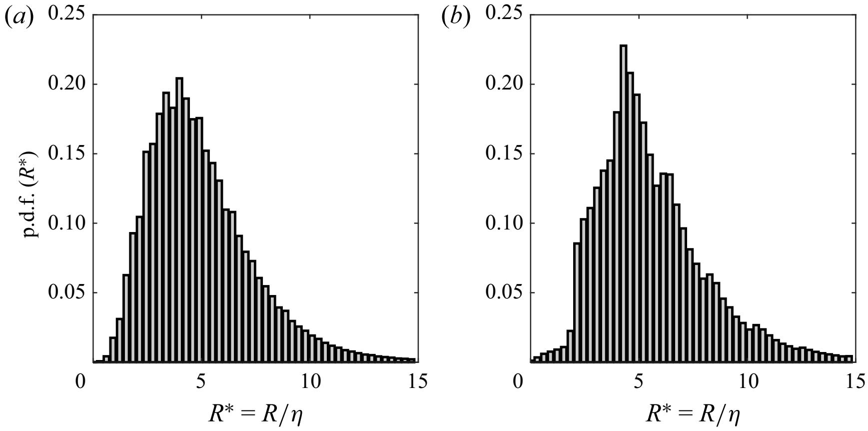

Figure 4. The p.d.f.s of normalized radius of the structures (R/η) of the (*a*) experimental and (*b*) DNS data sets.

The objective detection method used herein initially follows similar steps to the thresholding method used in Jiménez *et al.* (1993). However, the methods diverge once the process of determining the centre lines of the vortex structures takes place. In Jiménez *et al.* (1993) the enstrophy profile of the vortex is assumed to decay exponentially to detect the boundary, whereas the objective detection method detects the outermost almost convex iso-surface as the boundary. Thus, one might expect small variations in the radii of the detected vortex structures to occur depending on the method. However, figure 4, i.e. p.d.f.(R/η), is similar to the analogous figures in the works of Jiménez *et al.* (1993), Jiménez & Wray (1998), da Silva *et al.* (2011) and Ghira *et al.* (2022) where the thresholding detection method is used giving confidence that the two methods yield similar results for resolved homogeneous and isotropic data sets.

To quantify the rotational energy and intermittency of the small-scale structures, p.d.f.s of normalized enstrophy $\omega^2/\langle\omega^2\rangle$ are plotted in figure 5(*a*) for the experiment (black lines) and DNS (grey lines), where $\langle\omega^2\rangle$ is the enstrophy spatially averaged over the whole measurement volume and all the snapshots. The dashed lines show the p.d.f.s throughout the volume, whereas the solid lines show the p.d.f.s conditioned on the inside of the structures. A logarithmic binning is used to calculate the p.d.f.s and are plotted on log – log scale. Good agreement is found across the data sets. The p.d.f.s from the experiment and DNS both intersect at around $\omega^2/\langle\omega^2\rangle = 1$. When $\omega^2/\langle\omega^2\rangle < 1$, the p.d.f.s of the volumetric enstrophy are significantly higher and peak at $\omega^2/\langle\omega^2\rangle \approx 10^{-2}$ and also extend to much lower values $\omega^2/\langle\omega^2\rangle \approx 10^{-6}$ than the p.d.f.s conditioned on the inside of the structures. When $\omega^2/\langle\omega^2\rangle > 1$, conditioned on the structures shows slightly greater enstrophy values before falling off with similar values to the volumetric average. The p.d.f.s show that increasingly high-enstrophy events are similarly rare in the volume-averaged and conditional statistics, whereas low-enstrophy events are much less prevalent for the conditioned statistics.

We can draw a similar comparison between the local and volumetric dissipation where it is normalized as $\epsilon/\langle\epsilon\rangle$. The dissipation, ϵ, is defined as $\epsilon = 2\nu s_{ij}s_{ij}$, where ν is the kinematic viscosity of the flow and $s_{ij} = (\partial u_i/\partial x_j + \partial u_j/\partial x_i)/2$ is the rate of strain tensor. The ensemble average dissipation is denoted as $\langle\epsilon\rangle$ and evaluated over the full data set. Figure 5(*b*) shows the p.d.f.s of the normalized dissipation for the whole volume (dashed lines) and conditioned on the inside of the structures (solid lines) for both the experiments

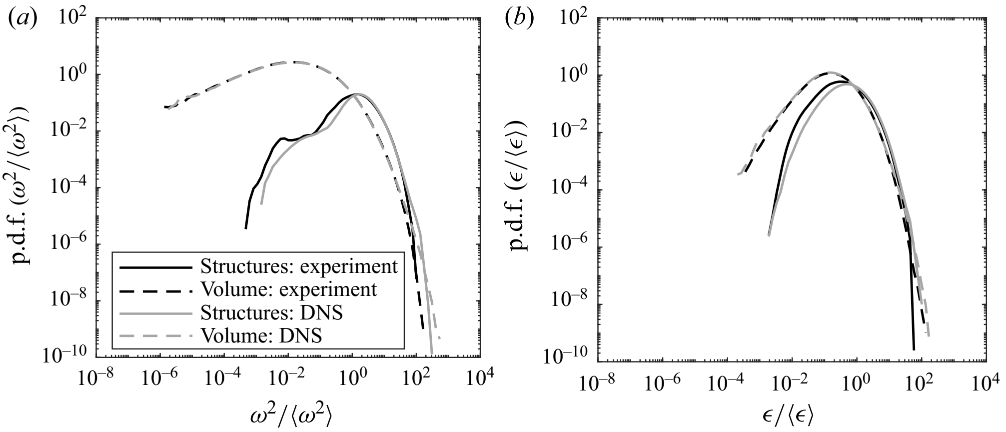

Figure 5. The p.d.f.s of normalized (*a*) enstrophy and (*b*) dissipation of the structures (solid lines) and volume (dashed lines). The black curves represent the experiment and the grey curves represent DNS.

and DNS. Again it is observed that the volumetric and conditioned p.d.f.s intersect when $\epsilon/\langle\epsilon\rangle = 1$. When $\epsilon/\langle\epsilon\rangle > 1$ the p.d.f.s show that the structures contribute slightly higher dissipation compared with the volume. On the other hand, the structures contribute less than the total volume when $\epsilon/\langle\epsilon\rangle < 1$. Nevertheless, the small-scale vortices still produce significant dissipation. Similar to the p.d.f.s of enstrophy, the probability that the vortex structures contain higher dissipation events is greater when compared to the whole volume. However, the difference for dissipation is not as large as for the case of enstrophy. This means that the structures are an intense realization of enstrophy with some overlap with regions of high dissipation/strain in the flow field (Davidson 2015).

To better understand the relationship between enstrophy and dissipation, spatial correlations in the from of joint p.d.f.s (j.p.d.f.s) are plotted in figure 6. These show that the volumetric j.p.d.f.s (dashed contours) for the experimental and DNS data sets exhibit a similar distribution to that reported in Yeung, Donzis & Sreenivasan (2012). When conditioned on the inside of the small-scale structures, shown by the solid contours, the j.p.d.f.s are shifted upwards and to the right towards higher values of enstrophy and dissipation. The j.p.d.f.s also show a preferred diagonal alignment (more symmetric with respect to the diagonal) which is consistent with an increase in local R_λ as discussed in the work of Yeung *et al.* (2012). This means that there is a preferential increase in the joint probability of extreme events of enstrophy and dissipation inside the structures. Furthermore, enstrophy and dissipation appear to scale similarly inside the structures which suggests a physical dependence between vorticity and strain even though it is not clear which one of them is the cause and which one is the effect (Jiménez *et al.* 1993).

The importance of the relationship between vorticity and the rate of strain dates back to Taylor (1938) who postulated that the stretching of small-scale vortices caused them to break up into yet smaller vortices and was therefore expected to be an important mechanism in the turbulent cascade. However, it was not until the DNS work by Ashurst *et al.* (1987) which permitted access to the full velocity gradient tensor which showed that instantaneously, the vorticity vector is aligned with the intermediate eigenvector of the rate of strain tensor, rather than the extensive eigenvector, and is predominantly positive. The alignment of the vectors is observer-independent and is important to the phenomenon of vortex stretching ($2\omega_i\omega_j s_{ij}$) which produces enstrophy (Tsinober 2009).

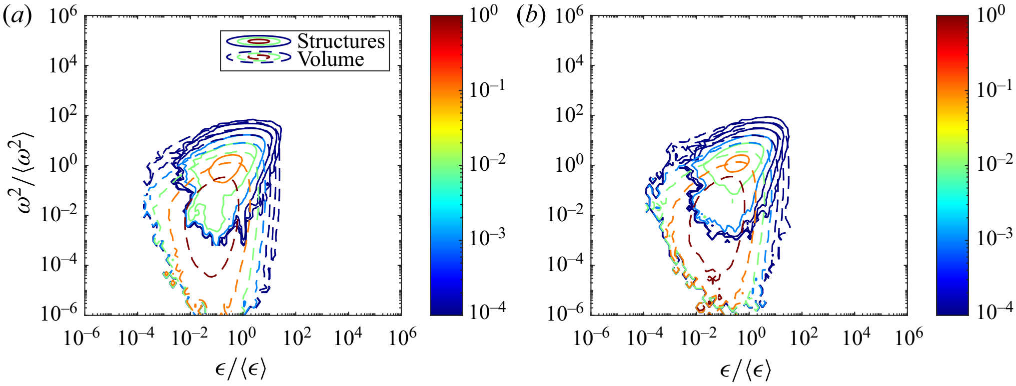

Figure 6. Joint p.d.f.s of normalized enstrophy and dissipation for the (*a*) experiment and (*b*) DNS. The solid contours represent the structures and the dashed contours represent the volume.

The alignment between the vorticity vector $\boldsymbol{\omega} = (\omega_1, \omega_2, \omega_3)$ and the eigenvectors of the rate of strain tensor $\boldsymbol{e} = (\boldsymbol{e}_1, \boldsymbol{e}_2, \boldsymbol{e}_3)$, where ordering of the eigenvalues is $\sigma_1 \geq \sigma_2 \geq \sigma_3$, can be investigated by plotting the cosine of the angles between these vectors: $\cos\theta_i = \boldsymbol{e}_i \boldsymbol{\cdot} \boldsymbol{\omega}/|\boldsymbol{\omega}|$. From the continuity equation, it follows that the sum $\sigma_1 + \sigma_2 + \sigma_3 = 0$ which means that σ_1 is always positive and its corresponding eigenvector, $\boldsymbol{e}_1$, is the extensive eigenvector. In contrast, σ_3 is always negative and its corresponding eigenvector, $\boldsymbol{e}_3$, is compressive. The value of σ_2 is determined by the sum of σ_1 and σ_3 and can be either negative or positive and is the intermediate eigenvalue with a corresponding eigenvector, $\boldsymbol{e}_2$.

The p.d.f.s of the cosine of the angles between the vorticity vector and the eigenvectors are plotted in figure 7(*a*,*b*) where the solid and dashed lines correspond to the alignments conditioned on the inside of the structures and the volume, respectively. Overall, the experimental data and DNS show excellent agreement. Considering the volume-based statistics first, the vorticity vector and the intermediate eigenvector are well aligned with each other as the peak values of the p.d.f.s occur at $\cos\theta_2 = \pm 1$ and appears to be a universal aspect of turbulent flow (Elsinga & Marusic 2010). The alignment between the vorticity vector and the compressive eigenvector shows a peak at $\cos\theta_3 = 0$ showing that the two vectors are predominantly normal to each other, whereas the extensive eigenvector indicates no preferential alignment. When conditioned on the structures, the vorticity vector is also aligned with the intermediate eigenvector but it is normal to both the extensive and compressive eigenvectors. A much higher peak at $\cos\theta_3 = 0$ is observed when conditioned on the inside of the structures. These results indicate that vorticity vectors inside the structures exhibit a strong preferred alignment with the intermediate eigenvector but normal to the extensive and compressive eigenvectors (Frisch 1995; Tsinober 2009; Buaria, Bodenschatz & Pumir 2020). Since the vorticity vector is only aligned with the intermediate eigenvector, we consider the distribution of the eigenvalues and, in particular, σ_2. Figure 8(*a*,*b*) plots p.d.f.s of eigenvalues of the rate of strain tensor for the same cases as considered in figure 7. As expected, $\sigma_1 > 0$ and $\sigma_3 < 0$ for the volume and structures whereas the p.d.f. of σ_2 contains both negative and positive values but is positive on average, $\langle\sigma_2\rangle > 0$. An insight into enstrophy production is gained by considering the average vortex stretching which can be written as $\langle 2\omega_i\omega_j s_{ij}\rangle = 2\omega^2(\langle\sigma_1\cos^2\theta_1\rangle + \langle\sigma_2\cos^2\theta_2\rangle + \langle\sigma_3\cos^2\theta_3\rangle)$ (Tsinober 2009). This relation is used to calculate the shares, relative to each alignment, in the total

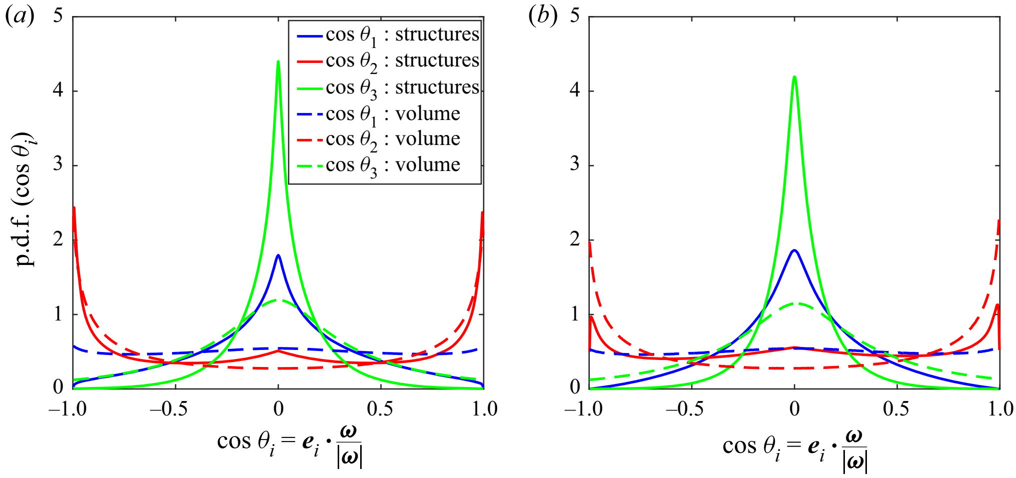

Figure 7. Alignment between vorticity vector and the eigenvectors of the rate of strain tensor for the (*a*) experiment and (*b*) DNS. The solid lines represent the structures and the dashed lines represent the volume.

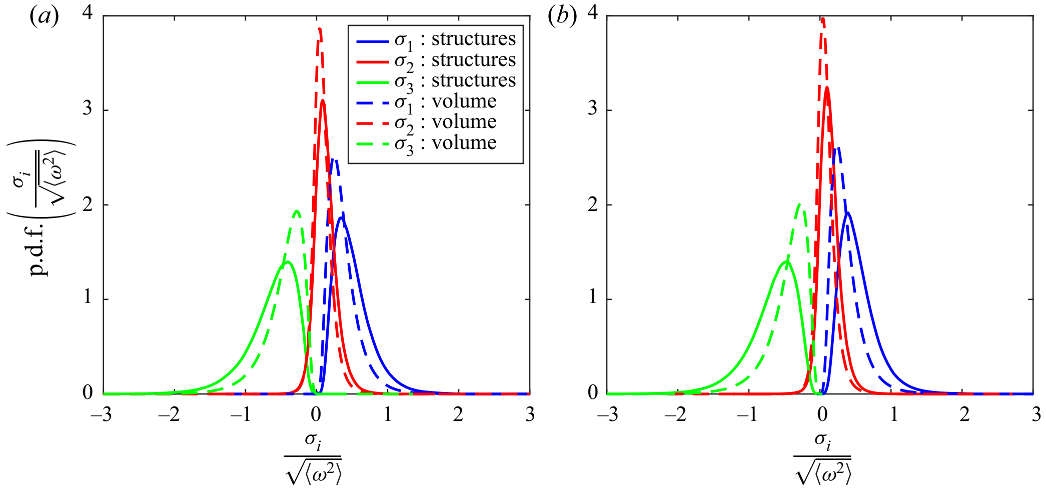

Figure 8. The p.d.f.s of the normalized eigenvalues of the rate of strain tensor for the (*a*) experiment and (*b*) DNS. The solid lines represent the structures and the dashed lines represent the volume.

production/destruction of enstrophy, i.e. $\langle \sigma_j \cos^2\theta_j\rangle/\sqrt{\sum\langle\sigma_i\cos^2\theta_i\rangle^2}$. This is shown in table 1. Clearly the contributions of the extensive and compressive eigenvalues become weaker in favour of the intermediate eigenvalue inside the structures as expected from figure 7. However, the contribution from the extensive eigenvalue remains prominent and, overall, the ratio of enstrophy production to destruction increases. This is consistent with the picture that, on average, the production of enstrophy via vortex stretching inside the structures is more significant compared with the flow field as a whole.

3.2. *Kinematics/dynamics of the structures*

3.2.1. *Entrainment*

To further elucidate the local flow field in a frame of reference relative to the high-enstrophy small-scale structures, we consider them as being embedded

Contribution	Experiment		DNS	
	Structures	Volume	Structures	Volume
$\dfrac{\langle\sigma_1\cos^2\theta_1\rangle}{\sqrt{\sum\langle\sigma_i\cos^2\theta_i\rangle^2}}$	0.700	0.823	0.639	0.818
$\dfrac{\langle\sigma_2\cos^2\theta_2\rangle}{\sqrt{\sum\langle\sigma_i\cos^2\theta_i\rangle^2}}$	0.677	0.355	0.732	0.352
$\dfrac{\langle\sigma_3\cos^2\theta_3\rangle}{\sqrt{\sum\langle\sigma_i\cos^2\theta_i\rangle^2}}$	−0.226	−0.443	−0.235	−0.455

Table 1. Enstrophy production (vortex stretching) contribution shares due to alignment between the vorticity vector and the rate of strain eigenvectors and the corresponding eigenvalues for the experiment and DNS.

in a predominantly quiescent flow and their detected boundaries are treated with the methodological approach applied at the TNTI. We then calculate the entrainment/detrainment velocity and the rate of enstrophy production, diffusion and dissipation across the boundaries using (2.3) and (2.2). Analysing the interaction of structures in this way will reveal how they interact with the flow in terms of mass and momentum exchange and permit direct comparison with the Burgers vortex model.

Figure 9 shows the p.d.f.s of the entrainment velocity, v_n, vortex stretching, enstrophy diffusion and dissipation terms from (2.3) for the experiment (solid lines) and DNS (dashed lines). The values are normalized by the corresponding Kolmogorov velocity scale, $u_\eta = (\nu\langle\epsilon\rangle)^{1/4}$. With the exception of enstrophy dissipation, the peaks in the p.d.f. of the various terms are all slightly negative and exhibit non-Gaussian distributions. Overall good agreement between the DNS and the experiments is observed. The p.d.f. of the entrainment velocity v_n is similar to those observed in other flows at the TNTI (Holzner & Lüthi 2011; Wolf *et al.* 2012; Mistry *et al.* 2019) which shows a fine balance in favour of entrainment over detrainment noting that the tail on the left-hand side, which corresponds to entrainment, has higher values compared with the right-hand side which corresponds to detrainment. This demonstrates that, on average, the structures are radially entraining fluid from the quiescent surroundings as $\langle v_n\rangle < 0$. The contribution of vortex stretching to the entrainment velocity, $-2\omega_i\omega_j s_{ij}/|\boldsymbol{\nabla\omega^2}|$, is shown by the red line and exhibits higher probabilities than the entrainment velocity which is balanced by the contribution of viscous diffusion of enstrophy. Viscous diffusion peaks slightly on the negative side but shows higher probabilities in the tails when $v_n/u_\eta > 0$. On the right-hand side, the tails of the viscous effects of enstrophy dissipation and diffusion have higher p.d.f. values compared with vortex stretching. This provides direct evidence that vortex stretching is a dominant mechanism that drives entrainment ($v_n < 0$) whereas the viscous effects of enstrophy diffusion and dissipation contribute predominantly to detrainment ($v_n > 0$). This is in contrast with the behaviour of viscous and inviscid budgets across the TNTI of free shear flow where the viscous effect is always dominant in both entrainment and detrainment regions and is an indication of viscous/laminar superlayer at the turbulence boundary (Holzner & Lüthi 2011). However, the behaviour of the vortex boundary is similar to that of the turbulent–turbulent interface where vortex stretching is dominant and viscous superlayer is not present (Kankanwadi & Buxton 2022).

The picture that emerges is that the overall behaviour of the small-scale structures appears similar to that of stable Burgers vortices where the radial entrainment of

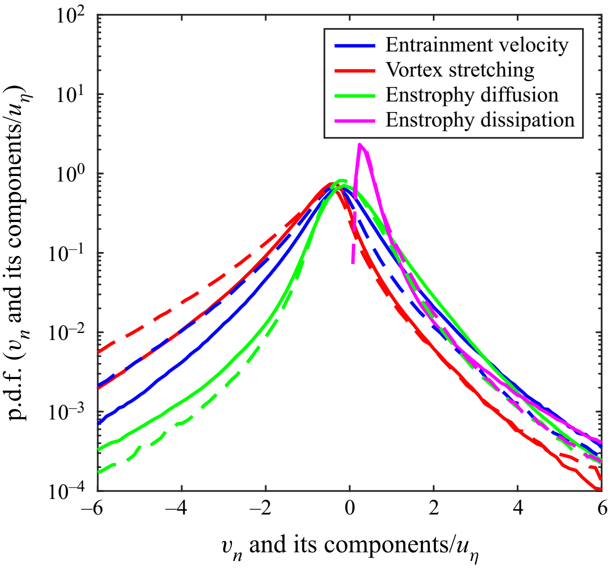

Figure 9. The p.d.f.s of normalized entrainment velocity, v_n/u_η, at the boundary of the structures and its components (budgets: vortex stretching, $-2\omega_i\omega_j s_{ij}/(|\nabla \boldsymbol{\omega}^2|u_\eta)$; diffusion, $-\nu(\partial^2\omega^2/\partial x_j \partial x_j)/(|\nabla \boldsymbol{\omega}^2|u_\eta)$; dissipation, $2\nu(\partial\omega_i/\partial x_j)(\partial\omega_i/\partial x_j)/(|\nabla \boldsymbol{\omega}^2|u_\eta)$) for the experiment (solid lines) and DNS (dashed lines).

surrounding low-enstrophy fluid into the vortex is the result of a competition between vortex stretching, enstrophy diffusion and enstrophy dissipation. In a stable Burgers vortex the radial entrainment velocity is $u_r = -(\alpha/2)r$, where α is a positive constant (the strain rate) and hence $u_r < 0$ (Davidson 2015) and is consistent with the average picture of the detected vortex structures observed in the experimental and DNS data sets even though the local statistics are not in full agreement with the Burgers vortex model.

We examine the local dependence of the entrainment velocity on the radius (size) of the structures by plotting the j.p.d.f.s of the normalized entrainment velocity, v_n/u_η, and the normalized radius, R/η, in figure 10. The experimental data are presented with solid lines and DNS with dashed lines as previously. The drop-shaped j.p.d.f.s are very slightly skewed towards the region of negative entrainment velocity which means that over all the sizes of R/η plotted, the structures are on average radially entraining fluid from their surroundings. The peak of the correlation between the magnitude of entrainment velocity and radius occurs when $2 \lesssim R/\eta \lesssim 6$. This shows that the entrainment/detrainment of the structures is most active when the local radius is between approximately 2η and 6η.

Next, we investigate how entrainment varies both radially and along the axial direction of the structures. In figure 11(a), we plot the average entrainment velocity conditioned on the radial and axial directions of the vortices, $(v_n/u_\eta)(r/R, l/\eta)$. Since the detected vortex structures are nested families of IVD iso-surfaces, the iso surfaces of IVD correspond to iso-surfaces of enstrophy as discussed in § 2.3. Thus, the entrainment velocity and the budgets in (2.3) can be calculated anywhere inside and in the vicinity of structures. The result can be interpreted as the radial velocity relative to the local iso-enstrophy surface when away from the boundary of the vortex, or alternatively, the entrainment velocity that holds for varying choice of enstrophy iso-surface boundaries. Since the length of the vortices is cropped by the finite size of the observation volume in the experiment, we here focus on DNS data only. The maximum entrainment velocity is on average located in the central region of the vortices extending $\approx \pm 5\eta$ along the vortex axis ($r/R = 0$)

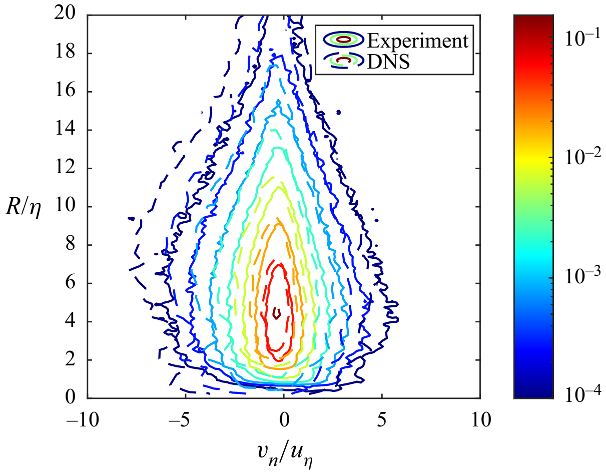

Figure 10. Joint p.d.f.s of normalized entrainment velocity, v_n/u_η, and normalized radius of the structures, R/η, for the experiment (solid contours) and DNS (dashed contours).

and radially outwards to about half the radius. Moving along the axis of the vortex along $r/R = 0$ the v_n/u_η decays towards both ends of the vortices to near zero values. Since the vortices occupy a finite volume of the domain, statistical stationarity would require that on average there is no gain or loss of mass for the average structure. Given the net radial entrainment observed here, one would expect a net detrainment across the boundary at the tips of the structure. The axial decrease of v_n is consistent with that argument even though we do not observe a change of sign over the considered length, presumably because our detection method crops the structure before the tip which is a singular point where the cross sectional area approaches zero.

To investigate the spatial pattern of the different contributions to entrainment, we consider the terms (budgets) on the right-hand side of (2.3) conditioned on the radial and axial directions plotted in figure 11(*b–d*) for the DNS data set. Contour of vortex stretching shows a strong contribution in favour of entrainment with maximum negative values concentrated along the vortex axis decaying to very low levels near the vortex boundary. The data show a slight peak centred at $l/\eta = 0$ extending $\approx \pm 5l/\eta$ before decaying along the vortex length. The effects of enstrophy diffusion, shown in figure 11(*c*), exhibit similar behaviour but in favour of detrainment. Figure 11(*d*) shows comparatively low, but slightly positive uniform values of enstrophy dissipation inside the vortices in favour of detrainment. Greater values of dissipation are found outside the vortices. The contribution of dissipation to the overall balance of the entrainment/detrainment velocity is small.

The Burgers vortex is a one-dimensional model and cannot capture any heterogeneity along the vortex axis by definition. However, it can still be a good model for the radial dynamics. To investigate the similarities and differences of the vortex filaments with Burgers vortices in more detail, we now compare statistical quantities from the experimental and DNS data with the quantities predicted by the Burgers vortex model (Jiménez *et al.* 1993; Jiménez & Wray 1998; da Silva *et al.* 2011; Watanabe *et al.* 2017; Ghira *et al.* 2022). Beginning with the radii of the filaments, p.d.f.s of the ratio of measured radius of the structures from the experiments and DNS to the equivalent Burgers radius, R/R_B, are plotted in figure 12. Here R_B was calculated for the structures based on the stretching values along the centre lines, $\alpha_0 = \omega_i\omega_j s_{ij}/\omega_0^2$ at $r = 0$, using the formula

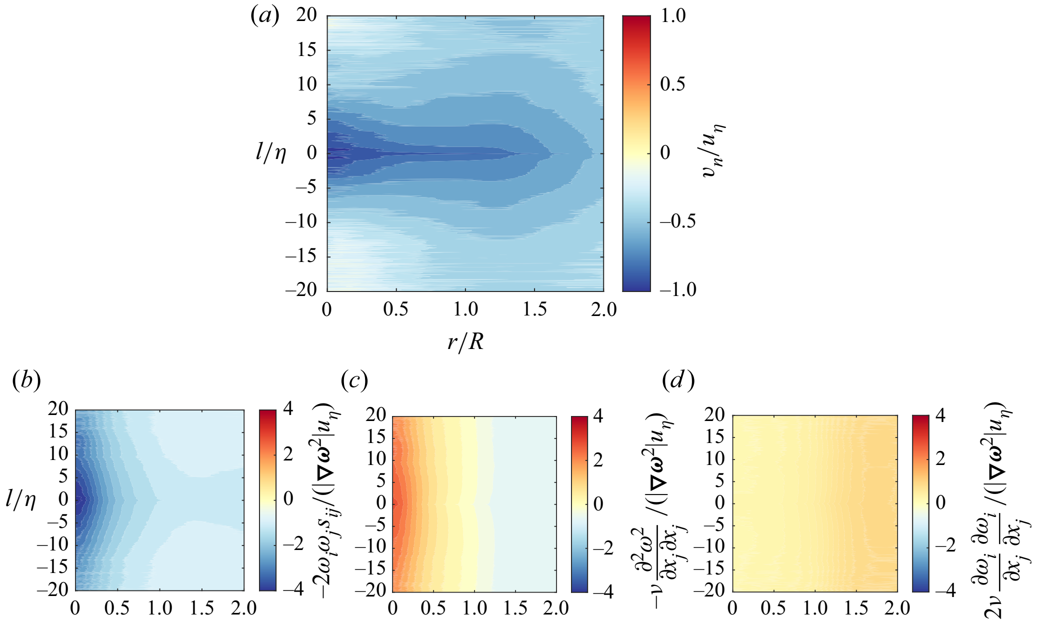

Figure 11. Filled contours of average normalized entrainment velocity and its budgets (terms in (2.3)) in radial (r/R) and axial (l/η) directions of the structures for the DNS data set: (*a*) entrainment velocity, (*b*) vortex stretching, (*c*) diffusion and (*d*) dissipation.

$R_B = \sqrt{4\nu/\alpha_0}$ in (2.5). The overall trends of the p.d.f.s from the experiment and DNS are in reasonably good agreement. The main differences are that the experimental data are more skewed on the left-hand side of $R/R_B = 1$ with a slightly different slope for vortices with larger radii. The maximum probabilities occur between $R/R_B \approx 0.65$ and 0.75 for both the experiments and DNS as well as small differences in the mean $\langle R/R_B \rangle = 0.95$ and 1.1. These data show that, on average, the radius of the structures and the equivalent Burgers vortex radius obtained from the experimental data are in good agreement with numerical studies, such as the DNS of Jiménez & Wray (1998) and da Silva *et al.* (2011), but there are some variations in the local statistics. In the DNS studies of Jiménez *et al.* (1993), Jiménez & Wray (1998), da Silva *et al.* (2011) and Ghira *et al.* (2022), the peak value of p.d.f.(R/R_B) occurs at $R/R_B = 1$, slightly different from figure 12 in the present study. We believe this slight difference is due to the vortex detection method being used. In the above-mentioned studies, a thresholding detection method based on exponential decay of enstrophy in the radial direction (following the Burgers vortex model) was used. Here, no assumption is made about the form of the enstrophy decay.

Another feature of the Burgers vortex model is that the radial enstrophy distribution in the vortex follows an exponential profile from the centre line. To test the robustness of this assumption, enstrophy profiles as well as profiles of the mean deviation of the structures for the experimental and the DNS data sets are plotted for comparison. The mean radial profiles of the normalized enstrophy of the vortices and the equivalent Burgers vortex model are plotted in figure 13(*a*) for the experiments and DNS with black lines as well as the model values for the equivalent Burgers vortices in grey line. Good agreement between the model, experiments and DNS is found near the vortex core, $r/R = 0$. Moving away from the vortex core, both the experiments and DNS depart from the Burgers model which

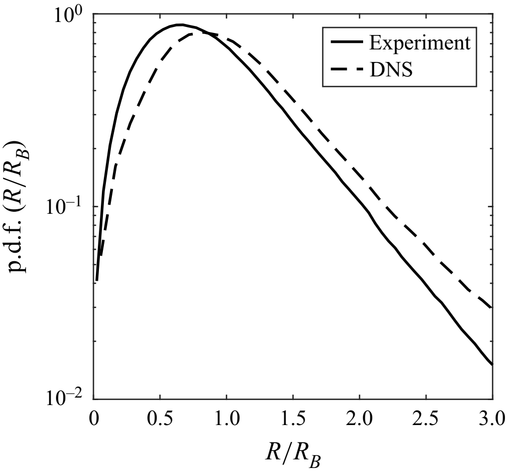

Figure 12. The p.d.f.s of the ratio between radius of the structures and the equivalent Burgers vortex radius for the experiment (solid line) and DNS (dashed line).

predicts a faster decay with r. Although the trends for the experiments and DNS are similar, it is difficult to untangle whether the Burgers model overestimates the decay of enstrophy towards the boundary of the structures or whether the resolution of the experiments and DNS underestimates the decay in enstrophy. Figure 13(*b*) plots the deviation of the experiments and DNS from the Burgers model by calculating

$$\delta\left(\frac{r}{R}\right) = \left\langle \frac{\omega^2\left(\frac{r}{R}\right) - \omega_B^2\left(\frac{r}{R_B}\right)}{\omega_0^2} \right\rangle \times 100\,(\%) \tag{3.1}$$

for the experimental and DNS data sets within the range of $0 \leq r/R \leq 2$. The curves show the mean radial profile of δ. As can be seen from this figure, the local agreement is poor away from the vortex core in both cases which is postulated to be at least partly related to a lack of spatial resolution.

We next compare the ratio of the measured entrainment velocity with the entrainment velocity predicted from the Burgers vortex model. The equivalent entrainment velocity is calculated using the radial velocity formula at the boundary, $v_{n,B} = u_{r=R_B} = -(\alpha_0/2)R_B$ (Davidson 2015). Figure 14 plots the p.d.f.s of the entrainment velocity ratio for the experiment (solid line) and DNS (dashed line). For the experiment, the peak of the p.d.f. occurs at $v_n/v_{n,B} \approx 0.8$ and the mean value is $\langle v_n/v_{n,B}\rangle = 0.79$, whereas for DNS the peak is at $v_n/v_{n,B} \approx 0.9$ and the mean value is $\langle v_n/v_{n,B}\rangle = 1.1$. Overall, the fact that $\langle v_n/v_{n,B}\rangle \approx 1$ shows that the Burgers model reasonably captures the entrainment velocity. Similar to the case of the p.d.f.s of radii (figure 12), the distributions are non-Gaussian with the positive tails having larger values away from $v_n/v_{n,B} = 1$.

3.2.2. *Enstrophy balance*

The different terms (budgets) of the enstrophy transport equation (2.2) are now investigated along the radial and axial directions of the structures in a similar manner to that in § 3.2.1. To construct a picture of how enstrophy is distributed in a vortex, figure 15 plots filled contours of the average enstrophy profile conditioned on the radial and axial directions for the DNS data only and not the experiment as the length of the vortices is cropped

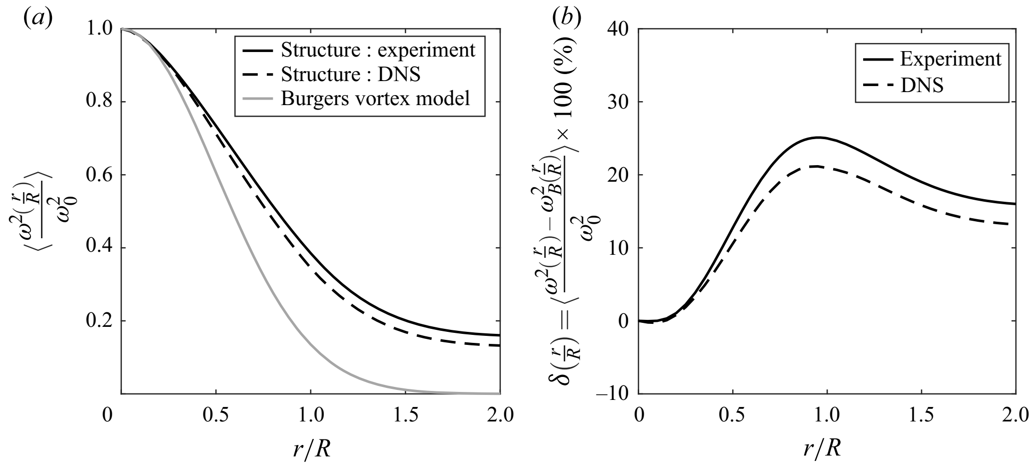

Figure 13. Enstrophy profiles. (*a*) The mean radial profile of the normalized enstrophy of the vortices and the equivalent Burgers vortex model for the experiments and DNS and (*b*) the deviation of the experiments and DNS from the Burgers model.

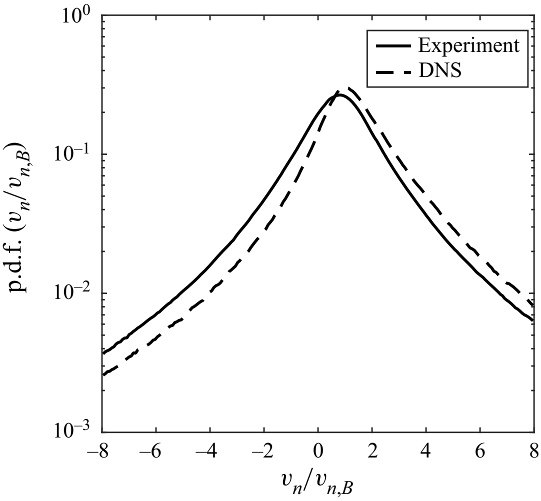

Figure 14. The p.d.f.s of the ratio between the entrainment velocity of the structures and the equivalent entrainment velocity from the Burgers vortex model for the experiment (solid line) and DNS (dashed line).

by the finite size of the observation volume in the experiment. On average, the peak of enstrophy occurs at the centre of the vortex, i.e. $(r/R, l/\eta) = (0, 0)$, which decays in the radial direction towards the vortex boundary and along the vortex axis but to a lesser extent.

The normalized conditional averaged radial profiles of the different terms in the enstrophy transport equation are shown in figure 16 for the experiments (solid lines), DNS (dashed lines) and the equivalent Burgers vortices (with dot markers). All cases considered show reasonably similar trends indicative of having similar governing physics. On average, at the centre of the structures, the viscous terms of diffusion with a near-negligible contribution from dissipation are balanced by inviscid vortex stretching as exhibited by the material derivative of enstrophy tending close to zero. Marching towards the boundary

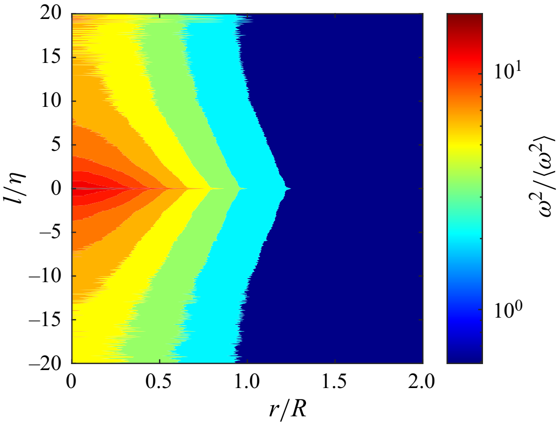

Figure 15. Filled contours of average normalized enstrophy ($\omega^2/\langle\omega^2\rangle$) in radial ($r/R$) and axial ($l/\eta$) directions of the structures for the DNS data set.

from the vortex core, the absolute values of both vortex stretching and diffusion decrease whilst the dissipation increases. The rate of decrease is greater for the diffusion term. Together this results in the total derivative of enstrophy increasing to a peak at $r/R \approx 0.7$ followed by a gentle decay towards zero. In the region $r/R_B > 1$ of the Burgers vortex model, the viscous diffusion term dominates over the inviscid vortex stretching term. This behaviour is qualitatively similar to that of viscous superlayer at TNTI. However, in contrast with the Burgers vortex model and TNTI, the inviscid vortex stretching term is still dominant over the viscous diffusion term in the $r/R_B > 1$ region of the detected vortex structures. Comparing the radial distribution of diffusion and dissipation shows that in the regions near the core, diffusion is the major contribution to the viscous effects, whereas near the vortex boundary dissipation becomes the dominant contributor.

Similar to § 3.2.1, plotting the enstrophy transport equation terms (2.2) conditionally averaged on the radial and axial directions of the structures can provide a more complete picture of the active physical phenomena inside the structures. Here we only consider the vortices from the DNS data set and not the equivalent Burgers vortices. The reason is that the Burgers vortex model by definition is infinitely long and the quantities of interest, i.e. enstrophy and the terms in the enstrophy transport equation (equations (2.5)–(2.9)), are independent of the axial distance. Figure 17 plots the terms (budgets) of the enstrophy transport equation (2.2). In the radial direction, figure 17 confirms figure 16, and in the axial direction they show the decay of all the quantities considered which is in contrast with the Burgers vortex model.

4. Conclusion

In this paper we investigated how small-scale vortex structures interact locally with the surrounding quiescent flow using a temporally and spatially resolved experimental data set of homogeneous turbulence of a von Kármán mixing flow and a DNS data set of forced isotropic turbulence. To detect the boundary of the small-scale vortex structures about which the local entrainment can be evaluated, an objective definition to identify the vortical structures introduced by Haller *et al.* (2016) was implemented on both data sets and was the first successful implementation in experimentally resolved measurements of small-scale turbulence at high Reynolds number. The average radius of the vortex

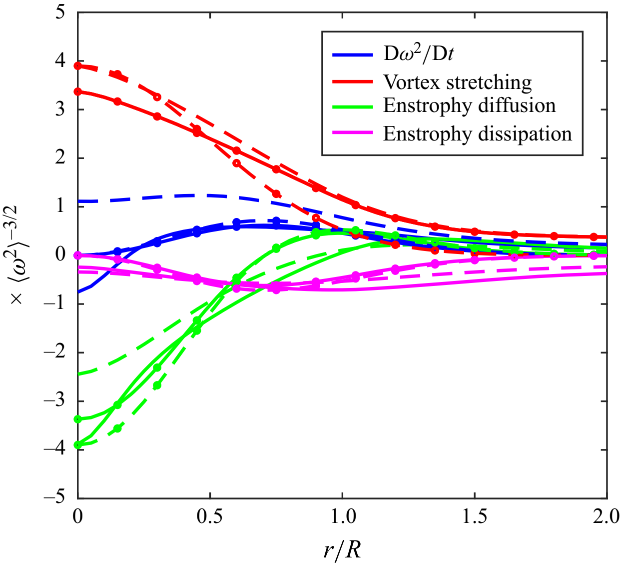

Figure 16. Normalized enstrophy transport equation terms (material derivative of enstrophy $(\mathrm{D}\omega^2/\mathrm{D}t) \times \langle\omega^2\rangle^{-3/2}$, vortex stretching $2\omega_i\omega_j s_{ij} \times \langle\omega^2\rangle^{-3/2}$, enstrophy diffusion $\nu(\partial^2\omega^2/\partial x_j \partial x_j) \times \langle\omega^2\rangle^{-3/2}$ and enstrophy dissipation $-2\nu(\partial\omega_i/\partial x_j)(\partial\omega_i/\partial x_j) \times \langle\omega^2\rangle^{-3/2}$) conditioned on the radial direction of the structures for the cases of the experiment (solid lines), equivalent Burgers vortex of the experiment (solid lines with dot markers), DNS (dashed lines) and equivalent Burgers vortex of the DNS (dashed lines with dot markers).

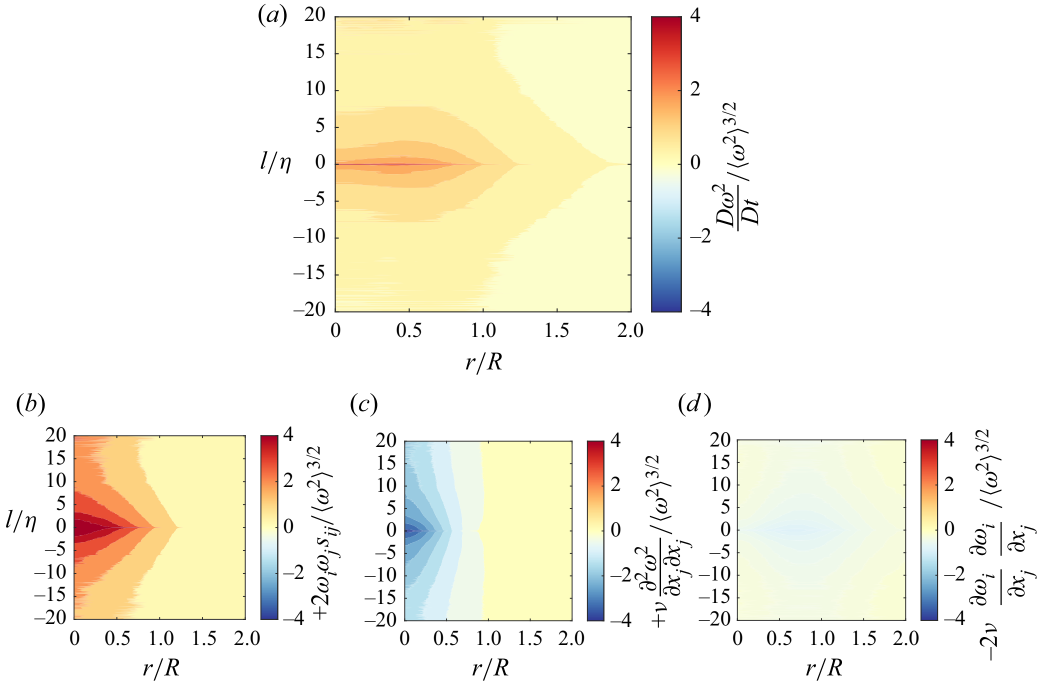

Figure 17. Filled contours of average normalized enstrophy transport budgets (terms in (2.2)) in radial (r/R) and axial (l/η) directions of the structures for the DNS data set: (*a*) material derivative of enstrophy, (*b*) vortex stretching, (*c*) diffusion and (*d*) dissipation.

structures was found to be 5.1η and that they occupied about 1.4 % of the measured flow volume on average in agreement with the reported values in the literature ($\approx 5\eta$ and ≈ 1 %). Comparing p.d.f.s of volume-averaged enstrophy and dissipation with those conditioned on the inside of the structures revealed that the latter contained higher peak values of enstrophy and dissipation but a decreased probability of low-enstrophy and low-dissipation events. These differences between the volume- and structure-averaged p.d.f.s were more pronounced for enstrophy and the enstrophy production to destruction ratio was found to be significantly higher inside the vortex structures. Volume-averaged and structure-averaged j.p.d.f.s of enstrophy and dissipation were found to scale similarly inside the vortex structures. The alignments between the vorticity vector and the rate of strain eigenvectors showed that inside the vortex structures the vorticity vectors were aligned with the intermediate eigenvector and normal to the compressive and extensional eigenvectors.

By considering the vortex structures as being embedded in a predominantly quiescent flow and conditioning on their boundary, the entrainment velocity and enstrophy budgets were determined. The p.d.f. of entrainment velocity exhibits a non-Gaussian distribution of entrainment and detrainment skewed slightly in favour of entrainment. The p.d.f. and the fine balance in favour of entrainment over detrainment is remarkably similar to the p.d.f.s of entrainment velocity observed across the TNTI reported in boundary layers and jets. The entrainment velocity was found to reach a peak near the vortex core decaying radially outwards towards the vortex boundary and along its axis. The decrease in the magnitude of the entrainment velocity was consistent with the flow being statistically stationary (the vortices cannot grow on average) and the net radial entrainment is expected to be balanced by the net detrainment at the ends of the vortices. A strong correlation between entrainment and vortex stretching was observed (inviscid effect) whereas detrainment was found to be correlated with enstrophy diffusion and dissipation events (viscous effects). This is in contrast with what is observed at the TNTI in free shear flow where the viscous effect is dominant due to the presence of the viscous/laminar superlayer. However, the behaviour of vortex boundary is similar to that of turbulent–turbulent interface where vortex stretching (inviscid effect) is dominant and viscous superlayer is no longer present. The j.p.d.f. of radius and entrainment velocity showed that entrainment/detrainment was most active when the local radii of the vortices were between 2η and 6η. A direct comparison with Burgers vortices was performed with both the experimental and the DNS data sets. The p.d.f.s of the local radius were non-Gaussian but good agreement between the experimental data, DNS and the equivalent Burgers vortex was found. Compared with the DNS and experimental data, the Burgers vortex model overestimates the rate of decay in the enstrophy profile of the vortices. Conditional budgets of the enstrophy transport equation were examined and compared with the Burgers model confirming that the competition between vortex stretching and diffusion was the dominant mechanism. It was found that marching towards the boundary both vortex stretching and diffusion gradually weakened as dissipation strengthened with all terms approaching zero just outside the vortex boundary.

Declaration of interests. The authors report no conflict of interest.

Author ORCIDs.
Farid Aligolzadeh https://orcid.org/0000-0003-2848-0555;
Markus Holzner https://orcid.org/0000-0003-2702-8612;
James R. Dawson https://orcid.org/0000-0002-3069-6948.

REFERENCES

ASHURST, W.T., KERSTEIN, A.R., KERR, R.M. & GIBSON, C.H. 1987 Alignment of vorticity and scalar gradient with strain rate in simulated Navier–Stokes turbulence. *Phys. Fluids* **30** (8), 2343–2353.

BUARIA, D., BODENSCHATZ, E. & PUMIR, A. 2020 Vortex stretching and enstrophy production in high Reynolds number turbulence. *Phys. Rev. Fluids* **5** (10), 104602.

BURGERS, J.M. 1948 A mathematical model illustrating the theory of turbulence. *Adv. Appl. Mech.* **1**, 171–199.

CADOT, O., DOUADY, S. & COUDER, Y. 1995 Characterization of the low-pressure filaments in a three-dimensional turbulent shear flow. *Phys. Fluids* **7** (3), 630–646.

DAVIDSON, P.A. 2015 *Turbulence: An Introduction for Scientists and Engineers*. Oxford University Press.

DUBIEF, Y. & DELCAYRE, F. 2000 On coherent-vortex identification in turbulence. *J. Turbul.* **1**, 011.

ELSINGA, G.E. & MARUSIC, I. 2010 Universal aspects of small-scale motions in turbulence. *J. Fluid Mech.* **662**, 514–539.

FRISCH, U. 1995 *Turbulence: The Legacy of AN Kolmogorov*. Cambridge University Press.

GANAPATHISUBRAMANI, B., LAKSHMINARASIMHAN, K. & CLEMENS, N.T. 2008 Investigation of three-dimensional structure of fine scales in a turbulent jet by using cinematographic stereoscopic particle image velocimetry. *J. Fluid Mech.* **598**, 141–175.

GHIRA, A.A., ELSINGA, G.E. & DA SILVA, C.B. 2022 Characteristics of the intense vorticity structures in isotropic turbulence at high Reynolds numbers. *Phys. Rev. Fluids* **7** (10), 104605.

HALLER, G. 2005 An objective definition of a vortex. *J. Fluid Mech.* **525**, 1–26.

HALLER, G. 2015 Lagrangian coherent structures. *Annu. Rev. Fluid Mech.* **47** (1), 137–162.

HALLER, G., HADJIGHASEM, A., FARAZMAND, M. & HUHN, F. 2016 Defining coherent vortices objectively from the vorticity. *J. Fluid Mech.* **795**, 136–173.

HOLZNER, M. & LÜTHI, B. 2011 Laminar superlayer at the turbulence boundary. *Phys. Rev. Lett.* **106** (13), 134503.

HUA, B.L. & KLEIN, P. 1998 An exact criterion for the stirring properties of nearly two-dimensional turbulence. *Physica* D **113** (1), 98–110.

HUSSAIN, A.K.M.F. 1986 Coherent structures and turbulence. *J. Fluid Mech.* **173**, 303–356.

ISHIHARA, T., GOTOH, T. & KANEDA, Y. 2009 Study of high–Reynolds number isotropic turbulence by direct numerical simulation. *Annu. Rev. Fluid Mech.* **41**, 165–180.

ISHIHARA, T., YAMAZAKI, Y. & KANEDA, Y. 2001 Statistics of small-scale structure of homogeneous isotropic turbulence: Data-base analysis of direct numerical simulation. In *IUTAM Symposium on Geometry and Statistics of Turbulence: Proceedings of the IUTAM Symposium held at the Shonan International Village Center, Hayama (Kanagawa-ken), Japan, November 1–5, 1999* (ed. T. Kambe, T. Nakano & T. Miyauchi), pp. 133–138. Springer.

JIMÉNEZ, J. & WRAY, A.A. 1998 On the characteristics of vortex filaments in isotropic turbulence. *J. Fluid Mech.* **373**, 255–285.

JIMÉNEZ, J., WRAY, A.A., SAFFMAN, P.G. & ROGALLO, R.S. 1993 The structure of intense vorticity in isotropic turbulence. *J. Fluid Mech.* **255**, 65–90.

KANG, S.-J., TANAHASHI, M. & MIYAUCHI, T. 2009 Dynamics of fine scale eddy clusters in turbulent channel flows. *J. Turbul.* **8**, N52.

KANKANWADI, K.S. & BUXTON, O.R.H. 2022 On the physical nature of the turbulent/turbulent interface. *J. Fluid Mech.* **942**, A31.

KERR, R.M. 1985 Higher-order derivative correlations and the alignment of small-scale structures in isotropic numerical turbulence. *J. Fluid Mech.* **153**, 31–58.

LAWSON, J.M. & DAWSON, J.R. 2014 A scanning PIV method for fine-scale turbulence measurements. *Exp. Fluids* **55** (12), 1–19.

LAWSON, J.M. & DAWSON, J.R. 2015 On velocity gradient dynamics and turbulent structure. *J. Fluid Mech.* **780**, 60–98.

LE DIZES, S., ROSSI, M. & MOFFATT, H.K. 1996 On the three-dimensional instability of elliptical vortex subjected to stretching. *Phys. Fluids* **8** (8), 2084–2090.

LEUNG, T., SWAMINATHAN, N. & DAVIDSON, P.A. 2012 Geometry and interaction of structures in homogeneous isotropic turbulence. *J. Fluid Mech.* **710**, 453–481.

LI, Y., PERLMAN, E., WAN, M., YANG, Y., MENEVEAU, C., BURNS, R., CHEN, S., SZALAY, A. & EYINK, G. 2008 A public turbulence database cluster and applications to study lagrangian evolution of velocity increments in turbulence. *J. Turbul.* **9**, N31.

MATHEW, J. & BASU, A.J. 2002 Some characteristics of entrainment at a cylindrical turbulence boundary. *Phys. Fluids* **14** (7), 2065–2072.

MISTRY, D., PHILIP, J. & DAWSON, J.R. 2019 Kinematics of local entrainment and detrainment in a turbulent jet. *J. Fluid Mech.* **871**, 896–924.

MISTRY, D., PHILIP, J., DAWSON, J.R. & MARUSIC, I. 2016 Entrainment at multi-scales across the turbulent/non-turbulent interface in an axisymmetric jet. *J. Fluid Mech.* **802**, 690–725.

MOFFATT, H.K., KIDA, S. & OHKITANI, K. 1994 Stretched vortices–the sinews of turbulence; large-Reynolds-number asymptotics. *J. Fluid Mech.* **259**, 241–264.

NEAMTU-HALIC, M.M., KRUG, D., HALLER, G. & HOLZNER, M. 2019 Lagrangian coherent structures and entrainment near the turbulent/non-turbulent interface of a gravity current. *J. Fluid Mech.* **877**, 824–843.

NEAMTU-HALIC, M.M., MOLLICONE, J.P., VAN REEUWIJK, M. & HOLZNER, M. 2021 Role of vortical structures for enstrophy and scalar transport in flows with and without stable stratification. *J. Turbul.* **22** (7), 393–412.

NOVARA, M. & SCARANO, F. 2013 A particle-tracking approach for accurate material derivative measurements with tomographic PIV. *Exp. Fluids* **54**, 1–12.

POPE, S.B. 2000 *Turbulent Flows*. Cambridge University Press.

SAFFMAN, P.G. 1995 *Vortex Dynamics*. Cambridge University Press.

SHE, Z.-S., JACKSON, E. & ORSZAG, S.A. 1990 Intermittent vortex structures in homogeneous isotropic turbulence. *Nature* **344** (6263), 226–228.

SIGGIA, E.D. 1981 Numerical study of small-scale intermittency in three-dimensional turbulence. *J. Fluid Mech.* **107**, 375–406.

DA SILVA, C.B., DOS REIS, R.J.N. & PEREIRA, J.C.F. 2011 The intense vorticity structures near the turbulent/non-turbulent interface in a jet. *J. Fluid Mech.* **685**, 165–190.

TAVEIRA, R.R. & DA SILVA, C.B. 2014 Characteristics of the viscous superlayer in shear free turbulence and in planar turbulent jets. *Phys. Fluids* **26** (2), 021702.

TAYLOR, G.I. 1938 Production and dissipation of vorticity in a turbulent fluid. *Proc. R. Soc. Lond.* A **164** (916), 15–23.

TSINOBER, A. 2009 *An Informal Conceptual Introduction to Turbulence*, vol. 483. Springer.

VINCENT, A. & MENEGUZZI, M. 1991 The spatial structure and statistical properties of homogeneous turbulence. *J. Fluid Mech.* **225**, 1–20.

WATANABE, T., JAULINO, R., TAVEIRA, R.R., DA SILVA, C.B., NAGATA, K. & SAKAI, Y. 2017 Role of an isolated eddy near the turbulent/non-turbulent interface layer. *Phys. Rev. Fluids* **2** (9), 094607.

WESTERWEEL, J., FUKUSHIMA, C., PEDERSEN, J.M. & HUNT, J.C.R. 2005 Mechanics of the turbulent-nonturbulent interface of a jet. *Phys. Rev. Lett.* **95** (17), 174501.

WOLF, M., LÜTHI, B., HOLZNER, M., KRUG, D., KINZELBACH, W. & TSINOBER, A. 2012 Investigations on the local entrainment velocity in a turbulent jet. *Phys. Fluids* **24** (10), 105110.

YEUNG, P.K., DONZIS, D.A. & SREENIVASAN, K.R. 2012 Dissipation, enstrophy and pressure statistics in turbulence simulations at high Reynolds numbers. *J. Fluid Mech.* **700**, 5–15.

Article 2

Experiments of turbulent decay in a von Kármán swirling flow at high Reynolds number

---

Farid Aligolzadeh, Pawel Baj, and James R. Dawson

Under consideration for publication in Journal of Fluid Mechanics

This paper is submitted for publication and is therefore not included.

Article 3

Experimental investigation of large-scale harmonic motions in a von Kármán swirling flow

Farid Aligolzadeh, Pawel Baj, and James R. Dawson

Under consideration for publication in Journal of Fluid Mechanics

This paper is submitted for publication and is therefore not included.

Appendix A

Study of fine-scale vortical structures in a von Kármán mixing flow

Farid Aligolzadeh, Markus Holzner and James R. Dawson

Proceeding of the 12th *International Symposium on Turbulence and Shear Flow Phenomena (TSFP12), July 19-22, 2022, Osaka, Japan (Online)*

STUDY OF FINE-SCALE VORTICAL STRUCTURES IN A VON KÁRMÁN MIXING FLOW

Farid Aligolzadeh
Department of Energy and Process Engineering
Norwegian University of Science and Technology
NO-7491, Trondheim, Norway
farid.aligolzadeh@ntnu.no

Markus Holzner
Swiss Federal Institute of Forest,
Snow and Landscape Research WSL
8903 Birmensdorf,Switzerland
Swiss Federal Institute of Aquatic Science
and Technology Eawag
8600 Dübendorf,Switzerland
holzner@ifu.baug.ethz.ch

James R. Dawson
Department of Energy and Process Engineering
Norwegian University of Science and Technology
NO-7491, Trondheim, Norway
james.r.dawson@ntnu.no

ABSTRACT

Intense small-scale vortical structures also known as ‘filaments´ or ‘worms’ have been studied in a wide range of turbulent flows, mostly using DNS. In the present study, we investigate vorticity dynamics of vortex filaments at the dissipation scale in a fully resolved three-dimensional experimental data set of a turbulent mixing flow measured at the center of a large von Kármán mixing tank at a $Re_\lambda = 179$. To avoid arbitrariness inherent to threshold-dependent detection criteria and dependence of the results on the observer, an objective vortex detection method proposed by Haller *et al.* (2016) is implemented. One thousand instantaneous 3D velocity fields are studied. These fields were measured at random times with a spatial resolution of 1η, where η is the Kolmogorov length scale. About 12500 structures were detected having an average radius of 5.1η, which is similar to previous findings on vortex filaments in HIT and turbulent jets and channels. Local features related to the structures and global features of the flow were investigated and compared. Structures are characterized by high vorticity and low strain and the vorticity vector is predominantly aligned with the intermediate strain eigenvector that has a positive eigenvalue on average. The vorticity vector is predominantly oriented normally to the compressive and extensional strain eigenvectors suggesting that the structures are quasi one-dimensional and shows that enstrophy production inside the structures results from vortex stretching. We further investigate the mechanisms that sustain the vortical structures by treating them as turbulent structures embedded in a less turbulent ambient flow, analogous to a turbulent flow separated by a turbulent/nonturbulent interface from its quiescent surroundings, and we analyze the entrainment/detrainment across their boundaries. This analysis shows that the structures are entraining ambient fluid on average in radial direction and that this entrainment is a result of the competing effects of non-viscous and viscous phenomena consistent with Burgers’ vortex model.

Introduction/Motivation

In turbulent flows, vortical structures are defined as regions of concentrated enstrophy with a life time larger than the characteristic time scale of the flow (Dubief & Delcayre, 2000). Intense vortical structures (IVSs) at the dissipation scale, often called *worms* or *filaments*, have shown universal features among a variety of different turbulent flows such as homogeneous isotropic turbulence (Jiménez *et al.*, 1993; Jiménez & Wray, 1998), jets (Ganapathisubramani *et al.*, 2008; da Silva *et al.*, 2011), channel flows (Kang *et al.*, 2009), stratified flows (Neamtu-Halic *et al.*, 2021). These studies have shown that worms or vortex filaments have a radius of about 5η, where $\eta = (\frac{\nu^3}{\varepsilon})^{1/4}$ is the Kolmogorov length scale. In the DNS study of Jiménez *et al.* (1993) it was shown that stretching, $\alpha = \omega_i\omega_j s_{ij}/\omega^2$, is relatively low in small-scale vortices which indicates lack of self-amplification. The lack of self-amplification means that the vortices are passive and decoupled from the straining field of the flow. The worms are sustained by the strain field of the flow but the strain field is not affected by the presence of the worms. So, the worms are the consequence of turbulence dynamics and not important in evolution of the dynamics. For larger size vortices the strain field and the vortices show a two-way interaction with each other. The strain field is modified by the presence of the large scale vortices and the modified strain field modifies back the vortices. So on the contrary to small scale vortices, the large scale vortices are dynamically important in evolution of turbulence (Tsinober, 2009). Despite the many efforts to understand the importance and interactions of vortical structures with the surrounding flow, our understanding is still incomplete. In particular, the way vortical structures exchange mass, momentum and vorticity with the surrounding fluid has remained obscure. We show that fine-scale vortical structures are by no means passive in the sense of exchange, i.e. the interact with the background flow by entraining (detraining) mass radially (axially) and are thus not frozen to the flow or passively advected.

In addition to the inherent difficulty in obtaining fully resolved volumetric time-resolved measurements, there is the additional challenge of robust identification of high enstrophy structures. The intense vortical structures are usually detected by using a threshold on the norm of the vorticity field or the intensity of vorticity relative to the strain field, which are not objective detection methods. That is, besides the dependence on a user-dependent threshold, the results also depend on the observer, i.e. a change of reference system will yield different structures. In this study, we use a recent method proposed by Haller *et al.* (2016) based on the *vorticity deviation* to objectively detect the structures in our experimental data set. The method isolates a coherent fluid volume, in which fluid elements complete equal bulk material rotation relative to the mean rotation. The resulting coherent structures do not change with reference system and are truly objective. Recently, the method has been successfully applied to 3D turbulence (Neamtu-Halic *et al.*, 2019). However, it has not yet been used in a more fundamental HIT set up with a moderately large Reynolds number forcing exhibiting a broad range of vortex sizes.
Our aim here is to study the interaction of the worms with the surrounding flow based on an objective detection method that provides the boundaries of the structures and allows quantifying the exchange of mass, momentum and vorticity across them.

Description of the experimental data set

The experimental data set that is analyzed in this study is from the scanning particle image velocimetry (PIV) measurement of homogeneous turbulent flow between a pair of counter-rotating impellers in a large von Kármán mixing tank facility (Lawson & Dawson, 2014, 2015). A two-dimensional sketch of the facility with its dimensions and the theoretical flow pattern inside the tank is shown in figure 1. The facility is a dodecagonal tank made of Perspex with $2m$ height and $2m$ width. The diameter of the impellers is $1.6m$ and the vertical distance between the two impellers is about $1.25m$. The axisymmetric shear generated by the revolution of the impellers induces a secondary flow pattern because of the centrifugal pumping effect. The superposition of the primary flow pattern (axisymmetric shear) and the secondary flow pattern (centrifugal pumping) makes homogeneous turbulence at the center of the tank with almost zero mean velocity and high level of turbulent fluctuations. The Reynolds number of the flow based on the impeller radius $Re_{R_I} = \Omega_I R_I^2/\nu$ is $23,000$ where Ω_I is the rotational speed of the impellers, R_I is the radius of the impellers, and ν is the kinematic viscosity of the fluid. The Reynolds number based on Taylor micro-scale of the flow is $R_\lambda = 179$ and the Kolmogorov length scale is $\eta = 0.926mm$. The spatial resolution of the data set is about 1η. The non-dimensional volume of the flow is $L_x/\eta \times L_y/\eta \times L_z/\eta = 135 \times 134 \times 25.4$. In total, the data set consists of 1003 statistically independent volumes with long and random separation times between consecutive acquisitions. The detailed description of the volumetric scanning-PIV measurement technique that is used to achieve the velocity fields can be found in Lawson & Dawson (2014).

Objective Eulerian Coherent Structure definition and the detection method

To detect the fine-scale vortical structures objectively in the flow field the definition of Objective Eulerian Coherent Structure (OECS) proposed by Haller *et al.* (2016) has been implemented. The definition of OECS is based on Instantaneous Vorticity Deviation (IVD) scalar field.

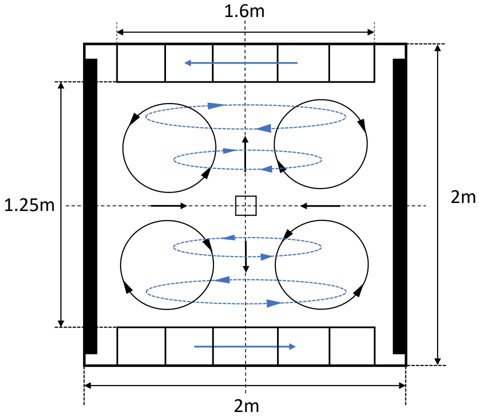

Figure 1. Schematic of the big von Kármán mixing flow facility.

$$IVD(x,t) = |\omega(x,t) - \overline{\omega}(t)| \tag{1}$$

where $\omega = \nabla \times u$ is the vorticity vector and $\overline{\omega}$ is the spatially averaged vorticity vector at each time step. OECS is defined as a nested family of level sufaces of IVD. The value of IVD does not increase when marching outwards from the center. The center has the maximum value of IVD and the boundary is defined as the outermost convex level surface. This definition of vortical structure is observer-independent and ensures instantaneous coherence of the rate of material bulk rotation relative to the mean background rotation (Haller *et al.*, 2016). An algorithm based on the presented definition has been developed and implemented to detect the three dimensional vortical structures. The algorithm is explained in details in Neamtu-Halic *et al.* (2019).

Burgers' vortex model

Since some features of the small-scale vortical structures are compared to the Burgers' vortex model, a short description of it is provided here. The Burgers' vortex model is an exact solution of incompressible Navier-Stokes equation by assuming that the vorticity field is unidirectional. It means that the vorticity field is either one dimensional or both the vorticity and strain fields are axisymmetric (Saffman, 1995). Burgers' vortices are stable as their radii do not change. Vorticity is produced by the inviscid phenomenon of vortex stretching ($\omega \cdot \nabla u$) inside the vortex and is diffused outward by the viscous phenomenon of vorticity diffusion ($\nu \nabla^2 \omega$). The competing effects of these phenomena lead to entrainment of fluid in radial direction into the vortex and detrainment of fluid along the axial direction to conserve rotational energy and mass (figure 2). Since an exact solution exists for the flow of Burgers' vortex, all the parameters related to the velocity field and velocity gradient tensor can be calculated analytically.

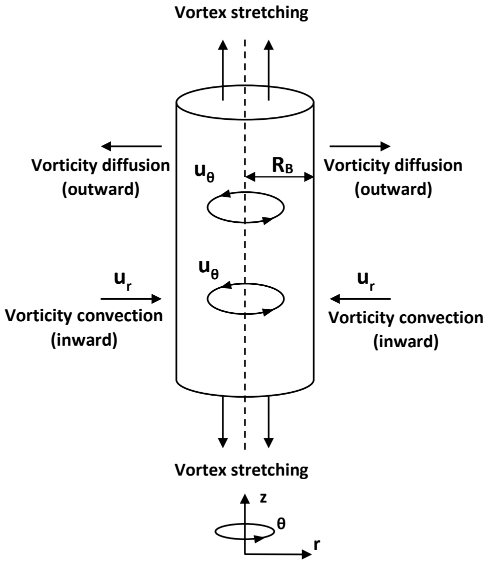

Figure 2. Burgers' vortex model.

RESULTS

In figure 3 the intense vortical structures in a snapshot of the experimental data set are shown. The black curved lines show the center of the structures and the pink surfaces show the boundary of each structure. In total, about 12500 structures have been detected over the 1003 snapshots of the data set. The average radius of the structures is 5.1η (figure 4) and were found to occupy 1.4% of the measurement volume which is in agreement with the DNS study of Jiménez *et al.* (1993).

The J-PDFs of enstrophy ($\omega^2 = \omega.\omega$ where ω is the vorticity vector) and dissipation ($\varepsilon = 2\nu s_{ij}s_{ij}$ where $s_{ij} = \frac{1}{2}(\frac{\partial u_i}{\partial x_j} + \frac{\partial u_j}{\partial x_i})$ is the rate of strain tensor) are calculated for the whole volume of flow (figure 5) and within the structures (figure 6), separately. By comparing these J-PDFs one can see a shift towards the high-vorticity and low-strain quadrant for the points within the structures. Also, a noticeable preference can be seen for the J-PDF within the structures to get aligned with the diagonal line of the enstrophy-dissipation figure. This preference shows that the extreme events of enstrophy and dissipation scale together inside the structures.

Further insight can be gained by considering the alignment between the vorticity vector $\omega = (\omega_1, \omega_2, \omega_3)$ and the rate-of-strain eigenvectors $e = (e_1, e_2, e_3)$, where $\sigma_1 \geq \sigma_2 \geq \sigma_3$ are the corresponding eigenvalues, as it affects the vortex stretching phenomenon (production/destruction of enstrophy, $\omega_i\omega_j s_{ij}$) (Tsinober, 2009). For incompressible flows, from the continuity equation ($\frac{\partial u_i}{\partial x_i} = 0$) it can be concluded that $\sigma_1 + \sigma_2 + \sigma_3 = 0$. This means than $\sigma_1 > 0$ and $\sigma_3 < 0$ everywhere in a flow field and that the value of σ_2 can be either positive or negative depending on the value that the sum of σ_1 and σ_3 has ($\sigma_2 = -(\sigma_1 + \sigma_3)$). The alignments, $\cos(\theta_i) = e_i \cdot \frac{\omega}{|\omega|}$, are calculated for the whole volume of the flow and within the structures and shown in figure 7. For the case of the whole volume it can be seen that the vorticity vector and the intermediate eigenvector are well-aligned with each other. The alignment between the vorticity vector and the compressive eigenvector was found and shows that these two vectors are mostly perpendicular to each other. However, the PDF of the alignment between the vorticity vector and the extensional eigenvector showed no preferential alignment. The preferential alignment between the vorticity and the intermediate strain eigenvector seems to be a universal feature of turbulent flows (Elsinga & Marusic, 2010). On the other hand, for the case of inside the structures it can be seen that the vorticity vector is also aligned with the intermediate eigenvector but it is normal to both extensional and compressive eigenvectors. So, one can interpret these structures as quasi 1-D with weak curvature because the vorticity vectors inside them have a strong preference to be aligned with the intermediate eigenvector and to be normal to the rest of the eigenvectors (Tsinober, 2009). As it was discussed earlier, the intermediate eigenvalue σ_2 can take either positive or negative values. For the case of the structures, since the vorticity vector has a strong preference to be only aligned with the intermediate eigenvalue the sign that σ_2 takes determines if the dominant topological phenomenon is vortex stretching ($\omega_i\omega_j s_{ij} > 0$) or vortex compression ($\omega_i\omega_j s_{ij} < 0$). Figure 8 shows PDFs of the three eigenvalues of the rate of strain tensor for both the cases of whole volume and inside the structures. The PDFs of the eigenvalues for the case of inside the structures have wider tails compared to the whole volume of flow. This means that these structures are intense realization of vortex stretching/compression in the flow field. As it is expected the value of σ_1 is only positive and the value of σ_3 is only negative. For σ_2 it can be seen that both negative and positive values are probable but on average it is positive for the both cases of whole volume and inside the structures ($\langle \frac{\sigma_2}{\langle \omega^2 \rangle^{0.5}} \rangle > 0$). It can be concluded that these structures are stretched on average by the strain field of the flow.

Since these intense vortex filaments tend to be embedded in a more quiescent (i.e. mostly characterized by rather weak enstrophy) flow, we can treat the boundary of the vortex filaments as an internal interface (Eisma *et al.*, 2015; Ishihara *et al.*, 2013), analogous to the turbulent/non-turbulent interface of free shear flows and evaluate whether they entrain and/or detrain flow. To investigate this, a formula for calculating the entrainment velocity, v_n, derived by Holzner & Lüthi (2011) is used (equation 2):

$$v_n = -\frac{2\omega_i\omega_j s_{ij}}{|\nabla\omega^2|} - \frac{\nu\frac{\partial^2\omega^2}{\partial x_j \partial x_j}}{|\nabla\omega^2|} + \frac{2\nu\frac{\partial\omega_i}{\partial x_j}\frac{\partial\omega_i}{\partial x_j}}{|\nabla\omega^2|} \qquad (2)$$

Here the entrainment velocity, v_n, is defined as $v_n n = u^s - u$ where u^s is the velocity of an isosurface element, u is the flow velocity at that isosurface, and $n = \frac{\nabla\omega^2}{|\nabla\omega^2|}$ is the normal vector to the isosurface. According to this definition, when $v_n \leq 0$ fluid elements at the isosurface are entrained into the structure and when $v_n > 0$ fluid elements are detrained out of the structure (Mistry *et al.*, 2019). Figure 9 shows the entrainment velocity and its components in equation 2 evaluated on the boundary of the structures. The entrainment velocity is negative on average which means that the structures are entraining ambient fluid on average. To conserve mass the same amount of fluid needs to be detrained axially in order to preserve the total volume of the vortices. Furthermore, by comparing the different terms in the entrainment velocity

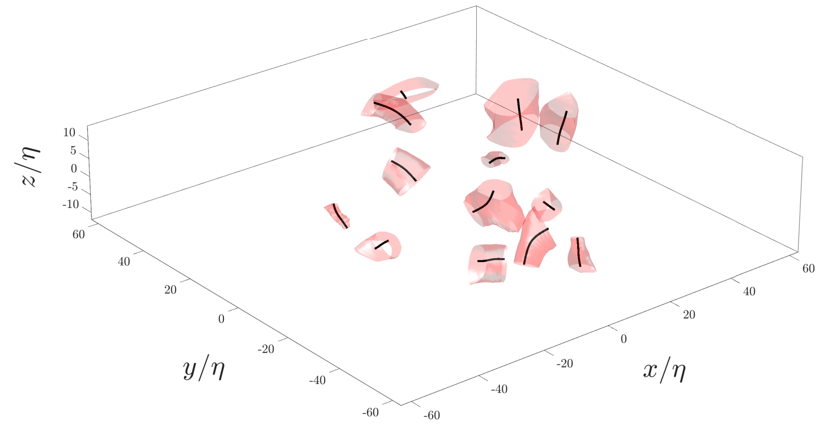

Figure 3. Example of OECSs in a snapshot of the experimental data set. Dimensions are normalized by the Kolmogorov length scale.

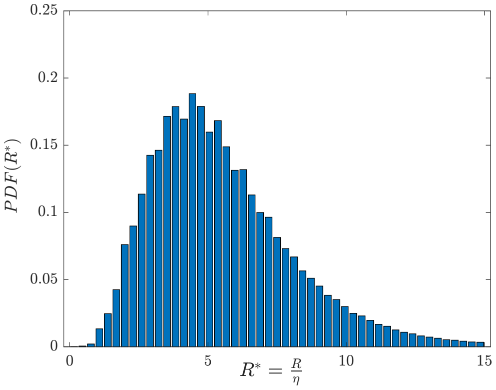

Figure 4. PDF of normalized radius of the structures.

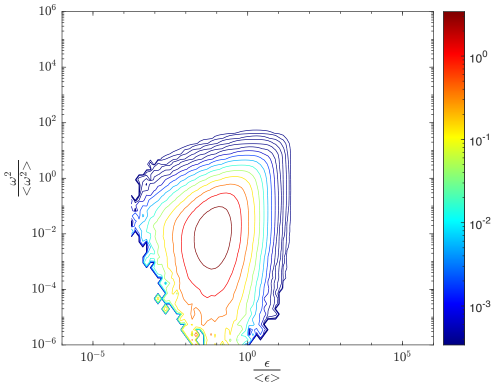

Figure 5. J-PDF of normalized enstrophy and dissipation for the whole volume.

equation we can see that the average entrainment results from a competition between inviscid and viscous effects. Figure 9 shows that local entrainment ($\frac{v_n}{u_\eta} \leq 0$) happens where local vortex stretching is greater than vorticity diffusion. On the other hand, detrainment ($\frac{v_n}{u_\eta} > 0$) occurs when the summation of local effects of vorticity diffusion and dissipation are greater than the local vortex stretching. This behaviour is consistent with a stable Burgers' vortex model where the ambient fluid is entrained to the vortex from the boundary in radial direction, $u_r = -\frac{\alpha}{2}r < 0$, and that the vortex remains stable because of the balance between inviscid and viscous phenomena acting on it.

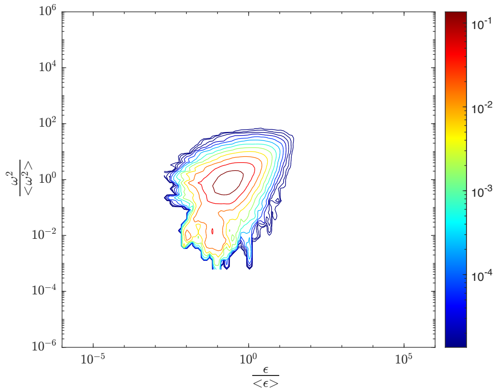

Figure 6. J-PDF of normalized enstrophy and dissipation for the structures.

To further investigate the importance of different physical phenomena in the vortical structures and to compare them with the Burgers' vortex model, all the terms in enstrophy transport equation (equation 3) are calculated along the radial lines of the structures. This equation implies that the rate of change of enstrophy (the material derivative, $\frac{D\omega^2}{Dt} = \frac{\partial \omega^2}{\partial t} + u_j \frac{\partial \omega^2}{\partial x_j}$) desscribes a competition between inviscid vortex stretching $(2\omega_i \omega_j s_{ij})$, the viscous diffusion of enstrophy $(\nu \frac{\partial^2 \omega^2}{\partial x_j \partial x_j})$, and enstrophy dissipation $(-2\nu \frac{\partial \omega_i}{\partial x_j} \frac{\partial \omega_i}{\partial x_j})$. Figure 10 plots the averaged values of these terms conditioned on radial directions of the structures. The terms are normalized by t_η^3 where $t_\eta = (\frac{\nu^3}{\varepsilon})^{1/2}$ is the Kolmogorov time scale. The horizontal axis of the plot represents the normalized radius of the structures. For each radial line, the radial distance from the center (r) is normalized by the local radius of the structure (R).

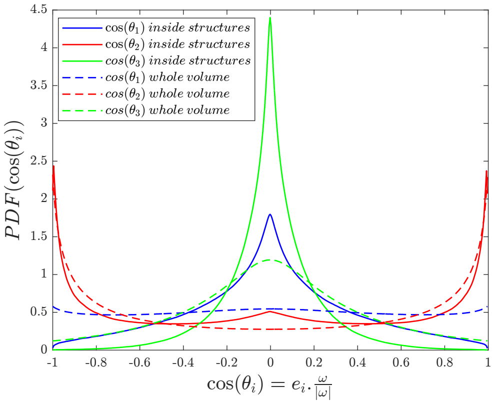

Figure 7. Alignment between the vorticity vector and the eigenvectors of the rate of strain tensor.

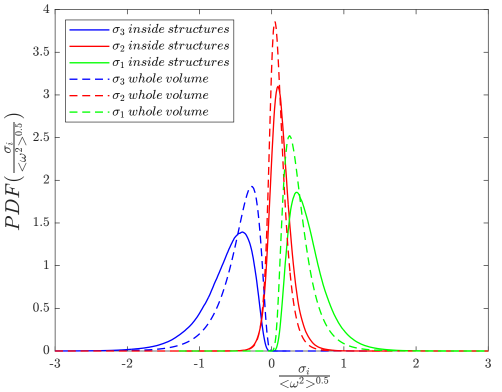

Figure 8. PDFs of eigenvalues of the rate of strain tensor for the whole volume of the flow and inside the vortical structures.

$$\frac{D\omega^2}{Dt} = 2\omega_i\omega_j s_{ij} + \nu\frac{\partial^2\omega^2}{\partial x_j \partial x_j} - 2\nu\frac{\partial\omega_i}{\partial x_j}\frac{\partial\omega_i}{\partial x_j} \tag{3}$$

Figure 10 shows that near the center of the structures ($\frac{r}{R} = 0$), enstrophy diffusion is more dominant than both vortex stretching and enstrophy dissipation, the latter of which has relatively small values resulting in $\frac{D\omega^2}{Dt} < 0$. By marching towards the boundary from the center both vortex stretching and enstrophy diffusion become weaker as dissipation gradually increases. The rate of change of diffusion is faster than vortex stretching which results in $\frac{D\omega^2}{Dt} > 0$ after $\frac{r}{R} \approx 0.2$. Dissipation reaches a maximum near the boundary of the structures. As $\frac{r}{R} > 1$, all the terms become constant (flat). To compare the behaviour with Burgers' vortex model, equivalent Burgers' vortices are considered and the same terms of the equation are calculated and plotted in figure 11. The equivalent Burgers' vortices are achieved by calculating stretching (α_0) and enstrophy (ω_0^2) at the center of the structures. By knowing α_0 and ω_0^2 and using the analytical relations available for Burgers' vortex model all the desired terms can be calculated. By comparing figures 10 and 11 a similar competition between the different terms in the enstrophy transport equation can be observed although with some small changes in their magnitude which shows that, on average the Burgers' vortex model reproduces the dominant physics of the small-scale structures quite well.

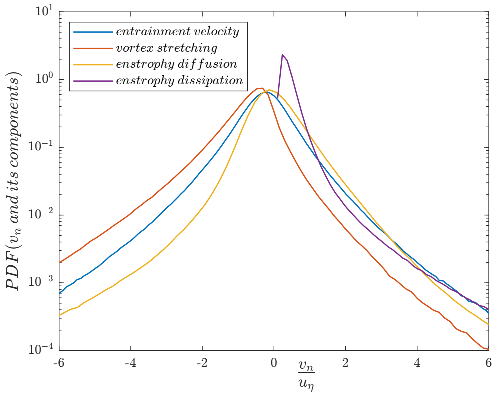

Figure 9. PDFs of entrainment velocity, v_n, at the boundary of the structures and its components.

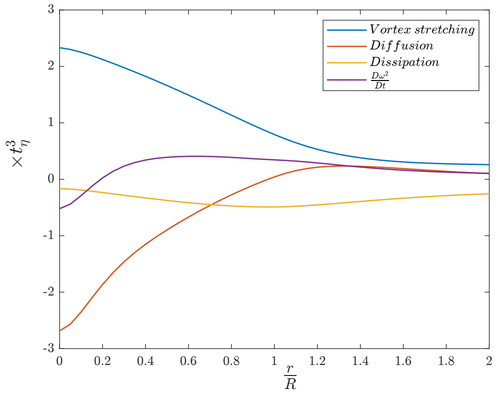

Figure 10. Averaged enstrophy transport equation terms conditioned on radial lines inside the structures.

SUMMARY & CONCLUSIONS

In this study, features of small-scale vortical structures ('worms') in a fully resolved 3D-3C experimental data set of homogeneous axisymmetric turbulence with an $Re_\lambda = 179$ measured at at the center of a large-scale von Kármán mixing tank are investigated. To avoid the arbitrariness in the definition of vortices (thresholding), an objective definition based on Objective Eulerian Coherent Structure (OECS) proposed by Haller *et al.* (2016) is implemented to detect the vortices in the volumetric velocity fields. In total, 12500 vortices were detected in 1003 volumes of the turbulent flow. The average radius of the structures is $\langle R \rangle = 5.1\eta$ that is in agreement with $\langle R \rangle \approx 5\eta$ widely reported in the literature for DNS studies. Small-scale vortex structures were found to occupy 1.4% of the volume of the flow in agreement with $\sim 1\%$ reported in the literature from DNS. Joint PDFs of enstrophy and dissipation within the volume and conditioned inside the structures were showed that the values of enstrophy and dissipation are concentrated in the small-scale vortices compared to the whole

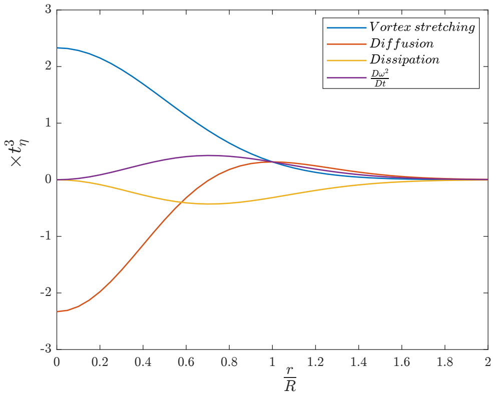

Figure 11. Averaged enstrophy transport equation terms of the equivalent Burgers' vortex model conditioned on radial lines inside the structures.

flow field and that they scale inside the structures. The alignment of the vorticity vector and eigenvectors of the rate of strain tensor showed the vorticity vector has a strong tendency to be aligned with the intermediate eigenvector and be normal to the compressive and extensional eigenvectors as found in previous turbulent flows. Since the average value of the intermediate eigenvalue is positive ($\langle \sigma_2 \rangle > 0$) vortex stretching is the dominant topological phenomenon.

To investigate the exchange of mass by the small-scale vortices, the entrainment velocity equation was solved on the boundary of the structures showing that they, on average, entrain relatively ambient flow from the surroundings. The total volume of the structures does not change in homogeneous stationary turbulence, the mass entrainment is compensated by the mass outflow along the axial direction. It is also shown that the local entrainment/detrainment at the boundary is the result of a competition between inviscid and viscous phenomena. This exchange of mass is accompanied with exchange of momentum, energy, and enstrophy with the ambient fluid. Therefore the structures are not passive in this sense. Finally, the enstrophy transport equation conditioned on radial lines of the vortices was studied and compared to those of equivalent Burgers' vortices. The results indicate that Burgers' vortex model on average reasonably captures the flow physics of the vortex structures.

REFERENCES

Dubief, Yves & Delcayre, Franck 2000 On coherent-vortex identification in turbulence. *Journal of Turbulence* **1**.

Eisma, Jerke, Westerweel, Jerry, Ooms, Gijs & Elsinga, Gerrit E. 2015 Interfaces and internal layers in a turbulent boundary layer. *Physics of Fluids* **27** (5).

Elsinga, G. E. & Marusic, I. 2010 Universal aspects of small-scale motions in turbulence. *Journal of Fluid Mechanics* **662**, 514–539.

Ganapathisubramani, B., Lakshminarasimhan, K. & Clemens, N. T. 2008 Investigation of three-dimensional structure of fine scales in a turbulent jet by using cinematographic stereoscopic particle image velocimetry. *Journal of Fluid Mechanics* **598**, 141–175.

Haller, G., Hadjighasem, A., Farazmand, M. & Huhn, F. 2016 Defining coherent vortices objectively from the vorticity. *Journal of Fluid Mechanics* **795**, 136–173.

Holzner, M. & Lüthi, B. 2011 Laminar superlayer at the turbulence boundary. *Phys Rev Lett* **106** (13), 134503.

Ishihara, Takashi, Kaneda, Yukio & Hunt, Julian C. R. 2013 Thin shear layers in high reynolds number turbulence—dns results. *Flow, Turbulence and Combustion* **91** (4), 895–929.

Jiménez, Javier & Wray, Alan A. 1998 On the characteristics of vortex filaments in isotropic turbulence. *Journal of Fluid Mechanics* **373**, 255–285.

Jiménez, Javier, Wray, Alan A., Saffman, Philip G. & Rogallo, Robert S. 1993 The structure of intense vorticity in isotropic turbulence. *Journal of Fluid Mechanics* **255**, 65–90.

Kang, Shin-Jeong, Tanahashi, Mamoru & Miyauchi, Toshio 2009 Dynamics of fine scale eddy clusters in turbulent channel flows. *Journal of Turbulence* **8**.

Lawson, John M. & Dawson, James R. 2014 A scanning piv method for fine-scale turbulence measurements. *Experiments in Fluids* **55** (12).

Lawson, J. M. & Dawson, J. R. 2015 On velocity gradient dynamics and turbulent structure. *Journal of Fluid Mechanics* **780**, 60–98.

Mistry, Dhiren, Philip, Jimmy & Dawson, James R. 2019 Kinematics of local entrainment and detrainment in a turbulent jet. *Journal of Fluid Mechanics* **871**, 896–924.

Neamtu-Halic, Marius M., Krug, Dominik, Haller, George & Holzner, Markus 2019 Lagrangian coherent structures and entrainment near the turbulent/non-turbulent interface of a gravity current. *Journal of Fluid Mechanics* **877**, 824–843.

Neamtu-Halic, M. M., Mollicone, J. P., van Reeuwijk, M. & Holzner, M. 2021 Role of vortical structures for enstrophy and scalar transport in flows with and without stable stratification. *Journal of Turbulence* pp. 1–20.

Saffman, Philip G 1995 *Vortex dynamics*. Cambridge university press.

da Silva, Carlos B., dos Reis, Ricardo J. N. & Pereira, José C. F. 2011 The intense vorticity structures near the turbulent/non-turbulent interface in a jet. *Journal of Fluid Mechanics* **685**, 165–190.

Tsinober, Arkady 2009 *An informal conceptual introduction to turbulence*, , vol. 483. Springer.

Appendix B

Large-scale forcing modulation of high Reynolds number turbulence in a von Kármán swirling flow

Farid Aligolzadeh, Pawel Baj, and James R. Dawson

Proceeding of the 13^{th} *International Symposium on Turbulence and Shear Flow Phenomena (TSFP13), June 25-28, 2024, Montréal, Canada*

13th International Symposium on Turbulence and Shear Flow Phenomena (TSFP13)
Montreal, Canada, June 25–28, 2024

LARGE-SCALE FORCING MODULATION OF HIGH REYNOLDS NUMBER TURBULENCE IN A VON KÁRMÁN SWIRLING FLOW

Farid Aligolzadeh
Department of Energy and Process Engineering
Norwegian University of Science and Technology
NO-7491 Trondheim, Norway
farid.aligolzadeh@ntnu.no

Pawel Baj
The Faculty of Power and Aeronautical Engineering
Warsaw University of Technology
ul. Nowowiejska 24, 00-665, Warsaw, Poland
pawel.baj@pw.edu.pl

James R. Dawson
Department of Energy and Process Engineering
Norwegian University of Science and Technology
NO-7491 Trondheim, Norway
james.r.dawson@ntnu.no

ABSTRACT

Von Kármán swirling flow is often used as a canonical case to study stationary turbulence experimentally. Although many studies focus on the structure and statistics of turbulence produced at the centre of this flow, several studies focusing on the large-scale global features of the flow have identified interesting phenomena such as equatorial symmetry breaking (de la Torre & Burguete, 2007; Cortet *et al.*, 2010). In this paper, we investigated the potential presence and characteristics of a large-scale slowly rotating structure with high kinetic energy content. The structure was recently identified by Baj *et al.* (2019) at $Re = 3 \times 10^4$. However, we considered a Reynolds number higher than the critical phase transition range proposed by Cortet *et al.* (2010), i.e. $5 \times 10^4 < Re_c < 10^5$. Stereoscopic particle image velocimetry (PIV) was used to measure the stationary flow at $Re = 1.21 \times 10^5$, but such a structure was not observed. However, we found that introducing a modulation with harmonic phase shift between the impellers caused a large-scale oval-shape structure to emerge in the flow. The structure showed oscillations in the axial and circumferential directions of the flow at the modulation frequency, with the axial oscillation being the most significant. The detected structure contained approximately 40% of the kinetic energy of the measured flow.

INTRODUCTION

It is widely agreed that large-scale turbulent motions are flow dependent, whereas their small-scale counterparts possess certain universal features regardless of the flow type. The length scales of the large-scale motions are comparable to the physical size of the flow. Consequently, these motions are greatly impacted by the specific flow geometry, boundary conditions, and instabilities inherent to the flow (Pope, 2000). These motions have been of interest in turbulence research as many natural and engineering applications are related to the large-scale motions, e.g. mixing, drag force, and heat transfer. Some examples of these studies are in pipe flow (Hellström *et al.*, 2015), boundary layer (Lee, 2017), channel flow (Lee *et al.*, 2014), Rayleigh-Bénard flow (Mishra *et al.*, 2011), and Couette flow (Lee & Moser, 2018). The overall conclusion from these studies is that turbulence demonstrates a much wider range of features at large-scales in odds with certain well-established models, e.g. turbulent-viscosity hypothesis. Moreover, large-scale turbulence exhibits nonlocality in time and space, meaning that the turbulent process has a long memory and is influenced by events that occur at remote distances within the flow field (Pope, 2000).

Research on stationary turbulence generated by two counter-rotating discs, known as von Kármán swirling flow, has been conducted since the early works of von Kármán (1921), Batchelor (1951) and Picha & Eckert (1958). The flow is particularly suitable for experimental studies because it produces homogeneous turbulence with high velocity fluctuations and a negligible mean flow at the center of the apparatus, where a stagnation point is established. Most studies on this flow have focused on the dissipation scales near the flow center (Lawson & Dawson, 2015; Debue *et al.*, 2021; Aligolzadeh *et al.*, 2022, 2023). However, the literature on the large-scale features of the flow is relatively limited. de la Torre & Burguete (2007) observed symmetry breaking behavior of the velocity field in a von Kármán flow at $Re \simeq 3 \times 10^5$. This symmetry breaking manifests itself as a slow dynamic, random inversion between two states (bi-stability) when the impellers are counter-rotating. On the other hand, a periodic inversion pattern is observed when a low frequency harmonic forcing is applied to one of the impellers. In a related study, Cortet *et al.* (2010) proposed that turbulence in von Kármán swirling flow undergoes a critical phase transition within the range $5 \times 10^4 < Re < 10^5$. This hypothesis is based on experimental observations of significant maxima required for symmetry breaking within a specific range of impeller forcing. In a recent study, Baj *et al.* (2019) discovered a large-scale, low-frequency velocity structure with high kinetic energy rotating around the axis at $Re \simeq 3 \times 10^4$. The topology of the detected structure reported to be similar to macro-instabilities observed in stirred vessels (Doulgerakis *et al.*, 2011).

The present study aimed to build on the findings of Baj *et al.* (2019) to examine whether the structure exists beyond the critical phase transition Reynolds number reported

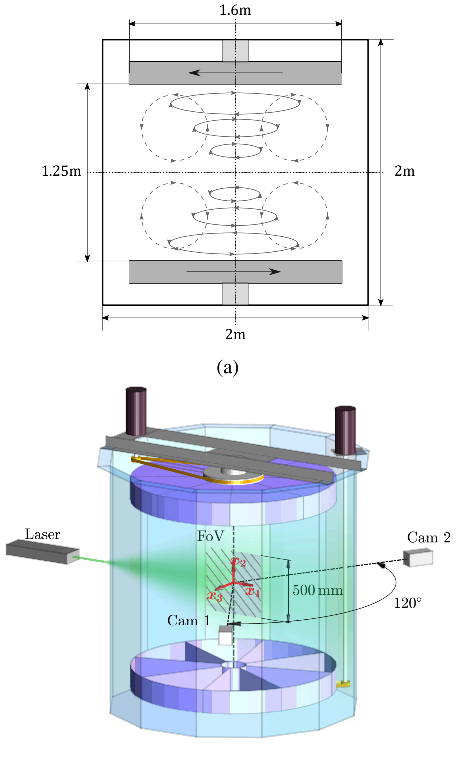

(a)

(b)

Figure 1: Von Kármán swirling flow: (a) sketch of the facility along with the key dimensions and the mean flow pattern and (b) the stereoscopic PIV measurement setup.

by Cortet *et al.* (2010). Another objective was to determine whether it was feasible to activate a similar structure by modulating the impellers.

EXPERIMENTAL PROCEDURE

The measurements were conducted in the large-size von Kármán swirling flow facility at Norwegian University of Science and Technology, Trondheim, Norway. Two identical impellers with a radius of $R = 0.8m$ were located at the top and bottom of a dodecagonal transparent plexiglass tank, $2m$ tall and $2m$ across, filled with water. The impellers were $1.25m$ apart. Sub-figure 1a depicts a schematic of the facility, highlighting its key dimensions. Moreover, it illustrates the mean flow pattern, which is characterized by a primary horizontal shear layer. This layer, in turn, induces a secondary vertical circulation pattern due to the centrifugal pumping force.

As a reference case, the two impellers were set to counter-rotate at a speed of 2rpm ($f_0 = 2/60 = 0.033$ Hz, $\Omega_0 = 2\pi f_0$), which corresponded to a Reynolds number of $Re = R^2\Omega_0/\nu \simeq 1.2\times10^5$. In other cases, modulations were introduced either harmonically, as described in equation 1 for the top impeller and equation 2 for the bottom impeller, or randomly using Langevin forcing (see Pope (2000)). In the harmonic cases, modulation amplitude, frequency, and phase shift between the impellers were represented by A_m, f_m, and $\Delta\phi_m$, respectively.

$$\Omega_t(t) = \Omega_0\Big(1 + A_m \sin(2\pi f_m t + \Delta\phi_m)\Big) \qquad (1)$$

$$\Omega_b(t) = \Omega_0\Big(-1 + A_m \sin(2\pi f_m t)\Big) \qquad (2)$$

A total of 11 cases were measured, including the reference case, 8 cases of harmonic modulations, and 2 cases of random modulations. The base case of harmonic modulation was set to $A_m = 0.25$, $f_m/f_0 = 0.1$, and $\Delta\phi_m = \pi$. The rest of the harmonic modulation cases were produced by varying only one of the three parameters in the base case. These parameters took the following values: $A_m = [0.15,\ 0.25,\ 0.35]$, $f_m/f_0 = [0.05,\ 0.1,\ 0.15]$, and $\Delta\phi_m = [\pi/4,\ \pi/2,\ 3\pi/4,\ \pi]$. However, the present paper discusses only the results for $\Delta\phi_m = \pi, 3\pi/4, \pi/2, \pi/4$ while the other two parameters were kept fixed at $A_m = 0.25$ and $f_m/f_0 = 0.1$. Equations 1 and 2 can be used to decompose the normalized rotation speed of the facility into two components: solid body rotation Ω^*_{sb}, i.e. co-rotation, as shown in equation 3, and shearing Ω^*_{sh}, i.e. counter-rotation, as shown in equation 4:

$$\begin{aligned}\Omega^*_{sb}(t) &= \frac{\Omega_t(t) + \Omega_b(t)}{2\Omega_0} \\ &= 2A_m \cos\Big(\frac{\Delta\phi_m}{2}\Big)\sin\Big(2\pi f_m t + \frac{\Delta\phi_m}{2}\Big)\end{aligned} \qquad (3)$$

$$\begin{aligned}\Omega^*_{sh}(t) &= \frac{\Omega_t(t) - \Omega_b(t)}{2\Omega_0} \\ &= 1 + A_m \sin\Big(\frac{\Delta\phi_m}{2}\Big)\cos\Big(2\pi f_m t + \frac{\Delta\phi_m}{2}\Big)\end{aligned} \qquad (4)$$

When $\Delta\phi_m = \pi$, the two impellers counter-rotate ($\Omega^*_{sb}(t) = 0$). As $\Delta\phi_m$ decreases, amplitude of the harmonic co-rotation between the impellers increases ($\Omega^*_{sb}(t) \neq 0$). The maximum is reached at $\Delta\phi_m = 0$ ($\Omega^*_{sb}(t) = 2A_m \sin(2\pi f_m t)$). In the reference case, only pure shearing was present, i.e. $\Omega^*_{sb,ref}(t) = 0$ and $\Omega^*_{sh,ref}(t) = 1$. Figure 2 demonstrates the profiles of the normalized rotational speed decomposition in different cases over a period of modulation. The correlation coefficient between the solid body and shearing rotations was maximum at $\Delta\phi_m = \pi/2$, with a value of $\rho = 0.01$. It then decreased to $\rho = 0.007$ at $\pi/4$ and $3\pi/4$, and finally reached $\rho = 0$ at $\Delta\phi_m = \pi$.

Stereoscopic PIV was used to measure the velocity fields at the center of the facility. The field of view (FoV) was $\simeq 50\times50\,cm^2$. The spatial resolution of the measurement was $\Delta x = 3.68\,mm \simeq 13.8\eta$ where η was the Kolmogorov length-scale of the flow. The setup for the stereoscopic PIV measurement is shown in sub-figure 1b. The measurements obtained all three components of velocity in a plane (FoV). To ensure a reasonable convergence of turbulence statistics, the time span of the measurements covered at least 1000 rotations of the impellers based on Ω_0 (2rpm). The length-scales from the measurements were normalized by the impeller radius, $x^* = x/R$, and the time-scales were normalized by the impeller frequency in the reference case, $t^* = tf_0$. Reynolds decomposition was implemented on the velocity fields from the measurements, U_i, to calculate the velocity fluctuations $u_i = U_i - \overline{U_i}$ (Pope, 2000).

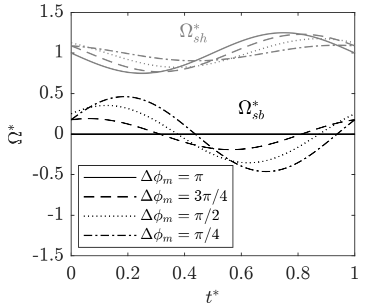

Figure 2: Normalized decomposition of the rotational velocity into shearing, Ω^*_{sh} in gray, and solid body rotation, Ω^*_{sb} in black, in the harmonic modulation cases.

RESULTS

To investigate the effect of forcing modulation on the flow field characteristics, the root mean square (rms) of velocity fluctuations and integral length-scales were calculated in different cases followed by power spectral density (PSD) and proper orthogonal decomposition (POD) analyses to provide a more comprehensive picture. Overall, the flow was predominantly affected when $\Delta\phi_m \neq \pi$, i.e. some degree of solid body rotation existed. This can be observed by comparing the results between the cases. The analysis of velocity components indicated that the modulation effect was most pronounced in the axial direction, followed by the circumferential direction, and finally to a limited extent in the radial direction. However, the effect was missing in the flow field when $\Delta\phi_m = \pi$, i.e. pure shearing, even when f_m and A_m were varied.

Table 1 presents the rms of velocity fluctuations averaged over FoV in the modulated cases with different $\Delta\phi_m$ values, normalized by the corresponding values in the reference case. The rms was defined as $u_i' = (\overline{u_i^2})^{1/2}$, where $\overline{*}$ and $\langle * \rangle$ represent ensemble averaging in time (over realizations) and space (over the FoV), respectively. The rms of velocity fluctuations with instantaneous counter-rotation ($\Delta\phi_m = \pi$) was very similar to the reference values. However, by introducing a harmonic phase shift between the impellers, the rms values deviated form the reference case. As the phase shift increased, the rms values in the axial direction exhibited an incremental trend. The maximum value of $\langle u_2' \rangle / \langle u_{2,ref}' \rangle$ was 1.29 at $\Delta\phi_m = \pi/4$. On the other hand, in the radial direction, the rms values decreased as the harmonic phase shift increased. We observe a convex function in the circumferential direction and the total rms, with the minimum values occurring at $\Delta\phi_m = \pi/2$. The convex trend is also observable, to a lesser degree, in the radial and axial directions. Although the authors are uncertain about the reasons behind this behavior, they speculate that the convexity is linked to the forcing strategy. The forcing modulation was the superposition of harmonic shearing and solid body rotation, with the highest correlation at $\pi/2$, as discussed in the experimental procedure section.

To complement the analysis of the velocity fluctuations and investigate whether the changes in kinetic energy are accompanied by changes in the average length-scales of turbulent motions in different directions, the longitudinal integral length-scales in the axial and radial directions of the flow were estimated using equation 5 (De Jong *et al.*, 2009). In this equation, the two point autocorrelation function is calculated over the available range of FoV from a PIV measurement ($0 < r < r_{max}$) followed by fitting an exponential curve to estimate the missing tail outside the measurement domain ($r_{max} < r < \infty$). The measured velocity field in the radial-axial ($x_1 - x_2$) plane was used to calculate L_{11} and L_{22} in table 2.

Table 1: The spatially averaged rms of velocity fluctuations in the radial (u_1'), axial (u_2'), and circumferential (u_3') directions of the flow, normalized by the reference case.

$(A_m, \frac{f_m}{f_0}, \frac{\Delta\phi_m}{\pi})$	$\frac{\langle u_1' \rangle}{\langle u_{1,ref}' \rangle}$	$\frac{\langle u_2' \rangle}{\langle u_{2,ref}' \rangle}$	$\frac{\langle u_3' \rangle}{\langle u_{3,ref}' \rangle}$	$\frac{\langle u' \rangle}{\langle u_{ref}' \rangle}$
(0.25, 0.1, 1)	1.01	1.02	1.00	1.01
(0.25, 0.1, 0.75)	0.98	1.14	1.03	1.03
(0.25, 0.1, 0.5)	0.76	1.13	0.81	0.85
(0.25, 0.1, 0.25)	0.81	1.29	0.97	0.98

$$
\begin{aligned}
L_{ii} &= \int_0^\infty \frac{\langle \overline{u_i(x) u_i(x + e_i r)} \rangle}{\langle \overline{u_i^2(x)} \rangle} \, dr \\
&\simeq \int_0^{r_{max}} \frac{\langle \overline{u_i(x) u_i(x + e_i r)} \rangle}{\langle \overline{u_i^2(x)} \rangle} \, dr + \int_{r_{max}}^\infty a_i \exp(b_i r) \, dr
\end{aligned}
\tag{5}
$$

Table 2: The longitudinal integral length-scales in the radial (L_{11}) and axial (L_{22}) directions of the flow, normalized by the reference case.

$(A_m, \frac{f_m}{f_0}, \frac{\Delta\phi_m}{\pi})$	$\frac{L_{11}}{L_{11,ref}}$	$\frac{L_{22}}{L_{22,ref}}$	$\frac{L_{22}}{L_{11}}$
(0.25, 0.1, 1)	0.95	1.02	0.74
(0.25, 0.1, 0.75)	0.95	1.30	0.94
(0.25, 0.1, 0.5)	0.91	2.09	1.56
(0.25, 0.1, 0.25)	0.87	2.53	1.98

When the impellers counter-rotated ($\Delta\phi_m = \pi$), the integral length-scales in table 2 varied within ±5% compared to the reference case. However, when solid body rotation was introduced ($0 < \Delta\phi_m < \pi$), a significant continuous growth appeared in the axial direction, accompanied by a decreasing trend in the radial direction. The maximum growth occurred at $\Delta\phi_m = \pi/4$ where $L_{22}/L_{22,ref} = 2.53$. In agreement with this growth in the axial direction, the aspect ratio of the length-scales increased significantly from $L_{22}/L_{11} = 0.68$ in the reference case to $L_{22}/L_{11} = 1.98$ for $\Delta\phi_m = \pi/4$. Thus, modulations with harmonic phase shift between the impellers increased both the kinetic energy and size of the turbulent structure in the axial direction of the flow. The increase in size was more significant than the kinetic energy, i.e. $L_{22}/L_{22,ref} = 2.53$ while $\langle u_2' \rangle / \langle u_{2,ref}' \rangle = 1.29$. This implies that a large-scale motion in the axial direction was activated due to the modulation with some degree of harmonic solid body rotation, where the intensity of this motion varied with $\Delta\phi_m$.

To further investigate this, figure 3 shows the PSDs of the velocity fluctuations, normalized by the reference case. PSD is defined as the Fourier transform of the auto-correlation function of the velocity fluctuations (equation 6). Figure 3 displays the spatially averaged PSDs of velocity fluctuations in the radial u_1, axial u_2, and circumferential u_3 directions of the flow. The area under the PSD curve in the frequency domain is equal to the rms of the corresponding velocity fluctuation in the real (time) domain. The aim here is to investigate the distribution of kinetic energy in the frequency domain with respect to the reference case. This demonstrates how forcing modulations affected the energy distribution in various directions, and whether energy distribution peaks emerged at certain frequencies.

$$S_{u_iu_i}(f) = \int_{-\infty}^{\infty} R_{u_iu_i}(\tau) e^{-\imath 2\pi f\tau} d\tau \tag{6}$$

Sub-figure 3a, the reference case, does not exhibit any peaks in any direction. The same is observed in sub-figure 3b where $\Delta\phi_m = \pi$. However, sub-figures 3d ($\Delta\phi_m = \pi/2$) and 3e ($\Delta\phi_m = \pi/4$) illustrate significant peaks in the axial and circumferential directions at the modulation frequency $f/f_0 = f_m/f_0 = 0.1$. The peak in the axial direction is more prominent than the circumferential direction. Furthermore, sub-figure 3c ($\Delta\phi_m = 3\pi/4$) exhibits a significant peak in the axial direction at the modulation frequency. However, the peak in the circumferential direction disappears. Figure 3 also indicates that when the peaks emerged, the energy was shifted only from low frequencies toward the peak frequency (modulation frequency) while the higher frequencies remained unaffected, similar to the stationary forcing condition (reference case). This redistribution of kinetic energy in the frequency domain might imply that the signature of large-scale forcing modulation was nearly absent at the smaller scales of the turbulent cascade. Further analysis is required to investigate this in more detail.

To evaluate the characteristic flow motions corresponding to the energy peaks observed in the PSD plots (figure 3), POD analysis was utilized (equation 7):

$$u_i(x_j,t) = \sum_{n=1}^{\infty} a_n(t)\Phi_i^n(x_j) \tag{7}$$

First, we consider the stationary forcing (reference case) and subsequently, the analogous plots for the harmonic forcing modulations are presented. This facilitates the comparison between these cases. Sub-figures 4a and 4b display the first two POD modes ($\Phi_i^n(x_j)$) in the reference case, while sub-figure 4c illustrates the PSDs of the time coefficients of these modes ($PSD(a_n(t))$). No peak appeared in the PSD plots of the coefficients. Finally, sub-figure 4d demonstrates the energy share of the modes, i.e. $(\overline{a_n^2(t)}/\sum_{n=1}^{\infty}\overline{a_n^2(t)}) \times 100(\%)$), indicating that the first four modes accounted for 64% of the total fluctuation energy of the flow, while the first two modes accounted for 47%. Figures 5, 6, 7, and 8 depict plots similar to figure 4, with $\Delta\phi_m$ values of π, $3\pi/4$, $\pi/2$, and $\pi/4$, respectively. The values of $A_m = 0.25$ and $f_m/f_0 = 0.1$ were kept unchanged. In figure 5, when $\Delta\phi_m = \pi$, the PSDs plot did not exhibit any peaks (only the first two are presented here). In figure 6, when $\Delta\phi_m = 3\pi/4$, the PSDs of the first two modes did not show any peaks. However, in modes 3 and 4, peaks appeared at the modulation frequency where the two modes contributed to a total of $12.6 + 6.2 = 18.8\%$ of the kinetic energy of the flow. These modes are topologically paired and together formed a single structure. The PSDs of their time coefficients indicate that this structure oscillated harmonically only in the axial direction at the modulation frequency. However, it was axisymmetric in the circumferential direction without any oscillation at a specific frequency. In figures 7 and 8, PSD peaks appeared in modes 1, 2, and 4 for $\Delta\phi_m = \pi/2$ and $\Delta\phi_m = \pi/4$. The first two modes accounted for $24.3 + 16.1 = 40.4\%$ and $22.8 + 13.6 = 36.4\%$ of the kinetic energy of the flow, respectively. The first two modes are paired and together formed an energetic structure that resembled an oval. In addition, the PSDs of their time coefficients suggest that the structure oscillated harmonically at the modulation frequency in both the axial and circumferential directions.

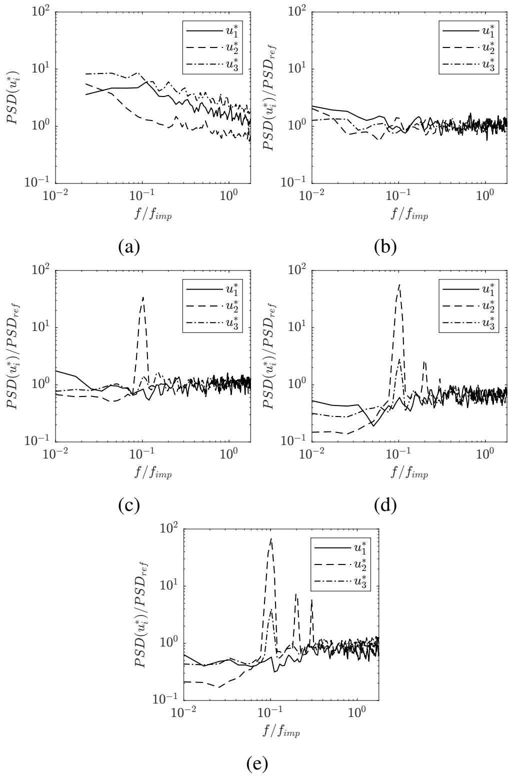

(a) (b) (c) (d) (e)

Figure 3: Normalized PSDs of velocity fluctuations in the radial (u_1), axial (u_2), and circumferential (u_3) directions within the cases ($A_m = 0.25$, $f_m/f_0 = 0.1$, $\Delta\phi_m$): (a) reference (no modulation), (b) $\Delta\phi_m = \pi$, (c) $\Delta\phi_m = 3\pi/4$, (d) $\Delta\phi_m = \pi/2$, (e) $\Delta\phi_m = \pi/4$.

CONCLUSION

In this paper, we investigated the presence of large-scale harmonic motions in a von Kármán swirling flow at $Re = 1.21 \times 10^5$, a Reynolds number higher than the critical range hypothesised by Cortet *et al.* (2010), i.e. $5 \times 10^4 < Re_c < 10^5$. This study was motivated by the observations of Baj *et al.* (2019) at $Re = 3 \times 10^4$, below the critical range. We used stereoscopic PIV to measure the flow in our large-size facil-

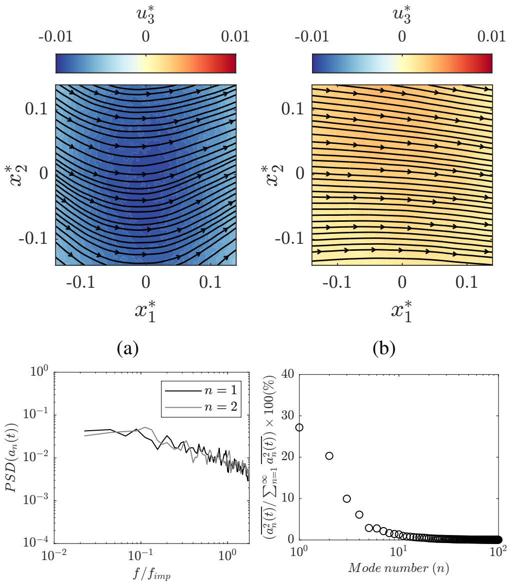

(a) (b)

(c) (d)

Figure 4: POD analysis of the reference case; (a) mode 1 and (b) mode 2 , i.e. $\Phi_i^{n=1}(x_j)$ and $\Phi_i^{n=2}(x_j)$ where u_1^* and u_2^* are shown as the streamlines and u_3^* as the filled contour. (c) PSDs of the time coefficients of modes 1 and 2. (d) The energy share of the modes.

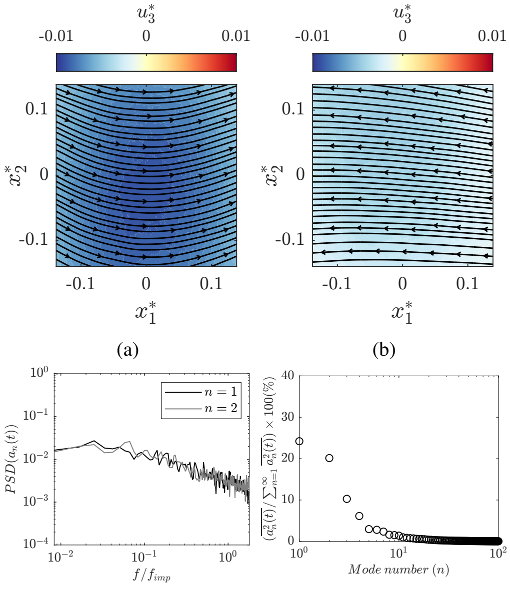

(a) (b)

(c) (d)

Figure 5: POD analysis of the case ($A_m = 0.25$, $f_m/f_0 = 0.1$, $\Delta\phi_m = \pi$); (a) mode 1 and (b) mode 2 , i.e. $\Phi_i^{n=1}(x_j)$ and $\Phi_i^{n=2}(x_j)$ where u_1^* and u_2^* are shown as the streamlines and u_3^* as the filled contour. (c) PSDs of the time coefficients of modes 1 and 2. (d) The energy share of the modes.

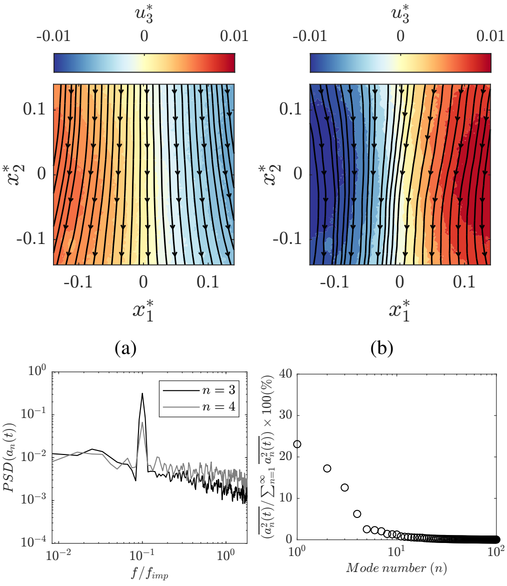

(a) (b)

(c) (d)

Figure 6: POD analysis of the case ($A_m = 0.25$, $f_m/f_0 = 0.1$, $\Delta\phi_m = 3\pi/4$); (a) mode 3 and (b) mode 4 , i.e. $\Phi_i^{n=3}(x_j)$ and $\Phi_i^{n=4}(x_j)$ where u_1^* and u_2^* are shown as the streamlines and u_3^* as the filled contour. (c) PSDs of the time coefficients of modes 3 and 4. (d) The energy share of the modes.

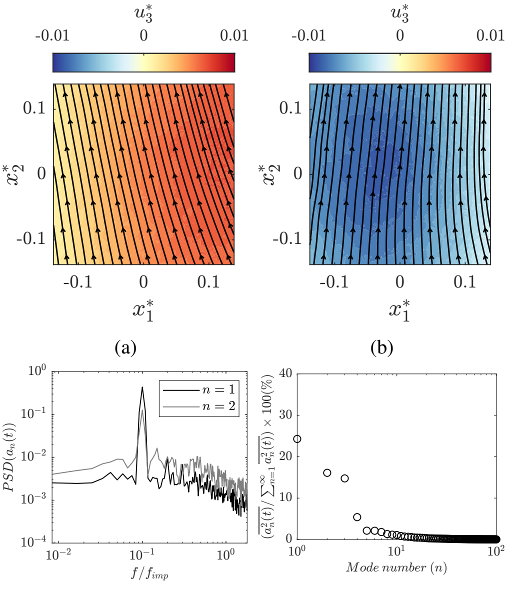

(a) (b)

(c) (d)

Figure 7: POD analysis of the case ($A_m = 0.25$, $f_m/f_0 = 0.1$, $\Delta\phi_m = \pi/2$); (a) mode 1 and (b) mode 2 , i.e. $\Phi_i^{n=1}(x_j)$ and $\Phi_i^{n=2}(x_j)$ where u_1^* and u_2^* are shown as the streamlines and u_3^* as the filled contour. (c) PSDs of the time coefficients of modes 1 and 2. (d) The energy share of the modes.

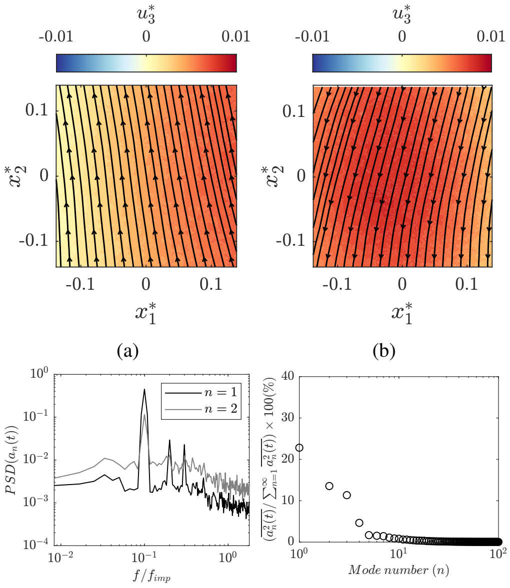

(a) (b)

(c) (d)

Figure 8: POD analysis of the case $(A_m = 0.25,\ f_m/f_0 = 0.1,\ \Delta\phi_m = \pi/4)$; (a) mode 1 and (b) mode 2 , i.e. $\Phi_i^{n=1}(x_j)$ and $\Phi_i^{n=2}(x_j)$ where u_1^* and u_2^* are shown as the streamlines and u_3^* as the filled contour. (c) PSDs of the time coefficients of modes 1 and 2. (d) The energy share of the modes.

ity. No such a structure was detected in the stationary flow. The possibility of activating a similar large-scale harmonically oscillating structure was explored by applying harmonic modulations to the impellers. Various numerical techniques were employed to assess the flow fields from the measurements, such as rms of velocity fluctuations (u_i'), longitudinal integral length-scales (L_{ii}), PSD, and POD. The results indicated that when the amplitude of solid body rotation increased (decreasing $\Delta\phi_m$ from π to $\pi/4$), the rms of velocity fluctuations and the longitudinal integral length-scale in the axial direction of the flow, u_2' and L_{22}, showed incremental trends. The growth rate of L_{22} was more pronounced than that of u_2'. The PSD and POD analyses revealed the appearance of a large-scale oval-shape structure in the flow with harmonic oscillations only when solid body rotation was introduced ($\Delta\phi_m \neq \pi$). When $\Delta\phi_m = \pi/4$ and $\pi/2$, the structure showed the most significant energetic harmonic oscillations in the axial direction of the flow, while the circumferential direction showed weaker harmonic oscillations. The oscillating structure accounted for approximately 40% of the kinetic energy of the flow. However, when $\Delta\phi_m = 3\pi/4$, the harmonic oscillation emerged only in the axial direction of the flow, and not in the circumferential direction. This axially oscillating structure accounted for approximately 20% of the kinetic energy of the flow. The radial direction of the flow in the mentioned cases did not exhibit any significant harmonic oscillations.

REFERENCES

Aligolzadeh, Farid, Holzner, Markus & Dawson, James R. 2022 Study of fine-scale vortical structures in a von kármán mixing flow. In *Proceedings of the 12th International Symposium on Turbulence and Shear Flow Phenomena (TSFP-12)*.

Aligolzadeh, Farid, Holzner, Markus & Dawson, James R 2023 Entrainment, detrainment and enstrophy transport by small-scale vortex structures. *Journal of Fluid Mechanics* **973**, A5.

Baj, Pawel, Dawson, James R., Worth, Nicholas A., Knutsen, Anna N., Lawson, John M. & Bodenschatz, Eberhard 2019 Very large-scale motions in von kármán flow. In *Proceedings of the 11th International Symposium on Turbulence and Shear Flow Phenomena (TSFP-11)*.

Batchelor, Go K 1951 Note on a class of solutions of the navier-stokes equations representing steady rotationally-symmetric flow. *The quarterly journal of mechanics and applied mathematics* **4** (1), 29–41.

Cortet, P-P, Chiffaudel, Arnaud, Daviaud, François & Dubrulle, Bérengère 2010 Experimental evidence of a phase transition in a closed turbulent flow. *Physical review letters* **105** (21), 214501.

De Jong, J, Cao, L, Woodward, SH, Salazar, JPLC, Collins, LR & Meng, H 2009 Dissipation rate estimation from piv in zero-mean isotropic turbulence. *Experiments in fluids* **46**, 499–515.

Debue, P, Valori, V, Cuvier, C, Daviaud, F, Foucaut, J-M, Laval, J-P, Wiertel, C, Padilla, V & Dubrulle, B 2021 Three-dimensional analysis of precursors to non-viscous dissipation in an experimental turbulent flow. *Journal of Fluid Mechanics* **914**, A9.

Doulgerakis, Zacharias, Yianneskis, Michael & Ducci, Andrea 2011 On the manifestation and nature of macroinstabilities in stirred vessels. *AIChE journal* **57** (11), 2941–2954.

Hellström, Leo HO, Ganapathisubramani, Bharathram & Smits, Alexander J 2015 The evolution of large-scale motions in turbulent pipe flow. *Journal of Fluid Mechanics* **779**, 701–715.

von Kármán, Th 1921 Uber laminare und turbulente reibung. *Z. Angew. Math. Mech.* **1**, 233–252.

Lawson, John M & Dawson, James R 2015 On velocity gradient dynamics and turbulent structure. *Journal of Fluid Mechanics* **780**, 60–98.

Lee, Jin, Lee, Jae Hwa, Choi, Jung-Il & Sung, Hyung Jin 2014 Spatial organization of large-and very-large-scale motions in a turbulent channel flow. *Journal of fluid mechanics* **749**, 818–840.

Lee, Jae Hwa 2017 Large-scale motions in turbulent boundary layers subjected to adverse pressure gradients. *Journal of Fluid Mechanics* **810**, 323–361.

Lee, Myoungkyu & Moser, Robert D 2018 Extreme-scale motions in turbulent plane couette flows. *Journal of Fluid Mechanics* **842**, 128–145.

Mishra, Pankaj Kumar, De, Arnab K, Verma, Mahendra K & Eswaran, Vinayak 2011 Dynamics of reorientations and reversals of large-scale flow in rayleigh–bénard convection. *Journal of fluid mechanics* **668**, 480–499.

Picha, KG & Eckert, ERG 1958 Study of the air flow between coaxial disks rotating with arbitrary velocities in an open or enclosed space. *proceedings of 3rd US Nat. Cong. Appl. Mech* .

Pope, Stephen B 2000 *Turbulent flows*. Cambridge university press.

de la Torre, Alberto & Burguete, Javier 2007 Slow dynamics in a turbulent von kármán swirling flow. *Physical review letters* **99** (5), 054101.

ISBN 978-82-326-8194-5 (printed ver.)
ISBN 978-82-326-8193-8 (electronic ver.)
ISSN 1503-8181 (printed ver.)
ISSN 2703-8084 (online ver.)

NTNU
Norwegian University of
Science and Technology